Application of pn-CCD detector for imaging of nanowires using white synchrotron radiation

DISSERTATION

zur Erlangung des Grades eines Doktors

der Naturwissenschaften

vorgelegt von

M. Sc. Alaa Algashi

eingereicht bei der Naturwissenschaftlich-Technischen Fakultät

der Universität Siegen

Siegen 2019

Application of pn-CCD detector for imaging of nanowires using white synchrotron radiation

DISSERTATION

zur Erlangung des Grades eines Doktors

der Naturwissenschaften

vorgelegt von

M. Sc. Alaa Algashi

eingereicht bei der Naturwissenschaftlich-Technischen Fakultät

der Universität Siegen

Siegen 2019

Gutachter:

Prof. Dr. Dr. Ullrich Pietsch
Prof. Dr. Lothar Strüder

Tag der mündlichen Prüfung:17 December 2019

Gedruckt auf alterungsbeständigem holz- und säurefreiem Papier.

Zusammenfassung

Der pnCCD Detektor fand inzwischen vielfälltige Anwendungen in der Materialforschung. Neben Weißstrahl Laue Beugung von einkristallinen und polykristallinen Materialien sowie Vielfachschichten von Hartstoffen und weicher Materie demonstrieren wir hier erste Anwendungen des Detektors für die Analyse von Halbleiter Nanodrähten.

Zum ersten Male wurde die energiedispersive Laue Beugung von weißer Röntgenstrahlungn und unter Nutzung einer frame-store pnCCD für die Strukturanalyse von Halbleiter Nanodrähten verwendet. Hierzu wird die Probe mit einem weißen Synchrotrostrahl im Energieintervall von 8 bis 120 keV bestrahl was einer Zahl von Laue spots führt, die die Braggbedingung für verscheidene Energien gleichzeitig erfüllt. The schnelle und genaue Charakterisierung der Matrialien mittels dieser Methode erfordert die gleichzeitige Detektion der Beugungswinkel und Beugungsenergien.

Ziel dieses Projektes war die Untersuchung verschiedener Nanodrähte mittels weißer Röntgenstrahlung unter Nutzung der pnCCD. Zuerst zeigen wir die Röntgenbeugung an Arrays von GaAs NW die auf GaAs B Substraten gewachsen wurden. Das Experiment wurde im Heimatlabor der Universität Siegen in coplanarer Bragggeometrie ausgeführt. Die strukturellen Eigenschaften wurden mittels einer quasi Einzelschuß Detektion des reziproken Raumes erhalten. Neben dem GaAs Substratpeak funden wir einen zweiten Peak, der den Gas Nanodrähten zuzuordnen ist. Aus der Differenz der Beugungspositionen und Beugungsenergien wurde die Gitterfehhlanpassung beider Komponenten bestimmt.

Als zweites wird über eine detilliertere Analyse von InAs NW die auf GaAs[111] B Flächen gewachsen wurden, berichtet. Das Experiment wurde an der EDR Meßstrecke bei BESSY II ausgeführt. Die enrgie-dispersive Röntgenbeugung

profitierte dabei vom hohen Photoenfluß in einem weiten Energeiintervall zwischen $5<E<35$ keV, so dass viele Braggreflexe ohne Probenrotation erfasst werden konnten. Die hochenergetische Röntenstrahlung erlaubte zusätzlich die Messung eines großen Ausschnitts des reziproken Raumes und damit den Zugang zur Realstruktur der InAs Nanodrähte und des GaAs Substrates und weiterer Reflexe gleichzeitig. Insbesondere konnten wir das gleichzeitige Auftreten von der Wurzite und Zinkblende Phasen in den InAs NW nachweisen.

Zuletzt wurden GaAs/In_xGa_{1-x} As/GaAs Kern-Mantel NW , die mittels MBE auf Si(111) Substraten gewachsen wurden, an der EDDI Meßstrecke bei BESSY II gemessen. In diesem Experiment kamen Röntgenenergien zwischen 20 und 120 keV zu Einsatz und die Probe wurde nahezu parallel zu [111] Richtung eingestrahlt. Wegender großen Breite des verwendeten Energiespektrums wurden Lauespots mehrer hochindizierter Reflexfamilien {hkl} mit unterschiedlichen Gitterparametern gleichzeitig gemessen, die die jeweilige Braggbedingung gelichzeitig erfüllen. Nach Auswertung der Lauespots und der Korrektur der kleinen Einfallswinkelabweichung des Einfallsstrahls relativ zur [111] Achse wurde die Pseuomorphie der Gitter des Kern und Mantelmaterials verifiziert.

Zusammenfassend wurde dargestellt, dass unter Nutzung weißer Synchrotronstrahlung die pnCCD eine 3D Verteilung der Intensität im reziproken Raum liefert, die über zwei räumliche Achsen und einer Energieachse aufgespannt ist. In dieser Weise erlaubt das Detektiosnsystem die Erfassung der Struktur von Halbleiter-NWs (GaAs, InAs, GaAs/ In_xGa_{1-x} As /GaAs), weil viele Lauereflexe gleichzeitig erfasst warden können, was mit monochromatiscer Strahlung nicht möglich ist.

Abstract

The pnCCD detector became an instrument which shows wide applications in material research. Besides white-beam Laue diffraction von single and polychrystalline materials the multilayer analysis of hard coatings and soft matter we demonstrate first application for the analysis of semiconductor nanowires (NWs).

For the first time, a frame-store pn-junction CCD has been applied for structure analysis of semiconductor nanowires by means of energy-dispersive Laue diffraction using white synchrotron radiation in the energy range of 8 to 120 keV. Here a white x-ray beam exposes the sample providing a number of Laue spots which fulfill the Bragg condition for different x-ray energies. The fast and precise characterization of any materials by this method requires a simultaneous position and energy resolved detection of X-rays.

The aim of this project was to investigate the real structure of different semiconductor NWs using white beam and pn CCD detector. Firstly, we present X-ray diffraction pattern taken from a periodic GaAs NW array that was grown onto GaAs[111]B surface. The experiment was performed at the home laboratory at Siegen University using a coplanar Bragg reflection. The structural properties were probed by measuring reciprocal space by quasi single shot exposure. Besides the peak related to the reflection from GaAs substrate, we found a second peak referring to the reflection from NWs. Form the difference of peak positions and peak energies the lattice mismatch between the NWs and the substrate was deduced.

Secondly, a more detailed analysis was performed on InAs NWs grown onto GaAs[111]B. The experiment was carried out at the EDR beam line of BESSY II synchrotron. Energy-dispersive X-ray diffraction techniques rely on a high usable photon flux in a wide energy range (5< E< 35 KeV) so that as many Bragg peaks

as possible can be detected in a single X-ray shot without any sample rotation. In addition, the usage of high-energy X-ray diffraction enables to measure a large section of reciprocal space at the same time allowing for probe the real structure of the InAs NWs and substrate GaAs and insensitive reflections simultaneously. By this experiment we could deduce the simultaneous appearance of wurtzite and zinc-blende phases in InAs NWs.

Finally, we measured GaAs/In_xGa_{1-x} As/GaAs core-shell NWs grown by molecular beam epitaxy (MBE) onto a Si (111) substrate at the EDDI beamline of BESSY II. In this system, the incident x-ray beam energy ranges between 20 to 120 keV and illuminates the sample nearly parallel to the [111] direction. Due to the wide range of x-ray energies provided various Laue spots of few highly indexed {hkl} families with different lattice plane fulfill the Bragg condition simultaneous. After the evaluation the Laue spots and correction caused by the small misalignment of the incident beam with respect to [111] direction the pseudomorphic growth of the In_xGa_{1-x} As shell and the GaAs core has been verified.

In summary, by using white synchrotron radiation the pnCCD provides a three dimensional intensity distribution composed by two pixel coordinates and an energy direction covering a 3D data volume in reciprocal space. In this sense, the system provides a good possibility to investigate the structure of semiconductor NWs (GaAs, InAs, GaAs/ In_xGa_{1-x} As /GaAs) because several Laue reflections can be probed simultaneous which is impossible using monochromatic radiation.

Table of contents

1. Introduction..1
2. The pn-CCD Detector 5
2.1. Concept of the pn-CCD 5
2.2. Measurement Process...6
2.2.1. Absorption of Impinging X-ray Photons (charge generation) 7
2.2.2. Charge Collection 8
2.2.3. Charge Transfer 9
2.2.4 Read out electronics………………………………………………………11
2.3. Quantum efficiency………………………………………………………14
2.4. Physical properties of the pnCCD……………………………………...15
2.4.1. Position resolution 16
2.4.2. Energy resolution 17
2.4.3. Time resolution 18
3. Semiconductor nanowires…………………………………………………...20
3.1. pitaxial growth of semiconductor nanowires……………………………..20
3.2. Techniques for nanowir growth……………………………………………...23
3.2.1. Vapor-liquid-solid (VLS)……………………………………………………23
3.3. Crystal Structure of NWS growth……………………………………………25
4. X ray diffraction on crystal…………………………………………………...29
4.1. Crystal structure and direct lattice……………………………………………29
4.2. Reciprocal Lattice……………………………………………………………..31
4.3. Bragg’s Law……………………………………………………………………..34
4.4. Bragg condition and Laue equations……………………………………... 35
4.5. Kinematical scattering theory……………………………………………... 38
5. Experiment at home ………………………………………………………….42
5.1. Introduction...43
5.2. The pn-CCD Detector…………………………………………………………43
5.3. Experiment section……………………………………………………………..44
5.3.1.Sample …………………………………………………………………………44

5.3.2. Setup of Experiment……………………………………………………… 45
5.3.3. Incoatec microfocus source IμS …………………………………………46
5.4. Discussion and results…………………………………………………… 47
5.5. Conclusion…………………………………………………………………50
6. EDR Experiment……………………………………………………….51
6.1. Introduction...51
6.2 Synchrotron radiation source (EDR bemline-BESSY II)…………………54
6.3 Setup of the Experiment………………………………………………...56
6.4 Discussion and results…………………………………………………..57
6.5 Conclusion ……………………………………………………………...66
7. EDDI Experiment ………………………………………………………67
7.1 Introduction...67
7.2 pnCCD detector..69
7.3. Energy –dispersive Laue diffraction...70
7.3.1. Sample ……………………………………………………………………70
7.3.2 Setup of experiment...72
7.4. Data analysis and results...73
7.5. Conclusion ……………………………………………………………..83
7.6. Supplement ……………………………………………………………..84
8. Conclusion& Outlook …………………………………………………..87
9. Bibliography………………………………………………………………91
10. Acknowledgements………………………………………………………111

Chapter 1

1. Introduction

To understand structures of semiconductor nano-materials are usually investigated using monochromatic X- ray diffraction techniques. Currently, by using highly brilliant synchrotron radiation, the pnCCD detector opens a wide field to investigate precise structures, strain and lattice mismatch of semiconductor nano-materials such as core shell nanowires (NWs) at fixed scattering geometry.

one dimensional semiconductor nanostructure, such as NWs, NW heterostructures and nanotubes are candidates for next generation electronic and photonic devices because of the low power consumption caused by the strong lateral quantum confinement effects [1,2]. For this reason, the field of semiconductor NWs becomes one of the most active research areas within a nanoscience community within the past decade. Many applications of semiconductor NWs for nanodevices have been demonstrated, such as NWs diodes [3], lasers [4,5], photodetectors [6,7,8], field effect transistors [9, 10, 11, 12, 13, 14],solar cells [15, 16, 17,18],etc.

$A^{III}B^{V}$ NWs grown onto Si (111) substrates are promising materials for future integration of optoelectronic applications in the Si technology [19, 20]. Grown by molecular beam epitaxy (MBE) or metal-organic vapor phase epitaxy, NWs can be grown as perfect crystalline material [21, 22]. The GaAs, InAs and GaAs/$In_xGa_{1-x}As$/GaAs core-shell composition of semiconductor NWs allows for various applications in the field of optoelectronics and energy harvesting [23].

Here, after the growth of the GaAs/$In_xGa_{1-x}As$/GaAs core-shell NWs, the material with a different lattice parameter is grown onto its side facets. For a nominal In content of 25% within the $In_xGa_{1-x}As$ shell, the strain accommodation

within the core-shell NW system is in the elastic regime [24]. Therefore, both materials grow pseudomorphic along the growth direction, faced by major deformation along the radial direction. In addition, due to growth along the zinc-blende (ZB) [111] direction, major structural defects such as the inclusion of stacking faults, and the appearance of different structural phase, such as the wurtzite (ZW) or 4H polytypes along the growth axis may deteriorate the performance of the respective devices requiring careful structural analysis of the NWs. Typically, the crystal phase structure and strain in NWs are investigated by high-resolution transmission electron microscopy (HRTEM) [25,26,27] and monochromatic x-ray diffraction (XRD) techniques [28]. Recently we have demonstrated that the complete structure of core-shell NWs can be determined using x-ray nano-diffraction measuring Bragg diffraction along and perpendicular to the NW growth axis [29]. Nevertheless, these measurements are time consuming and require additional modeling in terms of the finite element method. On the other hand, HRTEM analysis can only be applied locally as the prepared lamella needs to be less than a hundred nanometers thick. Moreover, the milling process is usually done using a focused ion beam which may induce detrimental changes to the crystal lattice. Therefore an alternative and less complicated method that can be used for strain characterization in NWs is demanded. In this work, we demonstrate that the use of highly brilliant synchrotron radiation in combination with the energy dispersive pnCCD detector opens a new route of fast and precise structural analysis of GaAs ,InAs and GaAs/$In_xGa_{1-x}As$/GaAs core-shell NWs in their as-grown geometry. For the first time, we used the pnCCD detector to measure the 3D strain state in GaAs , InAs and GaAs/$In_xGa_{1-x}As$/GaAs core-shell NWs. Initially, the European Photon Imaging pnCCD Camera on x-ray astronomy Multi-Mirror Mission (XMM-Newton) could be fabricated under the leadership of the Max Planck Institute for extraterrestrial physics.

The pn-CCD camera system have been tested and qualified to readout schemes containing astronomical observations [30]. A further developed type of the pn-

CCD detector has been also investigated for the extended Roentgen survey with an imaging telescope array (eROSITA) [31] which acts as a pathfinder for the spectrum Roentgen Gamma and the x-ray observatory. An advanced generation for pn-CCDs detector with a frame store operation [32] maintains the spatial resolution during the readout time of the accumulated image and can be operated at a higher rate of counting. The quantum efficiency of the pn-CCD reaches to 90% even at the energy of 11 keV as the 450 mm thick detector is fully depleted [33]. The first spectroscopic measurements of these eROSITA pn-CCD achieved an energy resolution of 143 eV for all events at 5.9 keV [34]. In especially, the pnCCD camera was developed with larger chip sizes and lower noise levels for the eROSITA satellite mission and reducing cycle time by increasing the counting of frame rate recorded for high speed applications [35, 36].The primary objective of this development and continuous improvement of the flexibility of x-ray pn-CCD detectors is to obtain as much information as possible about a sample using x-ray diffraction techniques. The pn-CCD detector has an ultrafast readout allowing detection of single photons with a time resolved, simultaneous position and energy dispersive detection of x-rays. In this sense, the single photon counting mode is achievable even at relatively high photon count rates as available at synchrotron. Therefore, highly brilliant x-ray beams generated by synchrotrons allow for high-quality structure analyses of core shell NWs by generation diffraction patterns for each energy contained in the complete white spectrum. The first application of pn-CCD detector using white synchrotron radiation is the three-dimensional resolution of pn-CCd which tested in the grazing-incidence small-angle scattering (GISAXS) experiment [37]. The Laue energy diffraction on organic and inorganic crystals has been successfully applied using soft and hard x-ray. It was reported that by recording the Laue pattern of energy solution of a sample and converting the three-dimensional information into reciprocal space coordinates, high accuracy information about the sample can be obtained [38, 39]. In addition, no prior knowledge and rotation of a sample by quasi single shot exposure are required using white beam which provides a complete indexing of the recorded Laue pattern by pn CCD detector [40, 41]. The

energetic structure of Laue peaks from plastically deformed Cu micro beam revealed by a three-dimensional x-ray detector [42]. Performing a micro-beam Laue experiment the full strain tensor was calculated by a single shot experiment at a deformed Cu [43].

In current project, we study the structure and strain of GaAs NWs grown onto GaAs[111]B at home, InAs NWs grown onto GaAs[111]B at the EDR beam line of the BESSY II and GaAs/$In_xGa_{1-x}As$/GaAs core-shell NWs onto Si[111]B at the EDDI beam line of the BESSY II using the pnCCD detector and a white beam. In this work, we demonstrate that a Laue diffraction experiment allows for a fast access to the structural parameters of NWs which is promising for future use in NW device technology.

Chapter 2

2. The pn-CCD Detector

In this chapter, the characteristic properties of the pn-CCD detector will be highlighted focusing on the operating system which will be discussed in successive steps from generation of the charges inside the detector up to digitizing of the resulting electrical signal. In addition to the properties of the device also will be presented which include quantum efficiency, position, and energy and time resolution.

2.1. Concept of the pn-CCD

The pn-CCD is a semiconductor silicon array detector of 450 µm thickness. It is a back-illuminated charge coupled device with fully depleted silicon chip. This detector was designed and developed in the semiconductor lab of Max-Planck-Institute (München) for space applications and used later for X-rays imaging in the energy range (2 keV to 150 keV) [44]. One of the most interesting features of this detector is its high quantum efficiency. In addition, it shows good spatial and energy resolution and allows for a very fast readout of the images because of the high frame rate [45, 46, 47].

The pn-CCD detector that is currently used in the laboratory of solid state physics is divided in two parts: namely in an image area (384×384 pixels with 75×75 μm^2 pixel size) and a frame store area (384×384 pixels with 75×51 μm^2 pixel size). When the pn-CCD is operated in frame store mode, the image is transferred from image store area to the frame store area by a fast transfer. Then, it is read out row by row from the frame store area while photons are again recorded in the image area for the next picture. Two 384-channel VLSI JFET-CMOS CAMEX chips are used for the simultaneous readout of the 384 pixel signals per row as shown in figure 1.1.

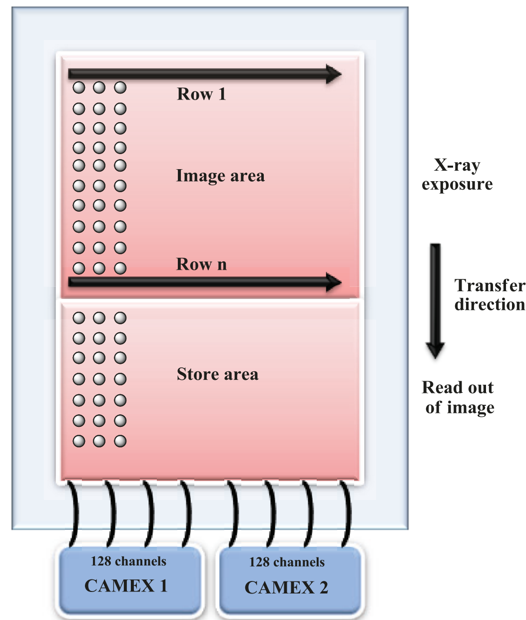

Figure 1.1 Schematic drawing of the pn-CCD detector shows the two different areas and the operation of the image in frame store mode.

2.2. Measurement Process

The functional principle of the pn-CCD detector (schematically shown in figure 1.2) can be summarized by the following steps: 1) generation of electron-hole pairs upon absorption of X-ray photons energy; 2) collection of generated electrons in a pixel array; 3) charge transport of each pixel charge by moving them pixel by pixel until they are reaching the readout node; 4) charge measurement as voltage value which is proportional to the number of generated electrons.

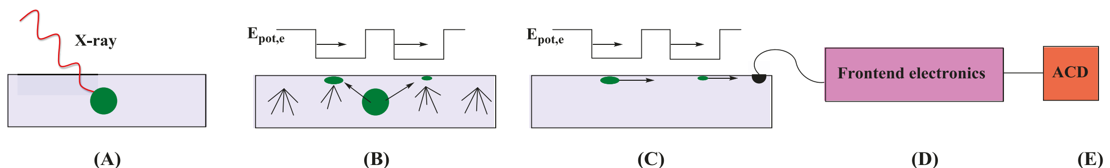

Figure 1.2 Schematic of the measurement process. (A) charge generation; (B) charge storage; (C) charge transfer to read out anode; (D) frontend signal processing; (E) digitization.

2.2.1. Absorption of Impinging X-ray Photons (charge generation)

When the photon penetrates the pn-CCD detector from the backside, it interacts with any silicon atom. Upon absorption of the X-ray radiation, electron-hole pairs will be generated in the space-charge region of the semiconductor by photoelectric absorption process. Depending on the incident energy, a number of generated electrons per photon energy is $N = E_{ph}/w$ eV. Where w= 3.63eV is the amount of energy needed for create one electron-hole pair [48].

The electrons which are generated by photo- and Auger- electrons move through the silicon bulk and lose their energy by inelastic Coulomb collisions in the semiconductor. Each collision includes two processes which consume the transported energy. The first process could be explained by jumping of one electron from the valence to the conduction band accompanied with a formation of one hole in the valence band. As consequence, a part of the collision energy is invested in the generation of an electron–hole pair (Figure 1.3).

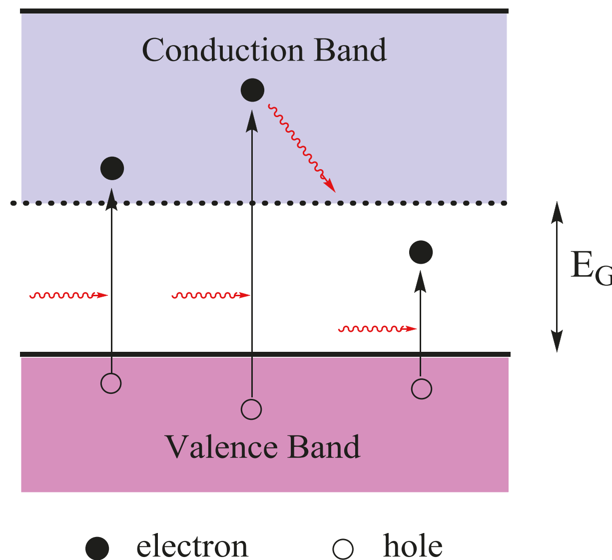

Figure 1.3 Absorption of photons energy equal, larger, or smaller than the band gap E_g, and the consecutive generation of an electron-hole pair in a semiconductor.

The second process is producing again another photoelectron by absorbed energy of either Auger-electron or a fluorescence photon. Because of multiple Coulomb collisions in the silicon chip, the ejected electrons lose their energy by generation of electron-hole pairs till the complete energy of the absorbed photon is released to the material. The variance of the number (N) of elector-hole pairs created is given by the following equation (2.1):

$$< \Delta \mathrm{N}^2 >= F.N = F\frac{E_{ph}}{w} \quad (2.1)$$

Where E_{ph} is the energy absorbed in the detector and F is a Fano factor of material specific constant that measures the fluctuation in the number of ionization events.

In a word, the silicon bulk absorbs the X-ray photon energy and converts it completely into electron-hole pairs and the amount of these pairs is proportional to the photon energy.

2.2.2. Charge Collection

After the generation of the electron-hole pairs across the bulk, they are located where the X-ray photon was absorbed. The charges will be accelerated by high electric field in the depletion region will be become and separated into electrons and holes before they recombine. The holes will be attracted to the negatively biased back p+ contact and will be absorbed, and the electrons will be attracted to the front side of the detector where they will be collected by a local potential minimum below the registers as illustrated in figure 1.4.

During this process in the depletion region, drift and diffusion all the negatively charged electrons are stored in a depth of 7µm below the front side of the detector [51]. The resulting charge distribution has approximately Gaussian shape. If the negatively charged electrons extend over a pixel boundary, they will be collected in more than one pixel (75×75 μm^2 pixel size).

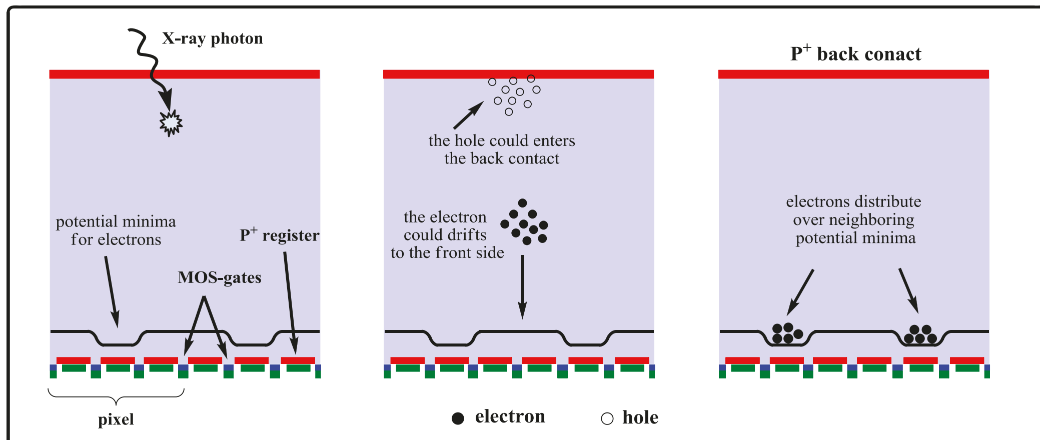

Figure 1.4 Charge collections in the pn-CCD detector. If X-ray photon hits a pixel border, the signal electrons spread over the two neighboring potential minima.

2.2.3. Charge Transfer

Since each pixel in the pn-CCD detector holds three registers, the transfer mechanism of the charge can be accomplished by a three phase transfer mechanism (Φ1, Φ2, Φ3). In order to accumulate the charge and store it from redistributing during the transfer, one or two of the registers are biased to a potential minimum that holds the charges, while the remaining registers have to be reversed in potential.

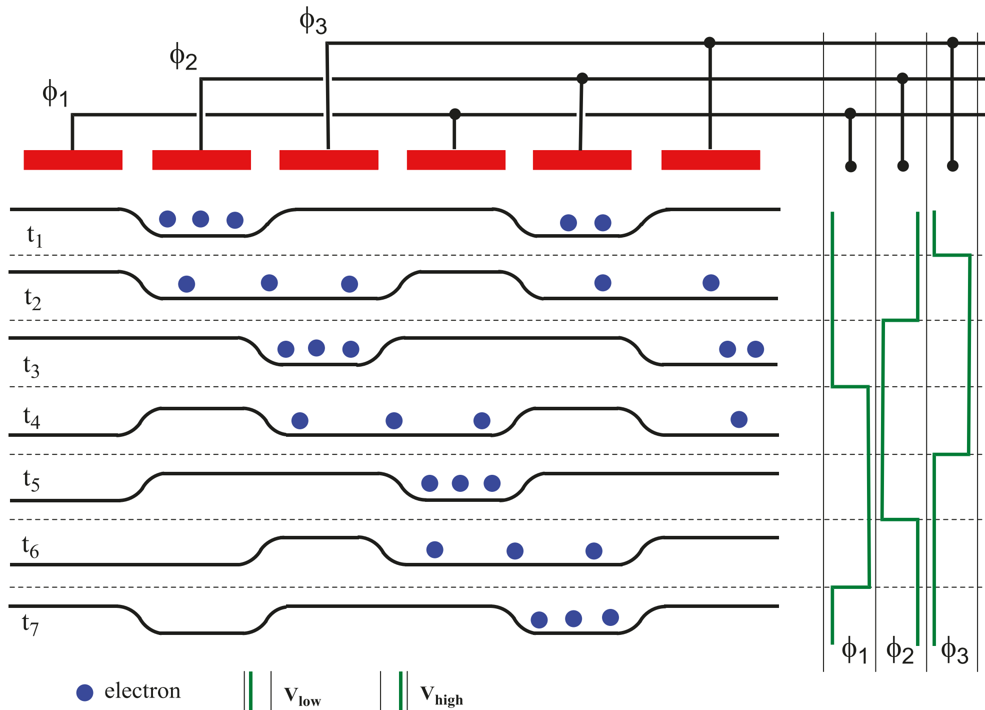

Figure 1.5 Charge transfer in three phases CCD.

As depicted in figure 1.5, the transfer mechanism can be described as follows: at time t_1, the second register contacts with a positive voltage. This leads to creation of a potential minimum that stores only the electrons below this register area, while the other registers protect the electrons from re-distributing to the neighboring pixel. After that, at time t_2, the third register contacts with a positive voltage in addition to the second one. This will cause a re-distribution of electrons below these two register areas, so the electrons stay in their local potential minima. Then at time t_3, only the third register contacts with a positive voltage. Therefore the electrons will only accumulate under the third register. Sequential re-distribution of electrons under each register will continue at times t_4, t_5, t_6 and t_7 and so on.

Simultaneous high and low voltages on the registers adjust the potential well. Thus an effectively transfer is occurring for all the charge (electrons) into its neighboring pixel. Repetition of this process leads to transfer of all detector

charge from one pixel to the next and as a result the signal will be shifted toward the readout anode.

2.2.4. Read out electronics

The CAMEX read out ASIC forms the heart of the read out stage in the pn-CCD detector. This CAMEX (CMOS Amplifier and Multiplexer) ASIC (Figure 1.6) performs the amplification, filtration, and shaping of the pn-CCD signals. It has 384 identical readout channels which carry out the parallel line by line readout. Each channel has a dedicated JFET which is located close to the readout anode. The different components of the CAMEX channels are described below:

- Each CAMEX channel begins with the current source pre-amplifier which converts the charge signal of the pixel into a measurable voltage signal for the JFET on the pn-CCD. This device can also be called a current to voltage converter.
- JFET amplifier which is connected to different combinations of capacitors that can control the option of gain signal.
- A passive low pass filter, which follows the JFET amplifier filters. The signal passing through this stage will be filtered and integrated from high frequency noise.
- Multi-Correlated Double Sampling (MCDS) filter, which consists of eight identical capacitors controlled by eight switching transistors. The signal is also sampled eight times and integrated both before and after shifting the signal electrons on the readout anode. Sampling the signal several times and integrating the results act as a low pass. Due to high frequency noise, fluctuations of the signal are roughly reduced with the square root of the number of samples.
- Sample and Hold stage, where the two deferent integrated signals produce the final electron signal which is stored in the sample and hold circuit.

- Finally the signal, which stored in the sample and hold circuit, is serialized by the Multiplexer of the CAMEX over all the channels before the signal is delivered to the external ADC board.

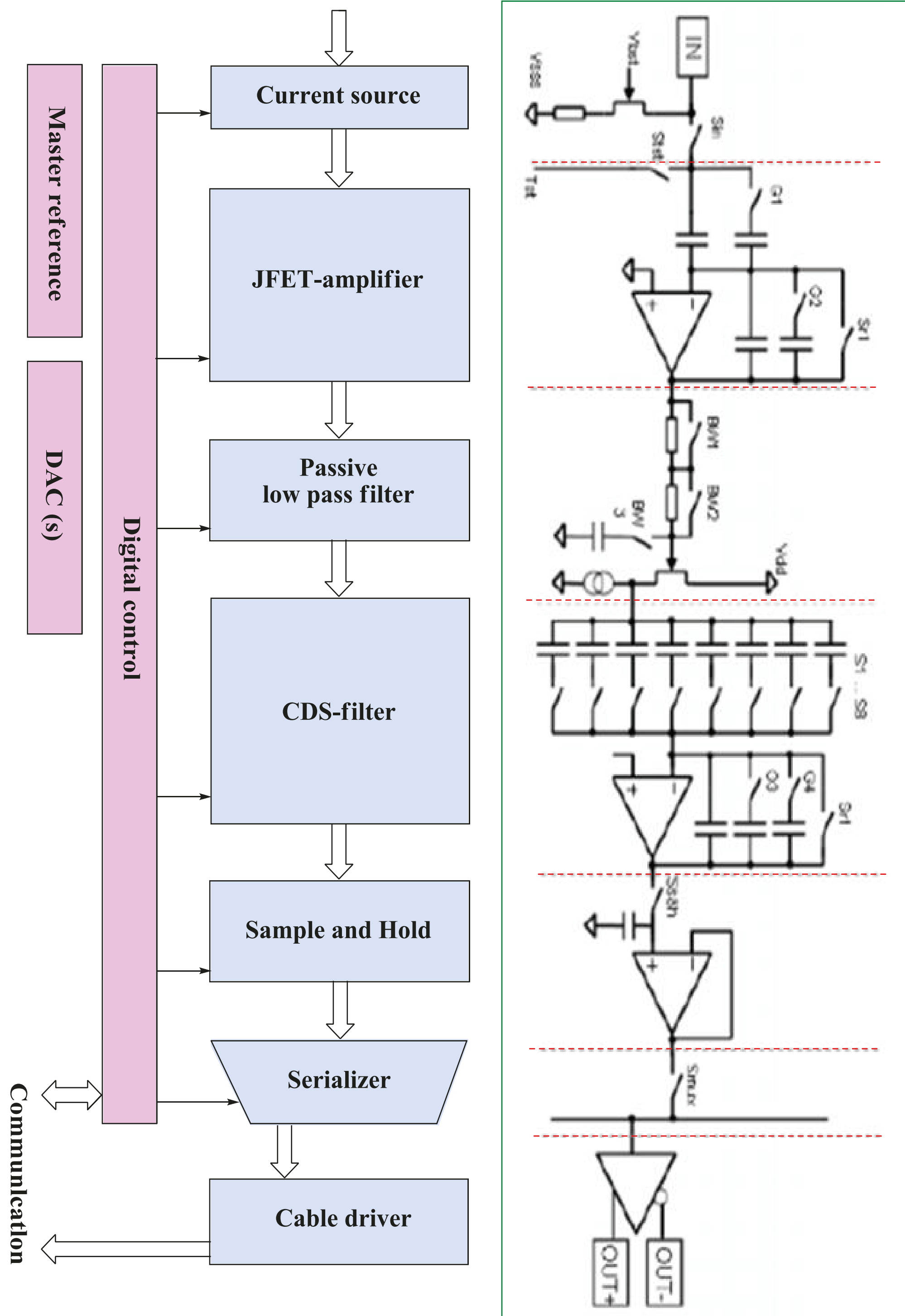

Figure 1.6 Schematic drawing of the CAMEX 384 chip showing the signal flow though the ASIC components .The generated electron signal will be amplified and filtered before being serialized and shifted to an external analogue to digital converter (ADC) [47].

2.3. Quantum efficiency

The quantum efficiency ($\mathcal{E}$) defines in the following equation (2.2) as the ratio number of generated electrons signals (N) to the number of photons (N_0) hitting the surface of pn-CCD detector:

$$\mathcal{E} = \frac{N}{N_0} \tag{2.2}$$

There are many external factors that can affect the quantum efficiency of the pnCCD. One of the most important factors is the energy of photon energy itself. The probability for absorption of a given photon by the CCD material is defined by the attenuation coefficient μ_{Si}, such that the ratio between the detectable photons (I_{det}) and number of the incident photons (I_{in}) hitting the active area of silicon (Si) chip. Let's denote the thicknesses of the Silicon chip and the housing window in front of pnCCD detector by d_{Si} and d_{wi} ,respectively, and μ_{Si} as the attenuation coefficient of this window. Both μ_{Si} and μ_{wi} depend exponentially on the energy of the incident x-ray beam. However, for more accurate calculations, one should take into account the relation between the distance covered by the ray and the incidence angle (2Θ) of the incoming radiation with respect to the normal of the detector's plane. It follows that the effective thickness is $d/\cos(2\Theta)$ as shown in figure 1.7 [49, 117].

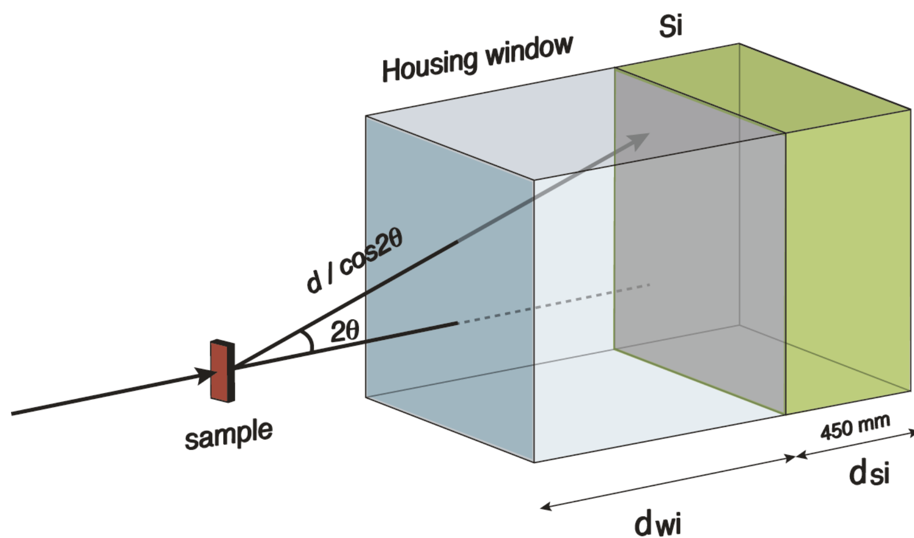

Figure 1.7 The traveling distance of the photon from d into d/cos2θdepending on the incident angle beam.

Hence, the quantum efficiency of pnCCD could be written as follow equation (2.3):

$$\mathcal{E} = (1 - e^{-\mu_{Si} d_{Si} / \cos 2\Theta}) e^{-\mu_{wi} d_{wi} / \cos 2\Theta} \tag{2.3}$$

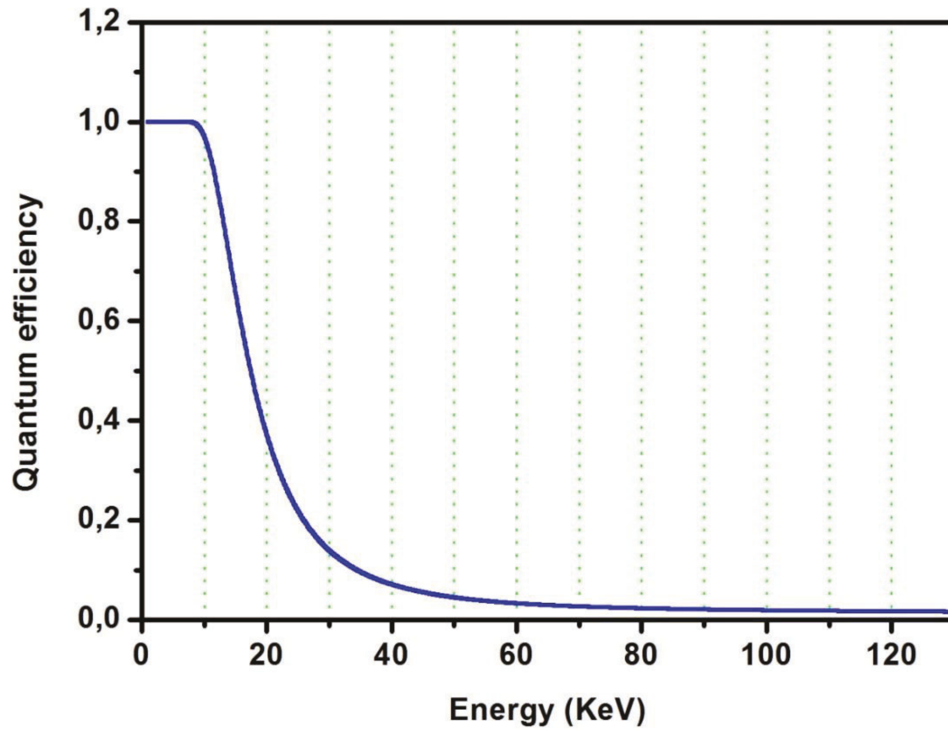

Figure 1.8 Quantum efficiency with the window of the pn-CCD detector with a fully depleted thickness of 450 µm over an energy scale ranges up to 130 keV.

Figure 1.8 shows the quantum efficiency of the pn-CCD detector as function of photon energy. It clearly indicates that the detection efficiency of the detector is close to 100 % for photons in the energy range from 3 keV up to 10 keV and then starts to decreases slowly reaching 5% at 45 keV and less than 2% above 90 keV [51].

2.4. Physical properties of the pnCCD

Many factors related to the incident beam affect the quality of the image such as the energy and the angles of the incident photons and experimental factors as operating mode, frames rate and pixel size.

2.4.1. Position resolution

The pnCCD is position sensitive detector since the interaction position of the photons can be addressed up to a certain resolution. The position resolution of the detector depends on the pixel geometry. Each pixel in the pnCCD is composed of three registers and it has square shape of 75 µm*75µm. Since the middle register is the storage one and the other two registers are barrier registers, the response function is essentially box-like. Therefore, the spatial resolution is equal to the register's pitch. The system works on the principle of photon-charge conversion, the volume of the created charge cloud determines the spatial resolution. In addition, the charge cloud diameter plays an important role in determining the spatial resolution, in which the cloud may be splits over more than one pixel if it size exceeds one pixel size. The charge cloud radius is proportional to the photon energy in which 5keV photon creates a cloud of diameter about 19 µm, 22 µm for 12 keV and 23 µm for 18keV photon [50, 51,117]. This implies that for soft x-ray, the spatial resolution is much better than that in case of hard x-ray where the electron cloud size may exceed the pixel size. Another factor that can affect the spatial resolution is the scattering angle 2θ of the incident photon with respect to the CCD normal.

The primary charge cloud, represented by the number of electrons which are generated from the interaction of photon with the silicon atom, is pushed from the interaction position toward the front side via the driving force of the electric field (E) in figure 1.9. During the drift and due to the influence of the diffusion and mutual electrostatic repulsion, the charge cloud expands as the square root of drift time in the diffusion case and cubic root of drift time in the case of repulsion. This phenomenon is so called Parallax effect [51, 117]. Such events need

correction depending on the chip thickness and on the interaction point in depth. Thus for high energetic photons, the conversion of the photons take place near the store registers (in case of back illuminating detectors). Consequently the deviation from the real position is smaller compared to those interacting near the back side.

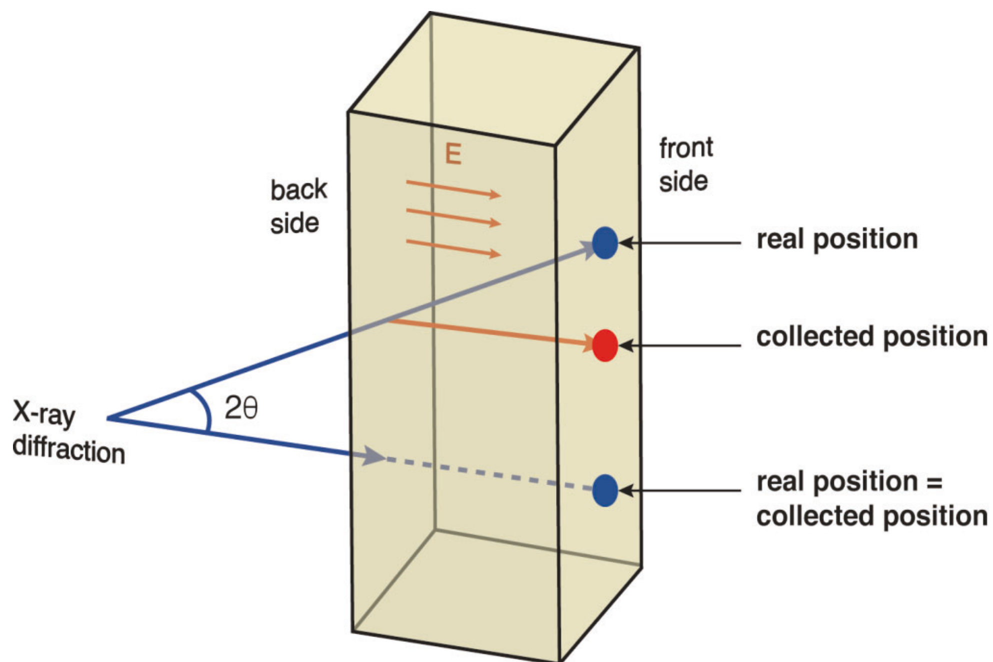

Figure 1.9 Parallax effect. As the conversion point take place far from the pixels side, as the spatial resolution become less.

Furthermore, out-of-time events are considered as rejected events. During the readout process of the image after each frame, and if there is no shutter to stop the flow of the incoming photons, many events influence the transferring image. These events cause a smearing of the transferring image resolution. Such events can be reduced by operating the pnCCD by a fast frame rate. It was the main reason behind the Frame Store mode idea which reduces the out-of-time events [51, 117].

2.4.2. Energy resolution

The ability of the pn CCD detector to discriminate two energies close to each other is characterized by the energy resolution of the system and depends essentially on the system noise of the system. The energy resolution of registered electrons can be determined by the FWHM of the Gaussian distribution taken with the X-ray spectrum. The CCD material, equivalent noise charge (ENC) during the charge transfer and signal amplification play a main role in determining the energy resolution of the system. This can be explained by the following relation (2.4) [52, 53, 54,51 ,117].

$$FWHM(E) = 2.355\omega\sqrt{\frac{FE}{\epsilon} + ENC^2} \quad (2.4)$$

Where $F = 0.115$ is the Fano factor for Si. ENC includes the different noises that are produced at different positions of electron (on-chip electronics, amplifiers, CAMEX and the leakage current due to thermal conditions). Such noises are unavoidable for real detector. But it can be reduced by cooling to very low temperature. Using suitable window materials, one can absorb the optical photons and other external low energetic photons from entering the CCD active area [51, 117].

2.4.3. Time resolution

The sum of the exposure time, charge transfer and readout times form the cycle time and the frame rate. This rate varies from one pnCCD model to another and from one mode of operation to another. For example, the pnCCD with 384x384 pixels operating with frame store mode, the complete cycle time is 11.28 ms while for 256x256 modules this time is reduced to 7.5 ms [50]. Rising the exposure time leads to more integrating events. But at same time, this causes more out-of-time events. The frame rate and consequently the time resolution of pnCCD can be improved by means of pixel binning (timing mode). By this mode, the charges of several adjacent pixels are integrated together as they belong to one “large pixel”. The integrated charges are then transferred to the next “large

pixel” and so on. For example, for 2-fold pixel binning, the charges from two rows are merged together and are transferred into the next two pixels and so on until they reach the readout node. 4,8,16 and more-fold binning is possible and this leads for a proportional reduction of the cycle time (half of the original time in case of 2-fold and quarter time for 4-fold binning) [53,54, 117]. However, mixing of several pixels together reduces the position resolution of the produced image. Hence, the timing mode has advantage for the applications for time resolved process where spatial resolution is of less importance [117].

Chapter 3

3. Semiconductor nanowires

In this chapter, we will discuss an overview of the epitaxial growth semiconductor. In section 3.1 motivation and challenges of the epitaxial growth semiconductor. And In section 3.2 Techniques for nanowire growth.

3.1. pitaxial growth of semiconductor nanowires

Nanowires are Quasi-one dimensional nanostructures, with lengths greater than 1 μm and with diameters typically less than 150 nm. Their unique shape grants significant features for designing novel devices [55], surface effects [56], and thermoelectric [57], strain relaxation properties [58]. Consequently, one dimensional semiconductor nanostructure, such as nanowires , nanowire heterostructures and nanotubes are candidates for next generation electronic and photonic devices because of the low power consumption caused by the strong lateral quantum confinement effects [59, 60]. For this reason, the field of semiconductor NWs becomes one of the most active research areas within a nanoscience community within the past decade.

Many applications of semiconductor nanowires for nanodevices have been demonstrated, such as NWs diodes [61, 62,63,64], lasers [65,66,67,68,69,70,71], photodetectors [72, 73, 74], field effect transistors [75,76,77,78,79,80], single-electron transistors and memory devices [81, 82, 83, 84, 85], field emission electron sources [86], solar cells [87,88,89,90], waveguides [91], single photon sources [92], integrated photonic circuits[93,94], biosensors [95],biostimulants [96] etc.

Among semiconductor nanowires, III–V nanowires show particular promise. Many nano-scale devices have been created using III-V nanowires. The superior optical and electrical properties of III–V materials, including their high electron

mobility and direct band gap, make III–V nanowires ideal for optoelectronic and electronic device applications.

GaAs nanowires have direct bandgap and show high electron mobility. The GaAs material is utilized largely in electronics industries. Therefore GaAs nanowires are major candidates for active nanodevices such as lasers, solar cells. InAs nanowires have significant merits due to very high electron mobility and anarrow bandgap (0.36eV) compared to other semiconductors as shown in figure 3.1. Therefore InAs is extremely promising for applications, especially for use in high frequency electronic devices. InGaAs nanowires have significant features due to the paramount importance of the InGaAs nano material, such as integrated photonics circuits and long wavelength optical transmission. Furthermore, the monolithic integration of III-V nanowires on substrate such as Si or GaAs by direct epitaxial growth enables new possibilities for the design and manufacturing of the optoelectronic and electronic devices.

Moreover, nanowires can be fabricated into radial and axial heterostructures, which have wide and varied applications in nanodevice. Nanowire heterostructures including a wide range IV materials and III–V materials such as Si and In have been carried out. In spite of, the large structural mismatches, thermal and chemical between these highly various materials, High resolution crystallographic are necessary to determine strain relaxation of Nanowire heterostructures.

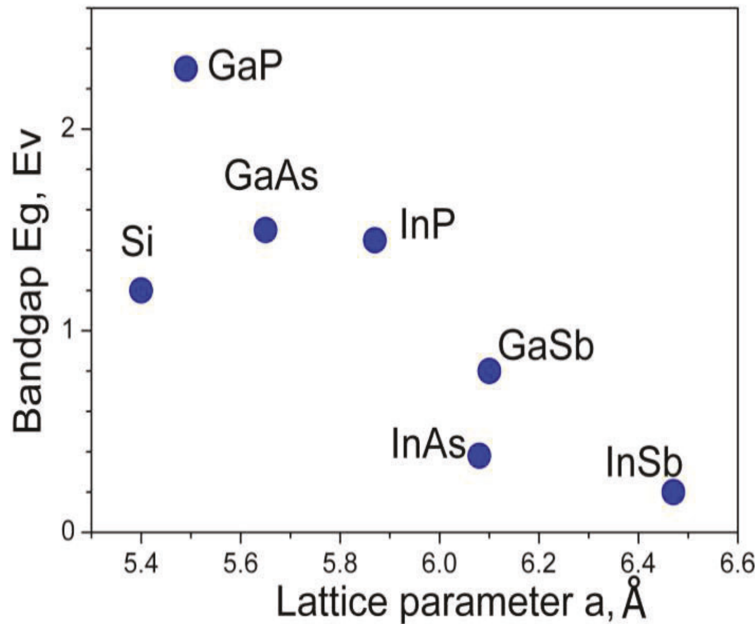

Figure 3.1 shows the energy band gap and lattice parameter of semiconductor nanowires.

The III–V semiconductor nanowires exhibit outstanding potential such as nano-building blocks for nanoelectronic and nanophotonic devices and systems. Different fabrication methods are available to grow semiconductor nanowires. These can be divided into two general strategies: top-down and bottom-up methods [97].Whereas the top-down approach begins with bulk material, from which nanowires are patterned via a etching and combination of lithography such as using electron beam lithography [98] defining the nanostructures. On the other hand the bottom-up approach depends on the chemical synthesis of nanowires. The nanowire properties can be accurately tuned and controlled during the epitaxial growth. As compared with top-down methods, the bottom-up approaches offer opportunities for the fabrication of atomically precise, complex devices in terms of future physical and economic limits [99].

The work presented in this thesis employs the bottom-up strategy for the fabrication of InAs, GaAs nanowires, GaAs/InGaAs/GaAs core-shell nanowires by molecular beam epitaxy (MBE) and metal organic chemical vapor deposition (MOCVD).

3.2 Techniques for nanowire growth

The detailed process of NW growth that applies for different growth techniques and mechanisms is still in development and research such as vapor-liquid-solid (VLS) [100], vapor-solid-solid (VSS) [101], vapor-solid (VS) [102] mechanisms etc. Among all vapor-based methods, the VLS process seems to be most successful for generating nanowires with single crystalline structures and relatively large quantities. Since this thesis concerns in MOCVD and MBE growth of III-V NWs using the VLS mechanism, we shall briefly provide a brief overview of this growth scheme.

3.2.1 Vapor-liquid-solid (VLS)

The VLS mechanism is the most widely cited growth method. The VLS mechanism was originally proposed by Wagner and Ellis in 1964 [103] to explain the anisotropic growth of Si wires catalyzed by metallic Au particles. The name of VLS mechanism refers to the fact that the source material from the vapor passes through a liquid droplet and finally ends up as a solid. So, the VLS process can be described by three steps with a supply phase, a collector phase and a crystalline solid phase in figure 3.2. The first step is the formation of the liquid alloy droplet which contains Au as catalyst and the source materials, the surface of the liquid has a large accommodation coefficient and is therefore the preferred site for deposition. The second step is the crystal nucleation upon gas adsorption and super saturation, the liquid becomes supersaturated with material supplied from the vapor, and crystal growth occurs by precipitation at the solid liquid interface. The last step is the axial growth from the crystalline seeds to form nanowires. Unidirectional growth is the consequence of the anisotropy in solid–liquid interfacial energy.

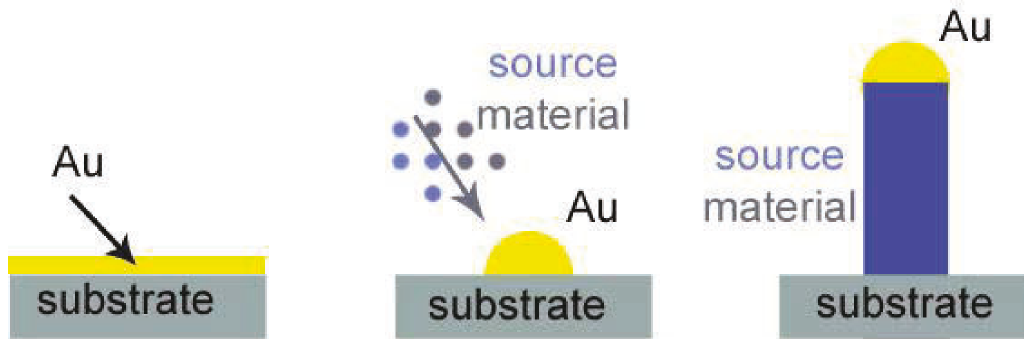

Figure 3.2 Growth scheme of semiconductor nanowires via Au-assisted VLS growth [105].

One can understand the super saturation in the second step of the VLS process which related to term of chemical potential "μ" of a thermodynamic system which is the amount of energy change of the system if an additional particle is introduced, with the entropy and volume is held fixed [104]. If a system contains more than one species of particle, there is a separate chemical potential associated with each species, defined as the change in energy when the number of particles of that species is increased by one. In crystal growth the super saturation, which is the thermodynamical driving force for growth, is the difference ($\Delta\mu_{sk}$) in the chemical potentials of the atomic species in the supply phase "μ_s" and the solid crystalline phase "μ_k". When the chemical potential difference ($\Delta\mu_{sk}=\mu_s-\mu_k$) is positive ($\Delta\mu_{sk}>0$) than the system is super saturated. If it is zero ($\Delta\mu_{sk}=0$) then the system is at equilibrium and there is no driving force for crystal growth and if it is negative than system is under saturated and there is a thermodynamic driving force for desorption of material from the crystal into the supply.

In case MOCVD and MBE growth, the existence of a plain or patterned SiO_x surface has always been linked to this kind of growth, whose role has still to be addressed. In this case, the substrate covered with a oxide layer is heated up to growth temperature of NW material. The oxide layer starts to evaporate and holes are forming in the oxide layer determining the locations for NW growth. The source material should be supplied in the correct sequence. The group III elements accumulate in the holes and create seeds. Then group V material should

be supplied. After supersaturating of the catalyzes the growth process is starting. After the growth, fluxes of source components stop and the whole system cools down as sow in figure 3.3 [105].

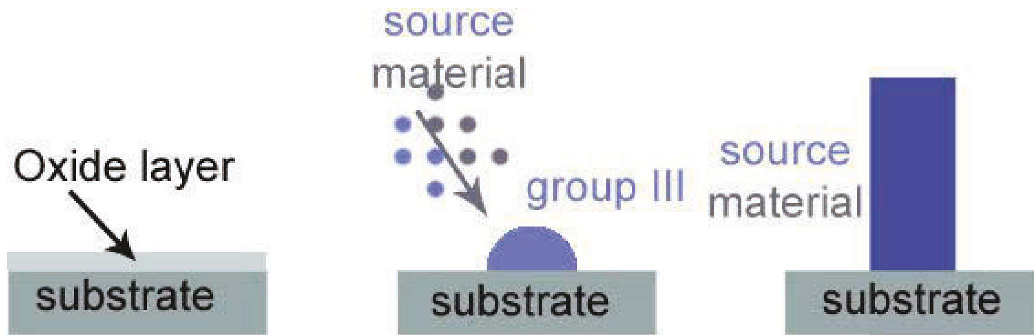

Figure3.3 shows the steps of the self-assisted growth mechanism [105].

3.3. Crystal Structure of NWS growth

The nanowire growth mechanisms is highly successful for many material systems, such as GaAs , InAs, GaAs/InGaAs/GaAs core shell NWs. These NWs grown by self-assisted MBE or MOCVD adopt the cubic zinc blende (ZB) structure. However, GaAs NWs often exhibit a mixed crystal structure with zincblende and wurtzite (WZ) segments alternating along the NW axis which does not exist in the bulk phase [106, 107] as shown in figure 3.4 (a, b). Due to the reduced number of layers, the geometrical lattice parameter c_{WZ} of this structure is by 2/3 shorter than the cubic one in figure 3.4 (b). In addition, GaAs and other III-V materials are expected to exhibit small deviations in lattice parameters in the WZ phase compared to the ZB one. In table 3.1 summarizes the bulk lattice parameters of the cubic and hexagonal structures of Si and GaAs, respectively [108, 159].

Table 3.1 Bulk lattice parameters of silicon and GaAs at room temperature [107].

	a^c /Å	$a^h = \frac{1}{\sqrt{2}} a^c$ /Å	$C^h = \sqrt{3} a^c$ /Å
Si	5.43102	3.8403	9.4068
GaAs	5.6536	3.9977	9.7923

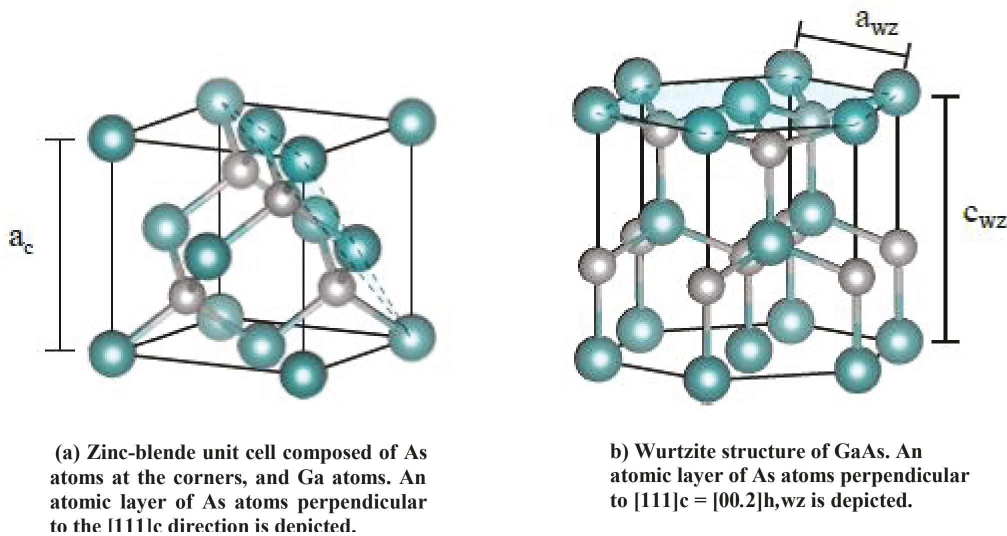

(a) Zinc-blende unit cell composed of As atoms at the corners, and Ga atoms. An atomic layer of As atoms perpendicular to the [111]c direction is depicted.

b) Wurtzite structure of GaAs. An atomic layer of As atoms perpendicular to [111]c = [00.2]h,wz is depicted.

Figure 3.4 Zinc-blende and wurtzite structures of GaAs.

The similarity and the differences of the atomic arrangement of the ZB and WZ crystal structures can be described by their stacking sequences, along the [111] and [0001] directions, respectively. ZB structure has …ABCABC… stacking sequence along [111] directions, whereas WZ structure has …ABABAB… stacking sequence along [0001] directions in figure 3.5.

There are few types of planer defects such as twin planes, stacking faults or hexagonal wurtzite structure mix randomly which may occur in nanowires during the growth along the [111] direction. Twin planes occur when a single bilayer is faultily stacked in a ZB crystal, which reverses the stacking sequence from ABC to CBA. For instance, in the sequence ABCACBA, C is the faultily stacked bilayer which creates the twin plane. The crystal on one side of C is rotated by 60° with respect to [111]B growth axis relative to the crystal on the opposite side.

Stacking faults in (WZ) structures occur when a single bilayer is misplaced, for instance, the sequence ABACACA contains a stacking fault at bilayer C. The crystal structure of the nanowires, including the density of planar crystallographic defects, is determined by the growth parameters as shown in figure 3.6 [159].

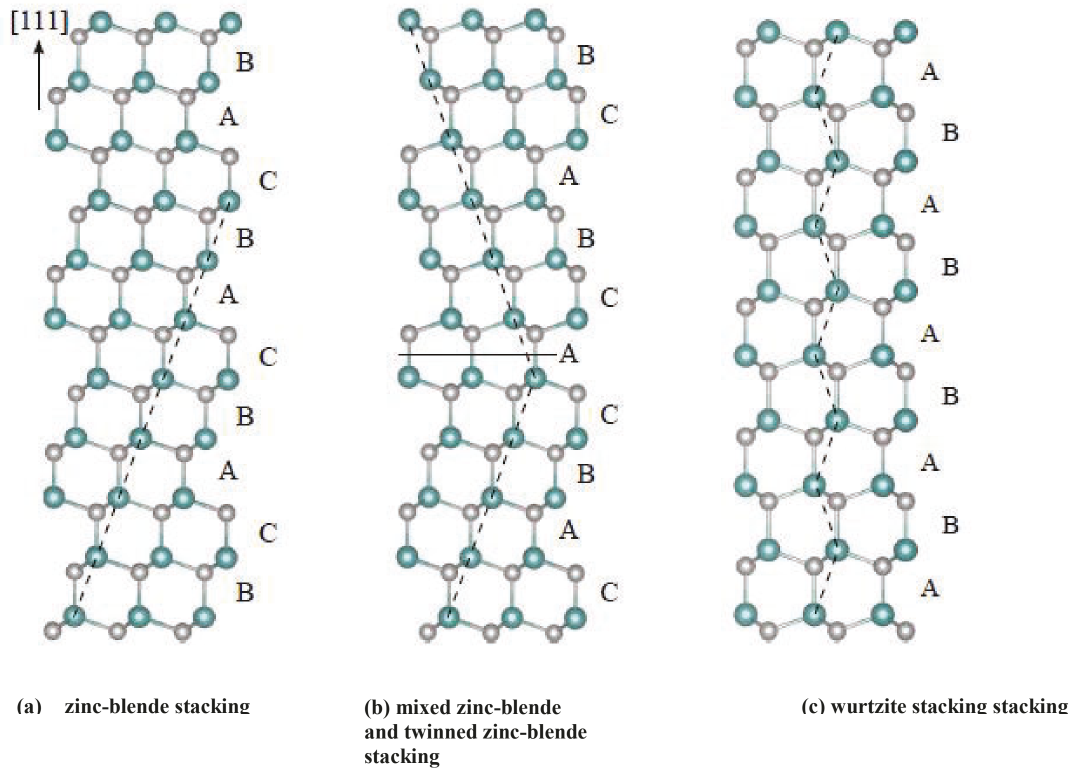

(a) zinc-blende stacking

(b) mixed zinc-blende and twinned zinc-blende stacking

(c) wurtzite stacking stacking

Figure 3.5 Stacking sequences of atomic bilayers along the [111]c and [0001]h direction viewed along $[10\bar{1}]c$. The zinc-blende stacking is a periodic repetition of the '...ABC...' sequence. The twinned zincblende structure is described by an inversion of this sequence into '...CBA...'. The twin-boundary is marked by a horizontal line. The wurtzite stacking is a sequence of alternating layers e.g.'...ABAB...' that can be created by successive nucleation of twin-boundaries.

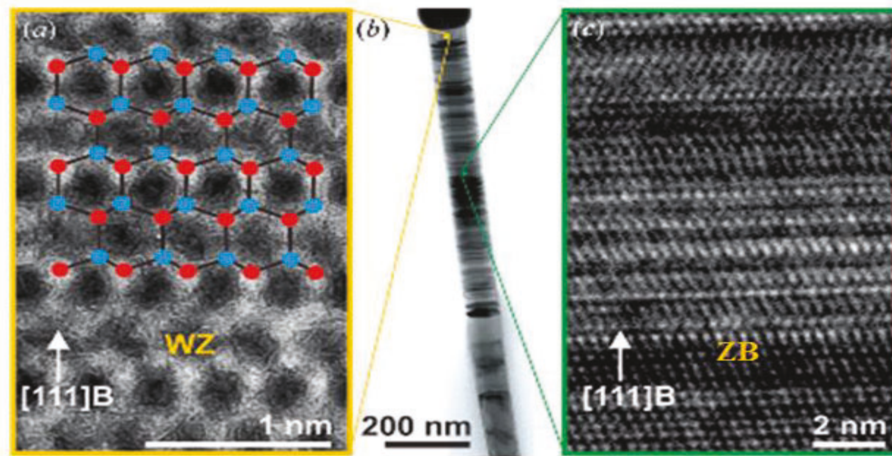

Figure 3.6 High resolution transmission electron microscopy (HRTEM) images of a typical GaAs nanowire: (a) HRTEM image of a WZ region with a simulation of the atom positions overlaid; (b) bright-field image of the top part of the NW;(c) HRTEM image of a ZB region with twin planes and stacking faults [109].

Chapter 4

4. X ray diffraction on crystal

X-ray diffraction is ideally method to investigate the structure of the crystals. The crystals exist naturally in various shapes and colors. As some minerals might be used as decorative objectors, semiconductor crystals are fundamental for technical applications as explained in the previous chapter. But all alike they can be described by two different sets of vectors, which describe the crystal lattice and the arrangement of atoms inside a unit cell. In this chapter will introduce the crystal structure in GaAs, InAs and InGaAs including polytypism, and the basics of kinematic scattering theory with different wavelengths.

4.1. Crystal structure and direct lattice

The smallest building block of a crystal is called unit cell and constructs a crystal by stacking it in all three directions of space. The unit cell defines a coordinate system with lattice vectors $\vec{a}$, $\vec{b}$ and $\vec{c}$ as describing the symmetry of atomic arrangement. Within this unit cell the atomic positions can be described by a vector $\vec{r}$.

$$\vec{r} = u_1\vec{a} + u_2\vec{b} + u_3\vec{c} \qquad (4.1)$$

Where u_1, u_2 and u_3 are the relative positions of an atom with respect to the unit cell origin. Since all individual atoms within the unit cell define a basis of the crystal, the long range order of the crystal is described by unit cell is an infinite lattice and the position $\overrightarrow{R_n}$ of any n-th unit cell is

$$\overrightarrow{R_n} = u\vec{a} + v\vec{b} + w\vec{c} \qquad (4.2)$$

Where u,v,and w are integers.

The unit cell is defined by the vectors, $\vec{a}$, $\vec{b}$ and $\vec{c}$ as shown in figure 4.1, and the volume nof the primitive cell V_c which is given:

$$V_c = |\vec{a} \cdot (\vec{b} \times \vec{c})| \tag{4.3}$$

The angles between the basis vectors are often denoted by:

$$\alpha = (\vec{b}, \vec{c}), \ \beta = (\vec{c}, \vec{a}) \text{ and } \gamma = (\vec{a}, \vec{b}) \tag{4.4}$$

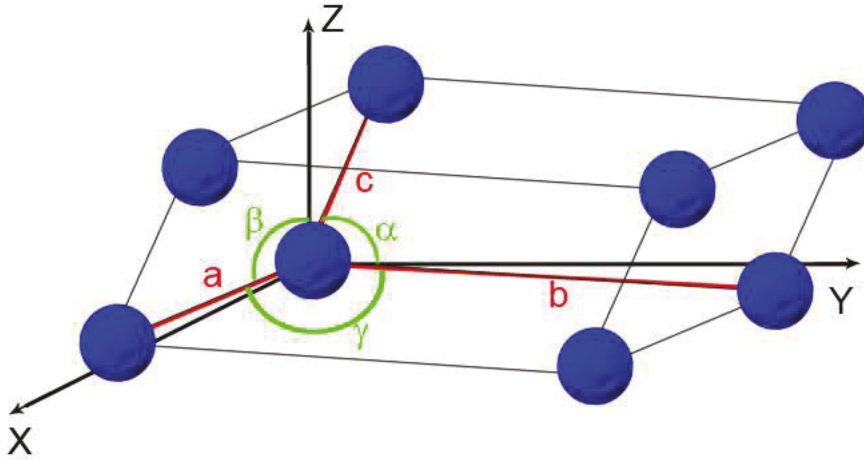

Figure 4.1 Unit cell with lattice parameters a, b, c and angles between basis vectors α,β,$\boldsymbol{\lambda}$.

The symmetry of the unit cell and the whole crystal is described by special angular and spatial relationships between the lattice vectors, like rotations or mirror planes. Based on composition of these symmetry elements seven different lattices characterize every crystal, but only two are relevant for GaAs nanowire systems and will be described in detail. This is the orthogonal cubic lattice with $|a| = |b| = |c|$ and the hexagonal lattice with $|a| = |b| \neq |c|$ and the angle of 90° except for the angle between a1 and a2, which is 120°. a and c are the lattice parameters of the cubic and the hexagonal crystal lattice, respectively. The simplest form of a lattice is the primitive lattice, where an atom is found at every corner of the unit cell. A cubic lattice, which has additional atoms at each facet center, is called a face centered cubic (fcc) lattice. The diamond lattice is composed by two fcc-lattices, which are shifted by 1/4 to each other along the space diagonal of the cube. Similar to Carbon and Silicon (Si) also binary

compounds as Gallium-Arsenide (GaAs) crystallize in this way, where one of the two fcc-sub lattices is filled with Gallium and the other with Arsenic atoms, respectively. As symmetry and regularity play important roles in the description of a crystal, it is helpful to describe planes (*h,k,l*) within the crystal in terms of interceptions ($\frac{a}{h}, \frac{b}{k}, \frac{c}{l}$) and angles of 90° except for the a and c are the lattice parameters of the a and the with the axes (a, b, c). The distance d_{hkl} between two planes with the same Miller Indices (*h,k,l*) has to be calculated for each lattice individually.

4.2. Reciprocal Lattice

The reciprocal lattice was introduced a mathematical construction useful for crystal planes indexing and further description of scattering by P. P. Ewald in 1921. One of the definitions for reciprocal lattice is the following consider a plane wave e^{ikr} . It will only have the periodicity if the following condition is fulfilled for all vectors r

$$e^{i\vec{k}(\vec{r}+\vec{R})} = e^{(i\vec{k}\vec{r})} \; ; e^{(i\vec{k}\vec{R})}=1 \tag{4.5}$$

The set of all wave vectors in three dimensions, which gives a plane wave with periodicity, is called the reciprocal lattice. We label the reciprocal lattice vectors by $\vec{G}$ [110],[111].

The basis vectors of the reciprocal lattice can be written as:

$$\begin{array}{ccc} \vec{a}.\vec{a^*} = 2\pi & \vec{b}.\vec{b^*} = 2\pi & \vec{c}.\vec{c^*} = 2\pi \\ \vec{b}.\vec{a^*} = 0 & \vec{a}.\vec{b^*} = 0 & \vec{a}.\vec{c^*} = 0 \\ \vec{c}.\vec{a^*} = 0 & \vec{c}.\vec{b^*} = 0 & \vec{b}.\vec{c^*} = 0 \end{array} \tag{4.6}$$

The vectors $\vec{a^*}$, $\vec{b^*}$ and $\vec{c^*}$ represent the reciprocal basis vectors and they are related to the vectors of the direct lattice by the relations:

$$\vec{a^*} = \frac{2\pi}{v}.\vec{b}\times\vec{c} \;, \quad \vec{b^*} = \frac{2\pi}{v}.\vec{a}\times\vec{c} \quad , \quad \vec{c^*} = \frac{2\pi}{v}.\vec{a}\times b \tag{4.7}$$

Where the unit cell volume is given by the equation (4.3).

As far the crystal is a periodic system of the atoms, the reciprocal lattice can be obtained by Fourier transformation of the real crystal lattice.

In this case the vector of a certain lattice plane is normalized.

$$\overrightarrow{N} = \frac{1}{2\pi} \cdot (n_1\overrightarrow{a^*} + n_2\overrightarrow{b^*} + n_3\overrightarrow{c^*}) \quad (4.8)$$

And the distance of the lattice plane from origin is defined by:

$$D = \overrightarrow{N}\overrightarrow{R} = n_1 u + n_2 v + n_3 w \quad (4.9)$$

Where is formed by equation (4.2). If a lattice plane crosses the coordinates axis in the points a_0, b_0, c_0 equation (4.9) can be rewritten by

$$\vec{D} = n_1\overrightarrow{a_0} + n_2\overrightarrow{b_0} + n_3\overrightarrow{c_0} \quad (4.10)$$

Based on equations (4.7) and (4.8) we can write the lattice plane equation:

$$hu+kv+lw=m \quad (4.11)$$

Where *h,k,l* are integer. With certain suitable values of define *m,h,k,l* as:

$$h = \frac{m}{\overrightarrow{a_0}}, k = \frac{m}{\overrightarrow{b_0}}, l = \frac{m}{\overrightarrow{c_0}} \quad (4.12)$$

Using these equations, we can write the reciprocal lattice vector, which is along perpendicular to the real lattice by:

$$\overrightarrow{G} = h.\overrightarrow{a^*} + k.\overrightarrow{b^*} + l.\overrightarrow{c^*} \quad (4.13)$$

where *h,k,l* are called Miller's indices.

With the help of the equation (4.13), we can define the angle between two lattices planes as the angle between corresponding normal's to these planes by:

$$\cos\psi = \frac{\overrightarrow{G_1} \cdot \overrightarrow{G_2}}{G_1.G_2} \quad (4.14)$$

Moreover, we may calculate the distance between two neighboured lattice planes of the same orientation by:

$$d_{hkl}^2 = \frac{1}{|\vec{G}_{hkl}^2|} = \frac{1}{(h.\overrightarrow{a^*} + k.\overrightarrow{b^*} + l.\overrightarrow{c^*})^2} \quad (4.15)$$

In such a way, the real space distances are connected with reciprocal space interpretation. If we consider a denominator of the right part of the equation:

Where: $(h.\overrightarrow{a^*} + k.\overrightarrow{b^*} + l.\overrightarrow{c^*})^2 = (h.\overrightarrow{a^*} + k.\overrightarrow{b^*} + l.\overrightarrow{c^*}).(h.\overrightarrow{a^*} + k.\overrightarrow{b^*} + l.\overrightarrow{c^*})$ (4.16)

$$\frac{1}{|d_{hkl}^2|} = h^2.\overrightarrow{a^*}^2 + k^2.\overrightarrow{b^*}^2 + l^2.\overrightarrow{c^*}^2 + 2kl.\overrightarrow{b^*}.\overrightarrow{c^*} + 2lh.\overrightarrow{c^*}.\overrightarrow{a^*} + 2hk.\overrightarrow{a^*}.\overrightarrow{b^*} \quad (4.17)$$

$$\frac{1}{|d_{hkl}^2|} = h^2.\overrightarrow{a^*}^2 + k^2.\overrightarrow{b^*}^2 + l^2.\overrightarrow{c^*}^2 + 2klb^*c^*\cos\alpha^* + 2l\,hc^*a^*\cos\beta^* + 2hka^*b^*\cos\gamma^* \quad (4.18)$$

The interplanar distance can be evaluated through the parameters of the direct lattice by substituting for the magnitudes a^*, b^* , $c^*$and and for $\cos\alpha^*$, $\cos\beta^*$, $\cos\gamma^*$ in these two equations. Considering the specifics of crystal system we can calculate interplanar distance for cubic, Tetragonal and hexagonal structure Respectively.

In case of cubic lattice $\alpha^* = \beta^* = \gamma^* = 90°$ and $a^* = b^* = c^* = \frac{1}{a}$

We obtain:

$$d_{hkl}^c = \frac{a}{\sqrt{h^2+k^2+l^2}} \quad (4.19)$$

And for Tetragonal case: $\alpha^* = \beta^* = \gamma^* = 90°$; ; $a^* = b^* = \frac{1}{a}$; $c^* = \frac{1}{c}$

We obtain:

$$d_{hkl}^t = \frac{a}{\sqrt{h^2+k^2+\frac{a^2l^2}{c^2}}} \quad (4.20)$$

For hexagonal one: $\alpha^* = \beta^* = 90°$; $\gamma^* = 60°$; $a^* = b^* = \frac{2}{a\sqrt{3}}$; $c^* = \frac{1}{c}$

Which gives: $$d(h,k,l) = \frac{a}{\sqrt{\frac{4}{3}(h^2+hk+k^2)+\frac{a^2l^2}{c^2}}} \quad (4.21)$$

The Miller indices of $(h'\,k'\,l')^c$ planes can be transformed into the indices $(h\,k\,l)^h$ of a reciprocal lattice point in the hexagonal coordinate system by the following [112 ,113 ,114,115]:

$$\begin{pmatrix} h \\ k \\ l \end{pmatrix}_h = \begin{pmatrix} 1/2 & 0 & -1/2 \\ -1/2 & 1/2 & 0 \\ 1 & 1 & 1 \end{pmatrix} \begin{pmatrix} h' \\ k' \\ l' \end{pmatrix}_c \quad (4.22)$$

and the inverse relation

$$\begin{pmatrix} h' \\ k' \\ l' \end{pmatrix}_c = \begin{pmatrix} 2/3 & -2/3 & 1/3 \\ 2/3 & 4/3 & 1/3 \\ -4/3 & -2/3 & 1/3 \end{pmatrix} \begin{pmatrix} h \\ k \\ l \end{pmatrix}_h \quad (4.23)$$

It is common to add the third index $i = -(h + k)$ for the description of the reciprocal space vectors in the hexagonal surface coordinate system, compare the concept introduced for the directions in the real space lattice [111].

4.3. Bragg's Law

Bragg's law is a consequence of the periodicity of the lattice. The incident beam is reflected by the planes of atoms with angle of incidence equal to the angle of reflection θ. The diffracted beam is likely observed when the reflections by parallel planes are constructive, showing the constructive interference phenomenon. Constructive interference happens when the path difference between two rays crossing two consecutive parallel planes is an integral number of the wavelength of the beam [116,117].

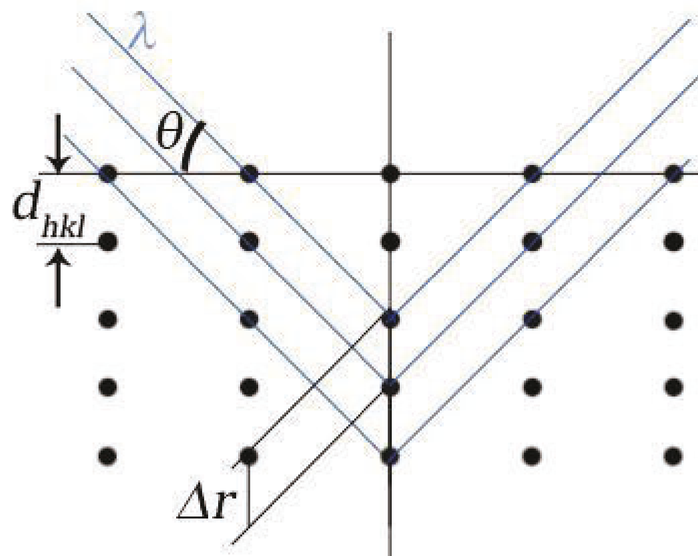

Figure 4.2 Bragg interference conditions.

The waves are scattered from lattice planes separated by the interplanar distance d. When the scattered waves interfere constructively, they remain in phase since the path length of each wave is equal to an integer multiple of the wavelength. The path difference between two waves undergoing interference is given by 2dsin θ, where θ is the scattering angle as see in figure 4.2. This leads to Bragg's law,

which describes the condition on θ for the constructive interference to be at its strongest.

$$2d_{hkl} \sin\theta = \Delta r = n\lambda \quad (4.24)$$

It is equivalent to

$$E = n\frac{hc}{2d_{hkl} sin\theta} \quad (4.25)$$

in energy coordinate, where n : is an integer and defines the order of interference and hc = 12.4 keV Å if d is given in Å.

Bragg's law is based on the elastic reflection of X-rays. In other words $|\vec{k}| = |\vec{k}'|$, where $\vec{k}$ is the wave vector with:

$$|\vec{k}| = \frac{2\pi}{\lambda} \quad (4.26)$$

Although the law is simple and does not provide any information about the arrangement of atoms inside the lattice, it stills provide a microscopic description of the phenomenon of reflection of radiation. This law is experimentally tested in the current work by white beam so that one can calculate the distance d separating a set of parallel planes, by altering the diffraction angles [118,111].

4.4. Bragg condition and Laue equations

In this project, The Laue method is mainly used to determine and characterize the semiconductor NWs. White radiation is reflected from, or transmitted through, a fixed position [119]. The beams diffracted form arrays of atoms lie on the sample to the pnCCD. The Bragg angle is fixed for every set of planes in the NWs crystal. Each set of planes picks out and diffracts the particular wavelength from the white radiation that satisfies the Bragg law for particular values of d and θ. Therefore each curve corresponds to a different wavelength. The spots lying on one curve are reflections from planes belonging to one zone. Laue reflections from planes of the same zone all lie on the surface of an imaginary cone whose axis is the zone axis. Consider the reflection of an incident beam by two neighbor atoms is shown in figure 4.3.

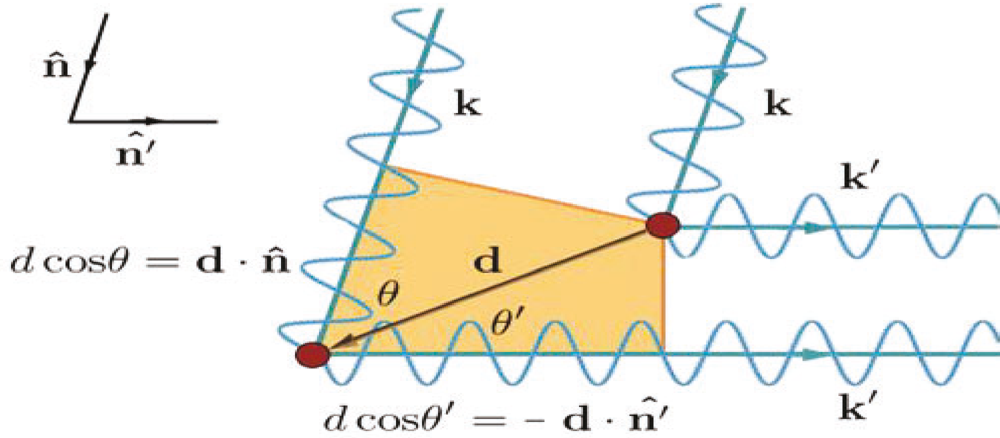

Figure 4.3 Laue diffraction of an incident beam by two neighbor atoms.

The wave vectors of the incident and the reflected beam are given by:

$$\vec{k} = \frac{2\pi}{\lambda}\vec{n} \quad \text{and} \quad \vec{k'} = \frac{2\pi}{\lambda}\vec{n'} \quad \text{respectively,} \tag{4.27}$$

Where $\vec{n}$ and $\vec{n}$'are unit vectors along the direction of the incident and reflected beam respectively.

The path difference between the two reflected beams is:

$$d\cos\theta + \ d\cos\theta' = d.(\vec{n} - \vec{n'}) \tag{4.28}$$

Such that d is the spacing between two lattice points. Similar to the Bragg diffraction, the condition for constructive interference is:

$$\vec{d}.(\vec{n} - \vec{n'}) = m\lambda \tag{4.29}$$

With m is an integer. Multiply by 2π and divide by λ one get:

$$\vec{d}.(\vec{k} - \vec{k'}) = 2\pi m \tag{4.30}$$

This condition will hold true for all possible $\vec{d}$, and thus for all direct lattice basis vectors $\vec{R} = \{\vec{a}, \vec{b}, \vec{c}\}$, fulfilling the relation:

$$\vec{R}.(\vec{k} - \vec{k'}) = 2\pi m, \tag{4.31}$$

Which is equivalent to:

$$e^{i\vec{R}.(\vec{k} - \vec{k'})} = 1 \tag{4.32}$$

Which is the Fourier condition seen in equation 4.5. Therefore $(\vec{k} - \overrightarrow{k'})$ is a reciprocal lattice vector. The magnitude of $\vec{G}$ is given by:

$$\left|\vec{G}\right| = m\frac{2\pi}{d} \tag{4.33}$$

Consider the Laue condition, the $(\vec{k} - \overrightarrow{k'})$ is a reciprocal lattice vector. In other words, the general result of Laue diffraction condition is:

$$\vec{q} = (\vec{\mathrm{k}} - \overrightarrow{\mathrm{k'}}) = \vec{G}_{h,k,l} \tag{4.34}$$

Since the X-ray diffraction by the crystals gives rise to elastic reflections of well-defined energies contained in the primary X-ray spectrum as soon as the Bragg condition is fulfilled, the magnitude of the involved wave vectors remains unaffected according to

$$k = k' = \frac{2\pi}{\lambda} = \frac{E}{\hbar c} \tag{4.35}$$

where $\lambda = \frac{2\pi\hbar c}{E}$ with $\hbar = 6.582 \cdot 10^{-16}$ eVs (Planck constant)nand $c = 2.998 \cdot 10^{8}$ m/s (speed of light). Thus, resulting from (4.22) the magnitude of the scattering vector satisfies

$$q = \frac{4\pi}{\lambda}\sin\theta = \frac{2E}{\hbar c}\sin\theta = \frac{2\pi}{\lambda} \tag{4.36}$$

Since the reciprocal translational vector is $\vec{G}$ in the equation (4.13), the equation (4.32) can be expressed as projection to the three axes of the lattice called the Laue Equations.

$$\begin{aligned} \vec{\mathrm{a}}\,.\left(\vec{\mathrm{k}} - \overrightarrow{\mathrm{k'}}\right) &= 2\pi.h \\ \vec{\mathrm{b}}\,.\left(\vec{\mathrm{k}} - \overrightarrow{\mathrm{k'}}\right) &= 2\pi.k \\ \vec{\mathrm{c}}\,.(\vec{\mathrm{k}} - \overrightarrow{\mathrm{k'}}) &= 2\pi.l \end{aligned} \tag{4.37}$$

Laue diffraction peaks are corresponding to Bragg reflection from direct planes perpendicular to $\overrightarrow{G}_{h,k,l}$. In Laue formulation the spacing between two consecutive parallel planes with Miller indices h, k and l is denoted by d_{hkl} . This spacing could be calculated using equation 4.31 with m = 1:

$$d_{hkl} = \frac{2\pi}{\left|\vec{G}\right|} = \frac{2\pi}{|\vec{q}|} \tag{4.38}$$

4.5. Kinematical scattering theory

Structural investigations of crystals with X-rays are possible because electromagnetic couple directly to electric charges (protons and electrons). But as protons are well localized and concentrated in the atomic core, the interaction of X-rays with matter is almost solely attributed to photon-electron interaction. There are two different theories describing X-ray scattering from matter, a dynamical and a kinematical theory. The dynamical theory treats bulk crystals, where besides multiple scattering at different electrons the photons are absorbed and deposit energy in the crystal. However, nanowires are small and can be treated within the kinematical theory, where only scattering from a single electron is considered. In a simple approximation, X-ray radiation is for most applications considered as an electromagnetic plane wave with amplitude E_0 polarised in ϵ and propagating in direction k. The resulting electric field at a position r is given by

$$E(r,t) = \epsilon E_0 e^{i(kr-wt)} \tag{4.39}$$

Where w is the oscillation frequency and t is the time. In order to calculate the scattered intensity, this is possible if each atom in the crystal is considered and the scattering of all electrons is processed correctly. If the electromagnetic wave encounters an electron, the electric field forces the electron to vibrate and emit itself a plane wave with ϵ' and k'. To quantify the probability to observe scattered intensity $I_{sc} = |r_0^2 E_{sc}|^2$ in a solid angle ΔΩ the differntial cross-section

$$\left(\frac{d\sigma}{d\Omega}\right) = r_0^2 \left|\epsilon.\epsilon^{'}\right|^2 = r_0^2 P \tag{4.40}$$

is introduced. Here r_0 is the classical electron radius and P a polarization factor relating the observation angle with the polarization of the incident plane wave and we will explain it in detail later. Following this approach, first the scattering amplitude for atoms and second for crystals can be derived considering the electrons of each atom placed within the unit cell of a lattice. In an atom the electrons are not localized but described by electron densities $\rho(r)$ that the interaction of X-rays with an atom is described by means of an atomic form factor $f(Q)$

$$f(Q) = \int_{-\infty}^{\infty} \rho(r)\, e^{iQr} d^3r. \qquad (4.41)$$

Kinematical theory is based on elastical scattering of photons, so that the energy incident and scattered wave is the same ($|k| = |k'|$) However the direction of the scattered photons changes compared to the incident X-ray beam and the scattering can be described in terms of the momentum transfer Q as in equation (4.34).

Scattering from a crystal can be factorized to a sum over all atoms j in the unit cell and a sum over all unit cells n:

$$F_{Crystal}(Q) = \underbrace{\sum_j f_j(Q)\, e^{iQ_j r_j}}_{unit\ cell\ structe\ factor} \underbrace{\sum_n e^{iQ_n R_n}}_{Lattice\ sum} \qquad (4.42)$$

In kinematic scattering approach the intensity is proportional to the square of the structure factor, which depends only on the structure within the unit cell, and the form factor related to the shape of the crystal:

$$I(Q) \propto |F(Q)|^2 = F(Q).F(Q)^* \qquad (4.43)$$

In the present work the equation (4.43) can rewrite in the following:

$$I_{hkl} \propto \varepsilon I_0 |F_{hkl}|^2 LPA \qquad (4.44)$$

Here the integrated intensity I_{hkl} of a Bragg peak *hkl* is proportional to various angular and energy dependent factors, ε is the quantum efficiency of the pnCCD at the scattering angle 2θ and the energy *E* of the reflection, I_0 the intensity of the incident white beam at this energy, F_{hkl} is the kinematical structure factor [120] , L is the Lorentz factor which takes into account that in real X-ray diffraction experiments, the Bragg condition cannot only be fulfilled by one specific wavelength and one single incident angle, but within narrow wavelength and angular bands enclosing these values. Therefore the Lorentz factor depends on the method used to analyze the crystal, this mean it is effectively different for measurements performed in the monochromatic mode and in the white-beam mode and for situations with a stationary sample and a rotating sample. In the present case of a spatially fixed crystal exposed to white X-rays, the amounts of Lorentz factor [121,122, 51]

$$L = \frac{\lambda^2}{Sin^2\theta} \qquad (4.45)$$

p is the polarization factor which effects associated of the integrated intensity arises with the nature of the incident beam that are summarized in the following equation[123, 112, 51].

$$P = \frac{1}{2}(1 + cos^2 2\theta) - \frac{1}{2}\tau \cos 2\,\rho\, sin^2 2\theta \qquad (4.46)$$

The first term in (4.45), which represents the contribution of an unpolarized X-ray beam which has applied to diffraction data collected with X-rays generated by a conventional X-ray tube. The second term in (4.46) describes the attenuation of the diffracted intensity due to the polarization of synchrotron radiation, where

$$\tau = \frac{I_{\parallel} - I_{\perp}}{I_{\parallel} + I_{\perp}} \qquad (4.47)$$

τ is the degree of polarization given by the ratio of the components with a polarization direction parallel ($I_{\parallel}$) and perpendicular ($I_{\perp}$) to the plane of the electron orbit in a storage ring. Where the component ($I_{\perp}$) is vanishes in the orbital plane in bending magnet radiation [124, 112, 51]. if the cross section of the synchrotron beam is sufficiently small this mean that $\tau \approx 1$.

$$\rho = \arctan\frac{z}{y} \qquad (4.48)$$

The angle ρ denotes the position of the Bragg peak in the detection plane measured from the horizontal axis. The notation in (4.48) refers to a coordinate system which is defined in such a way that the incident beam direction corresponds to the x-axis, whereas y and z are the horizontal and vertical directions of the pnCCD plane.

The factor A which in (4.43) equation takes into account absorption effects within the sample and its surroundings consisting of a thin-walled glass capillary. Since the utilized NWs is pure, the absorption of hard X-rays with relevant energies above 8 keV inside the sample environment was neglected for further corrections of integrated Laue diffraction spot intensities assuming $A \approx 1$. For typical geometries of NWs experiments, the applied polarization factors have values in the range $0.9 < P < 1$.

In crystallography, various parameters are used to characterize and analyze the quality of diffraction data [125,112, 51]. The achieved resolution, defined as the

minimum distance between two objects in a crystal that can be imaged within the obtained electron-density map, is often approximated by the nominal resolution

$$d_{min} = \frac{\lambda}{2sin\theta_{max}} = \frac{2\pi}{q_{max}} \quad (4.49)$$

The first term in (4.49) corresponds to Bragg's law (4.24) and refers to data collection at a fixed wavelength λ, where $2\theta_{max}$ is the maximum detected scattering angle limited by experimental constraints. The more general second term, resulting from (4.36), can be applied to Laue diffraction using the white beam and pnCCD detector, where the scattering angle and the wavelength are different measurands [51].

Chapter 5

5. Experiment at home ((sectionI)

Before this research was fully conducted, we conducted a preliminary experiment at home using the pnccd detector and nanowires sample and the experimental results were compared with the theoretical results to verify the possibility of follow-up research with the WZ and ZB structure of NWs samples using white beam and pn-CCd detector in following experiments.

X-Ray Diffraction from Periodically Patterned GaAs nanowires Grown onto GaAs[111]B using a pnCCD detector

Summary

We present a high-resolution X-ray diffraction pattern of periodic GaAs NWs grown onto GaAs[111]B surface. The experiments were performed at the home laboratory in Siegen University using a coplanar Bragg reflection with Cu-$K_{\alpha 1}$ radiation and pnCCD detector. The structural properties were probed by measuring reciprocal space maps (q_y, q_z) in the vicinity of GaAs[111] reflection. Besides the peak related to the reflection from GaAs substrate, we found a second peak referring to the reflection from NWs. The lattice mismatch between the NWs and the substrate was 0.34% probably due to probably caused by different lattice parameters of ZB and WZ of GaAs. Despite the high quantum efficiency of the pnCCD at the energy 8 keV the lattice parameters and lattice mismatch between the GaAs NWs (WZ) and the GaAs (111) substrate (ZB) are determined in reasonable agreement with data taken with monochromatic x-rays in range of 0.11%.

5.1. Introduction

Semiconductor nanomaterials, such as NWs and nanotubes (NTs) are candidates for next-generation electronic and photonic devices because of the low power consumption caused by the quantum confinement effects [126]. Therefore, the field of semiconductor NWs becomes one of the most active research areas within a nanoscience community. Many applications of semiconductor nanometerials for nanodevices have been demonstrated, such as diodes [127], field effect transistors, photo diode sensors, and solar cells [128].

Many nanoscale devices have been fabricated using III-V NWs [129].They are ideal for photonic devices due to their direct band gap and superior electrical properties a explained in detail in the third chapter in the thesis. The fabrication of these electronics and photonic NWs based devices demands a high-level control of the growth of respective heterostructures. Although there are obvious improvements in NWs growth and its characteristic, the crystallographic characteristics of NWs is still a difficult task.

The aim of this work is the application of x-ray diffraction methods for the characterization of semiconductor GaAs NWs Grown onto GaAs[111]B with emphasis on the use of micro-focused x-ray beams using pn-CCD detector as the first time in nanoscience field. In addition, calibration and investigation of the pn-CCD performance in collect crystallography data using integrated intensity image and reciprocal space maps.

5.2. The pn-CCD Detector

The pn-CCD detector is a new radiation instrument which showed wide applications for material research, such as white-beam 3D Laue diffraction, multilayer analysis of hard coatings soft matter, and particularly nano-objects [130].

The pn-CCD is a semiconductor array detector, back-illuminated charge coupled device with fully depleted silicon chip thickness of 450µm. This detector was designed and developed in the semiconductor lab of Max-Planck-Institute (München) for space applications and used later for X-rays imaging in the energy range (0.1 keV to 120 keV) [131].

One of the most interesting features of this detector, that it has 100% quantum efficiency up to 10 KeV and drops to 30% at 20 KeV. In addition, the spatial resolution depends on the pixels size which typically is 75 µm. The pixels size can be reduced to few micro meters using a modified center of gravity technique[132].

The pn-CCD detector that is currently used in our lab is divided in two parts namely an image area (384×384 pixels with 75×75 μm^2 pixel size) and frame store area (384×384 pixels with 75×51 μm^2 pixel size). After the x-rays enter the detector volume, they interact with the silicon substrate and create photo-electrons which drift to the front pixilated plan of the detector and stored under the pixel registers. Buckets of stored electrons are shifted in parallel to the read out anode with a 3 phase transfer clock. Further amplification and shaping (8 MCDS) of the signal done and the pixel amplitudes are digitized and sent the data acquisition system for offline analysis and pnCCD detector as explained in detail in the second chapter in the thesis.

5.3. Experiment section

5.3.1. Sample

The used sample is the GaAs NWs grown in periodic arrays by catalyst-free SA-MOVPE throughout a prepatterned 15-nm-thick amorphous SiNx layer onto GaAs[111]B surfaces. The silicon nitride has been deposited by plasma-enhanced chemical vapor deposition at 300℃. Within an area of 250* 250 μm^2, the SiNx layer was partially removed by electron beam lithography, defining an ordered

array of circular openings with diameters of 600 nm in an electron-sensitive resist followed by wet chemical etching using NH4F:HF:H2O solution. The selective area growth was implemented using low-pressure (50 mbar) MOVPE in an AIXTRON AIX200 reactor (Aachen, Germany). Thrimethylgallium (TMGa = 3.75 mL) and arsine (AsH3 = 50 mL) were used as group-III and group-V materials. The total flow into the reactor amounted to 7 slm. The growth temperature was set to 750℃, providing equally hexagonally shaped NWs with uniform spacing. [133, 134] Prior to X-ray measurements, the NR arrays were inspected by scanning electron microscopy (SEM). Figure 5.1 presents SEM pictures of the sample, verifying the uniformity of hexagonally shaped NWs. The sample is a hexagonal array of NWs with diameters of about 380 nm and heights of 400 nm and the sample has been investigated the inter-rod spacing with D = 1 µm (Figure 5.1(a)).

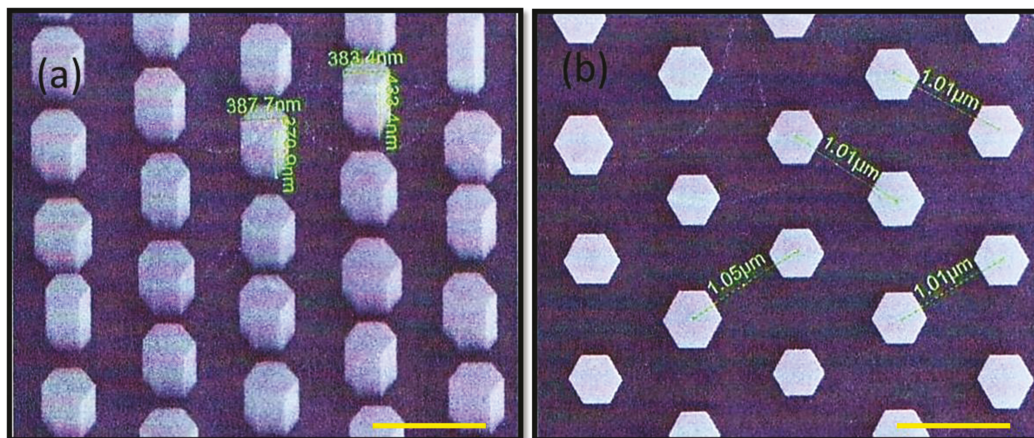

Figure 5. 1 (a) and (b) SEM picture of GaAs[111]+15 nm SiNx+GaAs NR sample grown on GaAs[111]B substrate.The NWs with diameters of about 380 nm and heights of 400 nm (a), the inter-rod spacing of the sample is with D = 1 µm (b). The scale bars in (a) and (b) are 1 µm.

5.3.2. Setup of Experiment

The measurement was carried out at the home laboratory in Siegen University using GaAs NWs on GaAs[111] substrate (Figure 5.2).

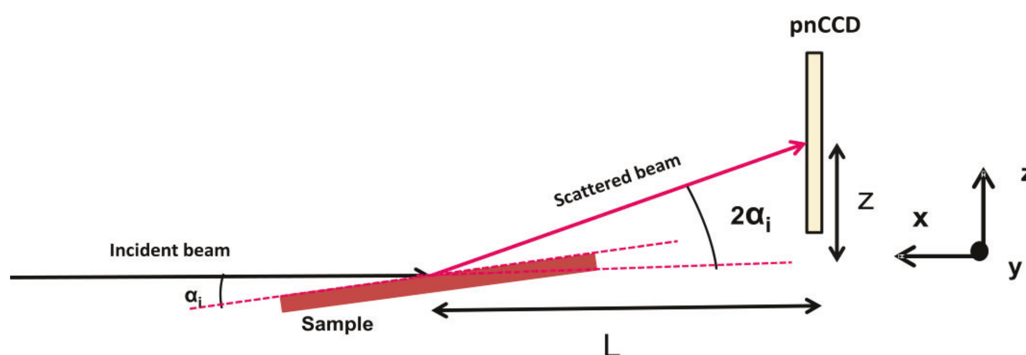

Figure 5.2 The experimental setup used in micro diffraction experiments.

The experimental setup is shown in Figure 5.2. The sample was illuminated by x-ray source at university of Siegen which name Incoatec microfocus source IµS at incident angle α_i = 13.65° for reflection (111), the size of the X-ray beam was focused to the size of (H x V) 50 x 50µm^2 at energy E= 8.048 KeV. A beam stop was used to block the direct beam in front of the detector. The sample to detector distance was 45 mm. After recording the direct beam, the detector moved up a distance Z = 25 mm to detect the reflected signal. The 100 K signal frames frames data sets were recorded at 100Hz in the signal photon counting mode to preserve the energy information.

5.5.3. Incoatec microfocus source IµS

Incoatec (innovative coating technologies) is firm located in Geesthacht near Hamburg was founded in 2002 by scientists from the GKSS research centre together with Bruker AXS in Karlsruhe. The IµS is a microfocus source based beam delivery system that is equipped with a Montel-type multilayer optic [135].

It consists of a 30 W microfocus sealed tube with high brilliance and a high-performance 2D focusing or collimating Quazar multilayer mirror and it is available for Cr-K_α, Cu-K_α, Mo-K_α and Ag-K_α radiation.

The basic equipment includes:

- High voltage generator.

- IμS X-ray source, consisting of tube, tube housing, optics housing and holder as shown in the following figure 5.3.

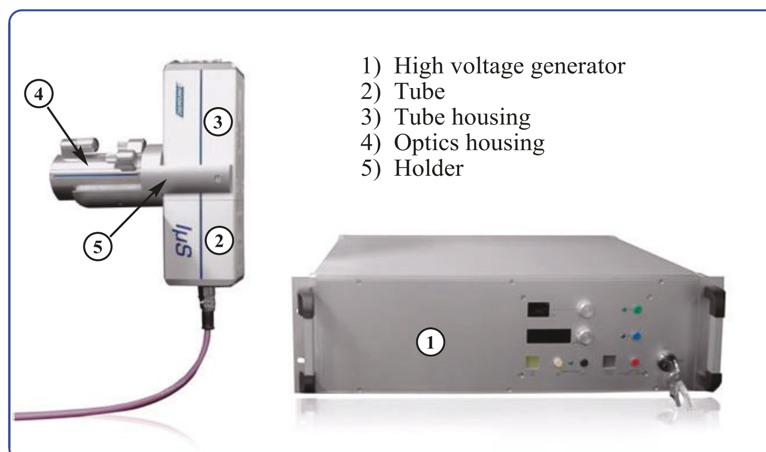

Figure 5.3 Basic Incoatec microfocus source system. Copyright 2007 Incoatec GmbH website.

Compared with other X-ray devices, the IμS offers numerous benefits that can be summarized as follow:

- Long lifetime without maintenance.
- Extremely stable.
- Short warm-up time.
- No water cooling.
- Easy tube replacement.
- Easy adaptable to all common goniometers.
- Low cost of ownership, comparable to common sealed tubes.

5.4. Discussion and results

Integrated intensity image and reciprocal space maps (RSMs) have been recalculated close to the GaAs(111) Bragg reflection using the following equations:

$q_y = 2\pi/\lambda\ (\cos\alpha_f \cdot \sin 2\boldsymbol{\varphi})$ $\qquad$ $q_z = 2\pi/\lambda(\sin\alpha_i + \sin\alpha_f)$

Where λ is the wavelength, $\boldsymbol{\varphi}$ is the plane angle, and α_i , α_f are the angles of incident and reflected beams.

Figure 5.4. shows integrated intensity image and RSMs of GaAs NWs taken at GaAs(111) reflection. Two spots are investigated, one of them related to the reflection from GaAs substrate (ZB) at $q_{z,sub}$ = 19.245 ± 0.008 nm^{-1} and the other spot referring to the reflection from GaAs NWs (WZ) at $q_{z,\,NW}$ =19.181 ± 0.003 nm^{-1}. The lattice parameter of the GaAs substrate in the ZB structure and GaAs NWs in the WZ structure was calculated experimentally and theory using the following equations (4.19) ,(4.21) and (4.38) in the chapter 4.

The lattice parameter of both substrate GaAs in ZB structure and NWs in WZ structure are presented in Table 5.1 Here we calculate the NWs in ZB structure to be able to calculate the lattice mismatch then we calculate the NWs in WZ using the Table 3.1 Bulk lattice parameters of GaAs at room temperature [107] in the chatper 3.

Table 5.1 shows experimental and theoretical of lattice parameter for substrate and NWs.

	lattice parameter [Å]	
GaAs (111)	Experimentally	Theoretically
Substrate (ZB)	a=5.6548 ± 0.0013	5.6532 ± 0.0001
Nanoroads (ZB)	a=5.6737 ± 0.0241	5.6532 ± 0.0001
Nanoroads (WZ)	a=4.0119± 0.0143 c=9.8271 ± 0.0349	a=3.9977 ±0.0001 c=9.7923±0.0001

The experimental results are in good agreement with that of theoretical value. Because the NWs crystallize in the wurtzite phase the lattice mismatch is $\Delta a/a = (a_{NWs} - a_{sub}) / a_{sub}$ with respect to the zinc-blende GaAs substrate is 0.34%. But the lattice mismatch of the sample using monochromatic x-rays is 0.23% [134]. The agreements of the lattice mismatch between the accuracy which can be achieved by the white using PnCCD detector compared with the accuracy achievable by monochromatic x-rays is in range of 0.11%.

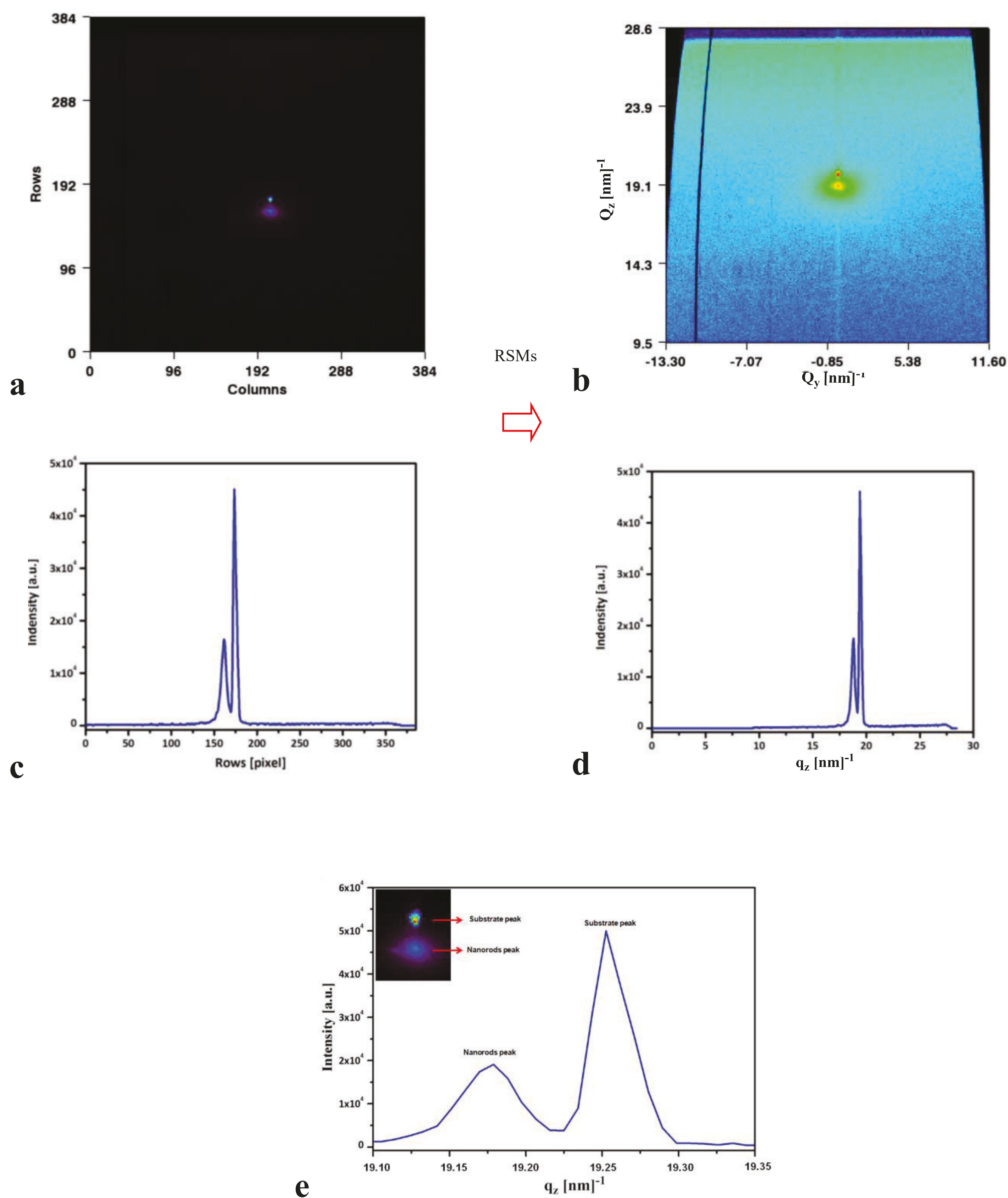

Figure 5.4 a) Integrated intensity image of GaAs NWs taken at the GaAs(111) reflection; b) RSM image of GaAs NWs taken at the GaAs(111) reflection; c) the vertical line profile of the integrated image; d) and e) the vertical line profile of the RSM image.

5.6. Conclusion

For the first time , in nanoscience field X-ray diffraction curried out using micro beam to study structures GaAs NWs Grown onto GaAs[111]B. The experimental results of the lattice parameter are in good agreement with that of theoretical value. Because the NWs crystallize in the wurtzite phase the lattice mismatch is $\Delta a/a = (a_{NWs} - a_{sub}) / a_{sub}$ with respect to the zinc-blende GaAs substrate is 0.34%. The lattice mismatch of the sample using monochromatic x-rays is 0.23% [134]. The agreements of the lattice mismatch between the accuracy which can be achieved by the white using PnCCD detector compared with the accuracy achievable by monochromatic x-rays is in range of 0.11%. In addition, one of the important advantages of using the pn CCD detector is that the measurement carried out in one shot without move or scans the sample.

The success of this experiment opened the door wide for further research with different samples of NWs using a micro white beam and pnCCD detector for detection in following experiments.

Chapter 6

6. EDR Experiment at BESSY (sectionII)

The Utilization of Energy-Dispersive Laue Diffraction to Determine Lattice Mismatch and Strain of InAs Nanowires on GaAs (111) Substrate

Summary

We carried out a high-resolution X-ray diffraction pattern of periodic InAs nanowires grown onto GaAs[111]B surface. The experiment carried out at the EDR beam line of BESSY synchrotron using experimental conditions and the desired continuous X-ray spectrum with sufficient primary photon flux in the hard X-ray regime to create detectable diffraction signals from the NWs. Energy-dispersive X-ray diffraction techniques rely on a high usable photon flux in a wide energy range (5< E< 35 KeV) so that as many Bragg peaks as possible can be detected in a single X-ray shot without any sample rotation. In addition, the usage of high-energy X-ray diffraction enables to measure a large section of reciprocal space allowing to probe a real structure of the NWs and –insensitive reflections simultaneously.

6.1. Introduction

Semiconductor NWs can be grown by means of different approaches, e.g. in metal-organic vapor phase epitaxy (MOVPE), offering the possibility to control their position using growth on a pre-structured mask. Although this approach is highly successful for many material systems, a common problem during growth is the occurrence of structural defects within the wires. In the case of III-V semiconductor NWs, the Au particle can be replaced by droplets formed directly by the group III metal. The first step, liquid Au droplets are deposited on a bare substrate surface (GaAs), usually by annealing of an initially deposited Au film.

If the growing species, e.g. In and As, are supplied from the vapor phase, they can be collected in the Au droplet, until the supersaturation of the droplet leads to the crystallization of a nanowire at the liquid-solid interface (Figure 6.1, Figure 6.2). They commonly grow along the [111] direction of the cubic zinc-blende (ZB) structure, however, within the NWs usually stacking faults, rotational twins or even the hexagonal wurtzite (WZ) structure mix randomly. The analysis of lattice mismatch and defect structure of the NWs are crucial. Therefore we aim to determine lattice mismatch and strain of such semiconductor InAs NWs grown on GaAs[111] substrate with emphasis on the use of micro-focused x-ray beams using pnCCD detector at the EDR beam line of BESSY.

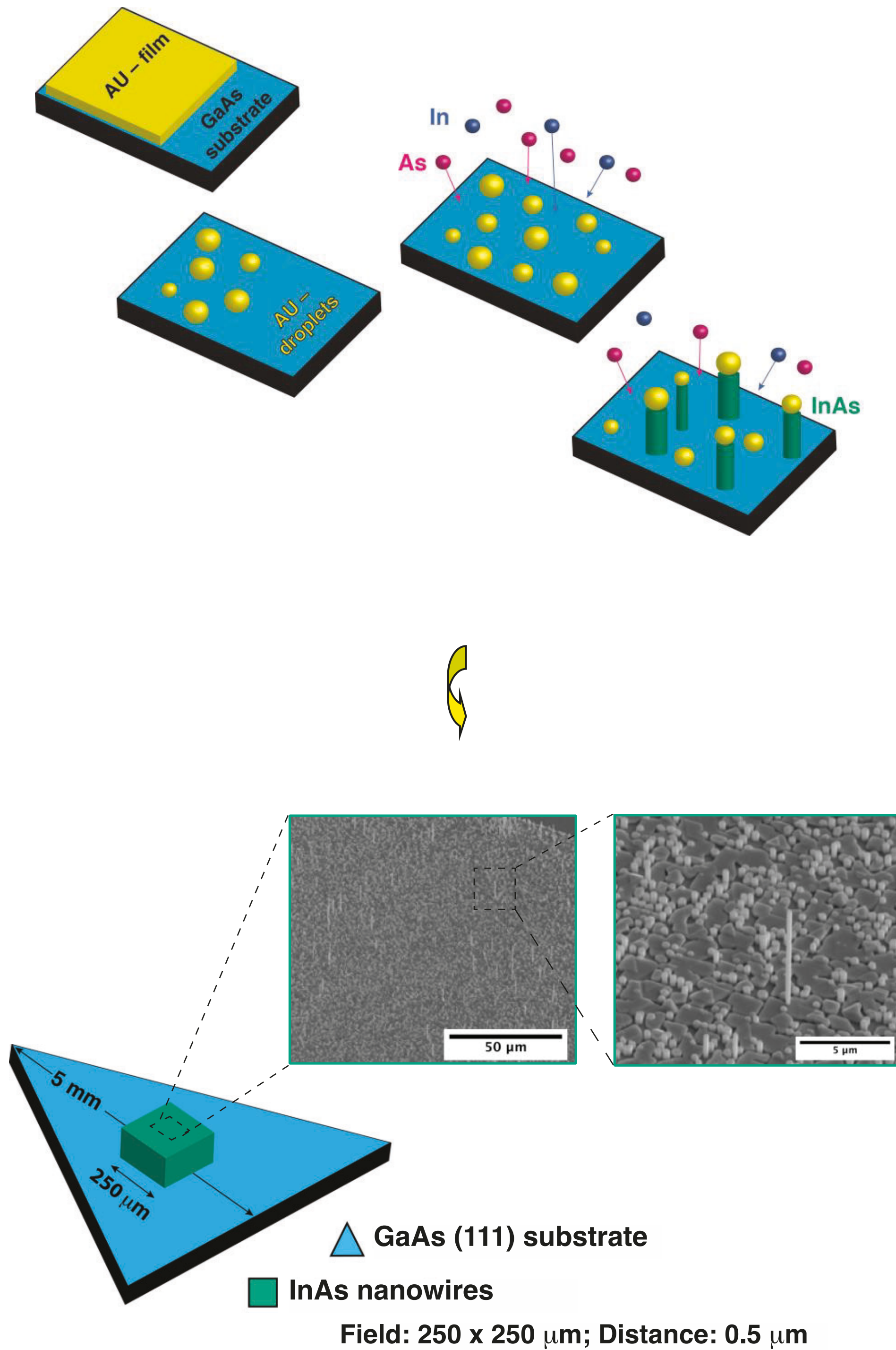

Figure 6.1 Schematic representation of the Au-assisted vapor-liquid-solid growth and SEM images of InAs nanowires grown on GaAs[111] substrate.

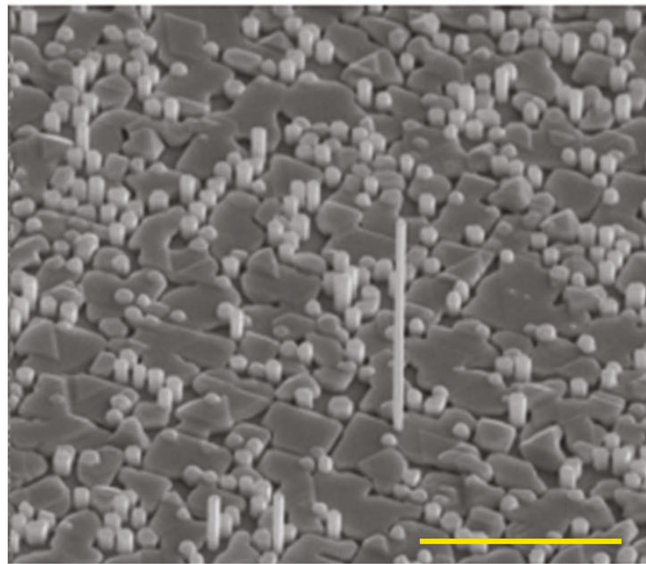

Figure 6. 2 SEM picture of InAs nm grown on GaAs[111]B substrate.The scale bars is 5 μm[136, 137 , 138].

The pnCCD as an energy-dispersive CCD detector allows a simultaneous measurement of the Laue spots positions and energies. This detector is divided in two parts namely an image area (384×384 pixels with 75×75 μm^2 pixel size) and frame store area (384×384 pixels with 75×51 μm^2 pixel size). After the x-rays hits InAs NWs grown on GaAs[111] substrate. The photons enter the detector volume, they interact with the silicon substrate and create photo-electrons which drift to the front pixilated plan of the detector and stored under the pixel registers. Buckets of stored electrons are shifted in parallel to the read out anode with a 3 phase transfer clock. Further amplification and shaping (8 MCDS) of the signal done and the pixel amplitudes are digitized and sent the data acquisition system for offline analysis as explained in detail in the second chapter in the thesis.

6.2. Synchrotron radiation source (EDR bemline-BESSY II)

Synchrotron radiation has become a premier research tool for the study of matter in all its varied manifestations, as facilities around the world constantly evolved to provide this light in ever more useful forms. Synchrotron radiation occurs

when relativistic electrons are deflected due to bending magnets which form the circular bath.

Electrons race through the storage ring in stabile trajectory for several hours. Then, radiation leaves the ring tangentially through the outlets (front ends) into the beamlines. In the beamlines, the radiation is dispersed by optical gratings, focused and guided by mirrors to the experimental end stations.

In order to produce more light periodic arrays of magnets, special magnetic insertion devices can be used namely undulators and wigglers. One of the most modern synchrotron radiation sources in the worldwide, which offer extended research opportunities for its users, is the synchrotron radiation source BESSY II in Berlin-Adlershof.

BESSY II provides highly brilliant synchrotron radiation from the infrared to the hard X-ray spectral region for various applications in physics, chemistry, medicine, material sciences, nanotechnology, and life sciences. The following table 6.1 shows the synchrotron parameters, while figure 6.3 shows the synchrotron power spectrum at BESSY II which is presented in linear and logarithmic scales.

Table 6.1 BESSY II synchrotron radiation parameters [139].

Electron energy	1.7 GeV.
Circumference of the storage ring	240 m.
Emittance (horizontal)	6.10^{-9} m rad.
Straight sections	16
Beamlines with dipoles	max. 40
Beamlines with insertion devices	max. 30
Brilliance.	Ca. 10^{19} $\frac{\text{Photons}}{\text{Sec mm}^2\ \text{mrad}^2\ 0.1\%\ \text{BW}}$ where BW is the spectral band width.

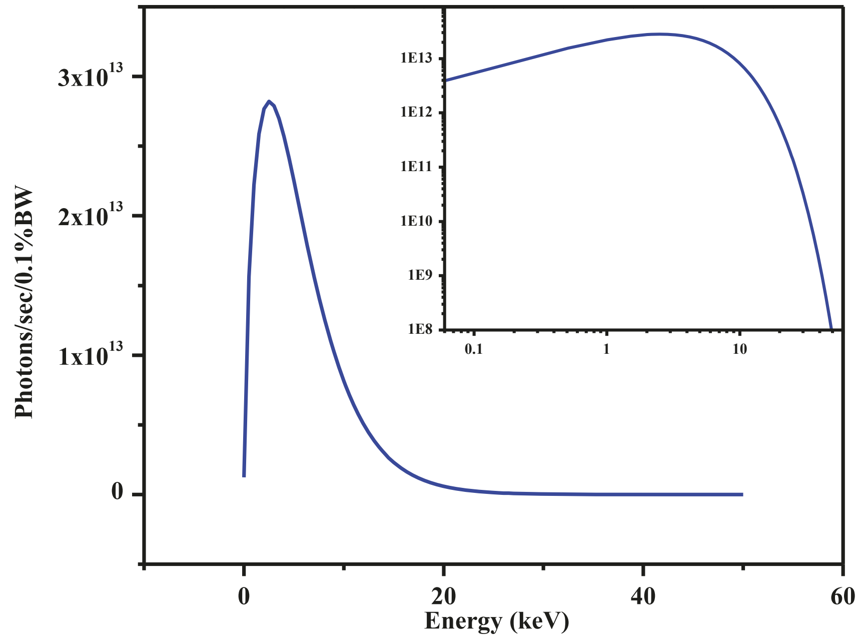

Figure 6.3 The spectrum power of synchrotron radiation at BESSY II calculated for a ring current of 200 mA. Electrons with energy of 1.72 GeV are deflected in a magnetic field of 1.3 T [140].

6.3. Setup of the Experiment

The measurement was implement at the EDR beam line of BESSY synchrotron using InAs NWs grown on GaAs[111] substrate. The experimental setup is shown in Figure 6.4 The sample was illuminated micro white beam at incident angle α_i = 3.0°, the size of the X-ray beam was focused to the size of (H x V) 50 x 20µm^2. The sample to detector distance was 35 mm. the detector moved up a distance Z = 30 mm to detect the diffraction signals as shown in figure 6.4 The 500K frames data sets were recorded at 100Hz in the signal photon counting mode to preserve the energy information. The NWs (InAs) and the substrate (GaAs) together were measured by the pnCCD detector and then the substrate (GaAs) alone was re-measured at the same position of the pnCCD detector.

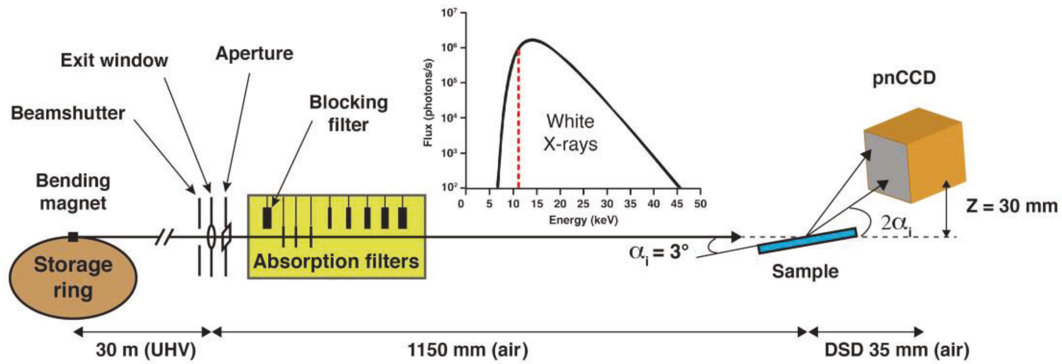

Figure 6.4 Set-up of experiment at the EDR bemline (BESSY II).

6.4. Discussion and results

The result of the offline analysis produces a 3D array [y_p, z_p, E] with coordinates of position and energy for every photon impact. The reflected signal of the sample in a particular direction defined by Bragg's law consists of diffracted energies E_1,...,E_n with average count rates 1,...,n superimposed by the background count rate. In this case, the detectable energies E_1,.., E_n which belong to reflections of various orders, are integer multiples of the energy assigned to the first-order Bragg peak with coprime miller indices hkl as explianed in chapter 4. Laue spots are located in the detector at position (y,z). The Bragg angles have been calculated with respect to the primary beam position as well as the energy of the Laue spot can be determined at the same time. The coordinate system was defined in such a way that the positive x axis corresponds to the incident beam direction. In the following, the data taken for a selected Laue spot of energy E_{hkl} will be discussed in more detail in 3D array [yp, zp, E] as shown in figure 6.5 where Laue pattern of InAs NWs grown onto GaAs[111] substrate recorded by the pnCCD in reflection geometry at the EDR beamline of BESSY II in Berlin (figure 6.5-b) and Laue pattern of on GaAs substrate recorded in the same reflection geometry (figure 6.5 -c). The continuous background contributions in the vicinity of the spot E_{hkl} region, caused by air-scattered photons and fluorescence radiation from the sample (Ga-kα1= 9.251 keV, As-kα1= 10.543 keV) as shown in figure 6. 6.

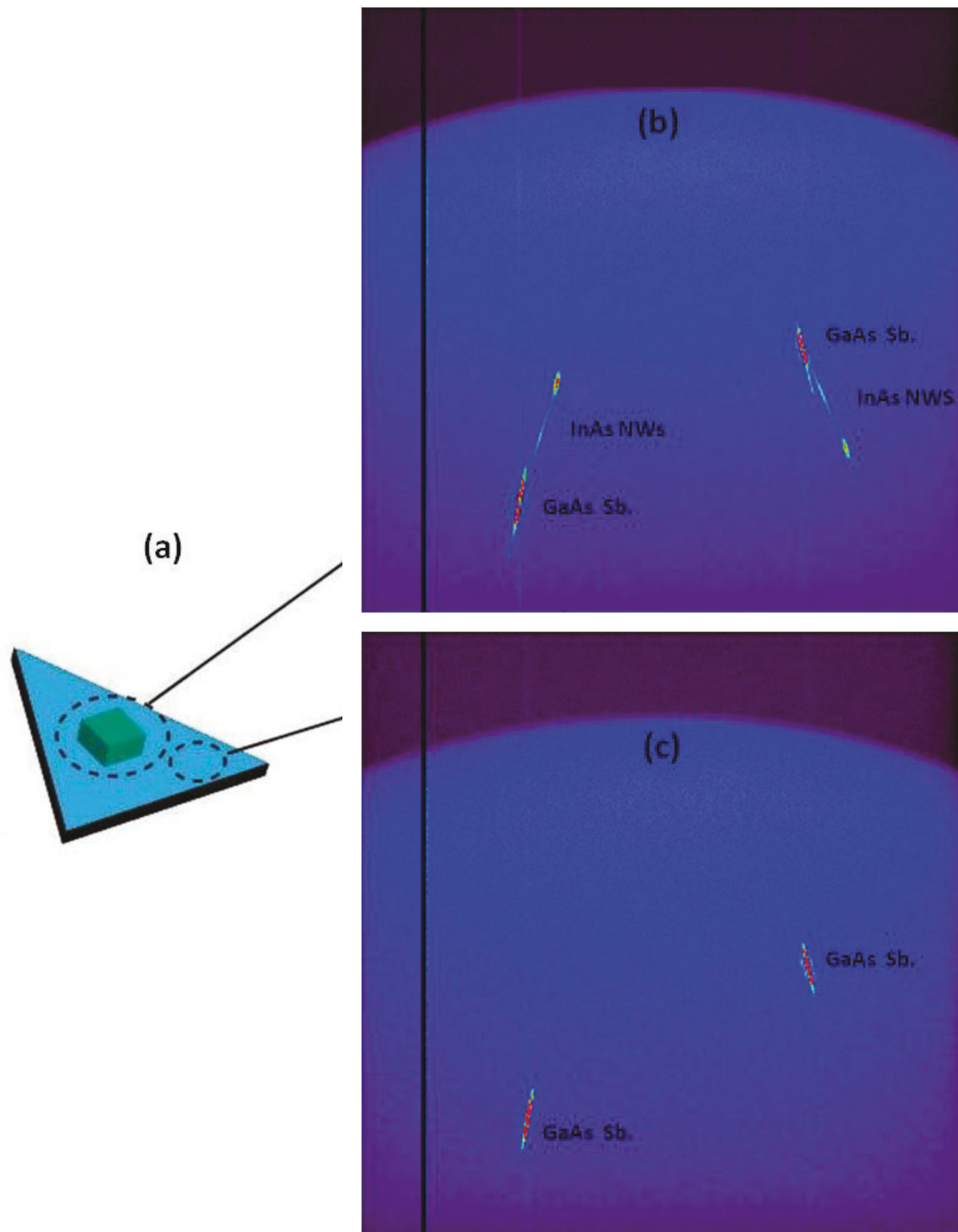

Figure 6.5 (a) The geometry of the sample and one circle shows where the photons hit the sample were the InAs NWs and GaAs substrate together while the second circle the photons only hit the sample were GaAs substrate and in both pevious case the size of the X-ray beam was focused to the size of (H x V) 50 x 20 μm^2, (b) Laue pattern of InAs NWs grown onto GaAs[111] substrate recorded by the pnCCD in reflection geometry at the EDR beamline of BESSY II in

Berlin, (c) Laue pattern of on GaAs substrate recorded by the pnCCD in the same reflection geometry.

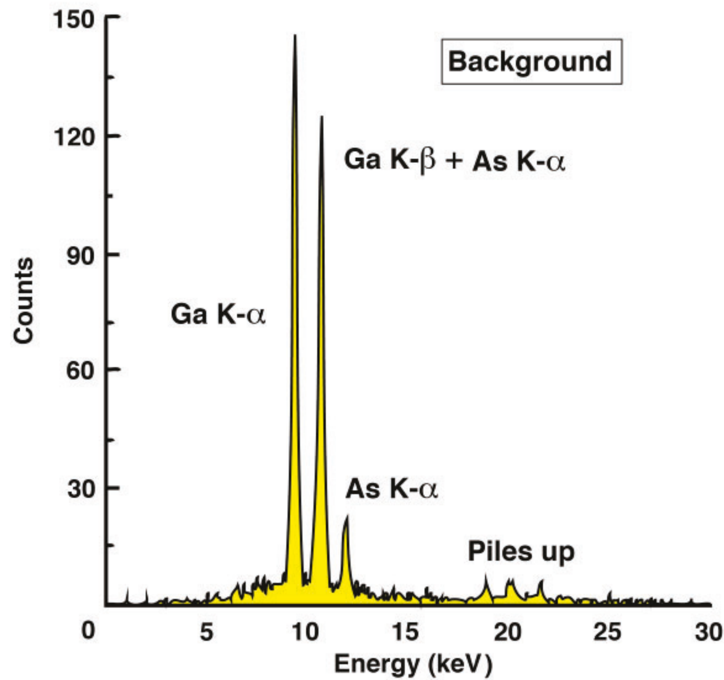

Figure 6.6 Energy spectrum of the Background detected by the pnCCD in an X-ray fluorescence experiment using InAs NWs grown on GaAs[111] substrate.

The energy values of Laue spot E_{hkl} in the intensity image Figure 6.7-a and Figure 6.8-a are determined as shown in (Figure 6.7-b,d,c) and (Figure 6.8-b,d,c). In Figure 6.7-b, the applied Gaussian fit of a pixel area of spots provides the spot the sample where the size of the X-ray beam was focused to the size of (H x V) 50 x 20 µm2. energy $E \pm \Delta E = 14.856 \pm 0.306$ keV, where $\Delta E = FWHM/2.355$ is the standard deviation. In this case the relative energy resolution is $\Delta E/E = 1$ %. Beside the Laue spot energy there are additional features in the detected spectrum, such as continuous background contributions in the vicinity of the spot E_{hkl} region, caused by air-scattered photons and fluorescence radiation from the sample as shown (Figure 4-d). It should be noted that the measured energy are subtracted from background energy in figure 6.7-b, c and figure 6.8-b, c. It

should be noted that the reason of the shape of the Laue peaks in figure 6.5 due to the geometry of

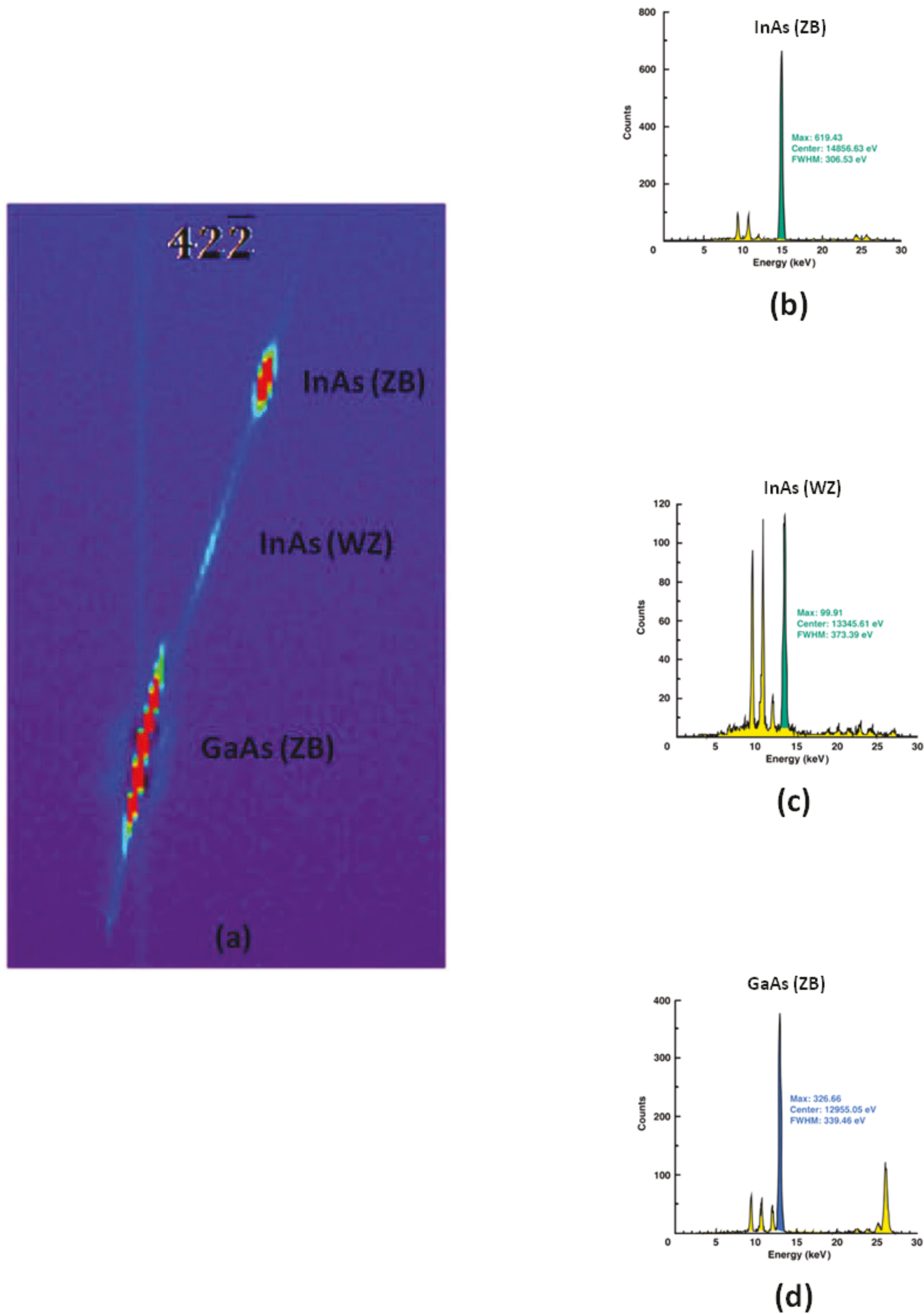

Figure 6.7 $42\bar{2}$ Laue spot of InAs NWs grown on GaAs [111] substrate (a). The spot shows three maxima in angular space and three different spot energies (b, c, d).

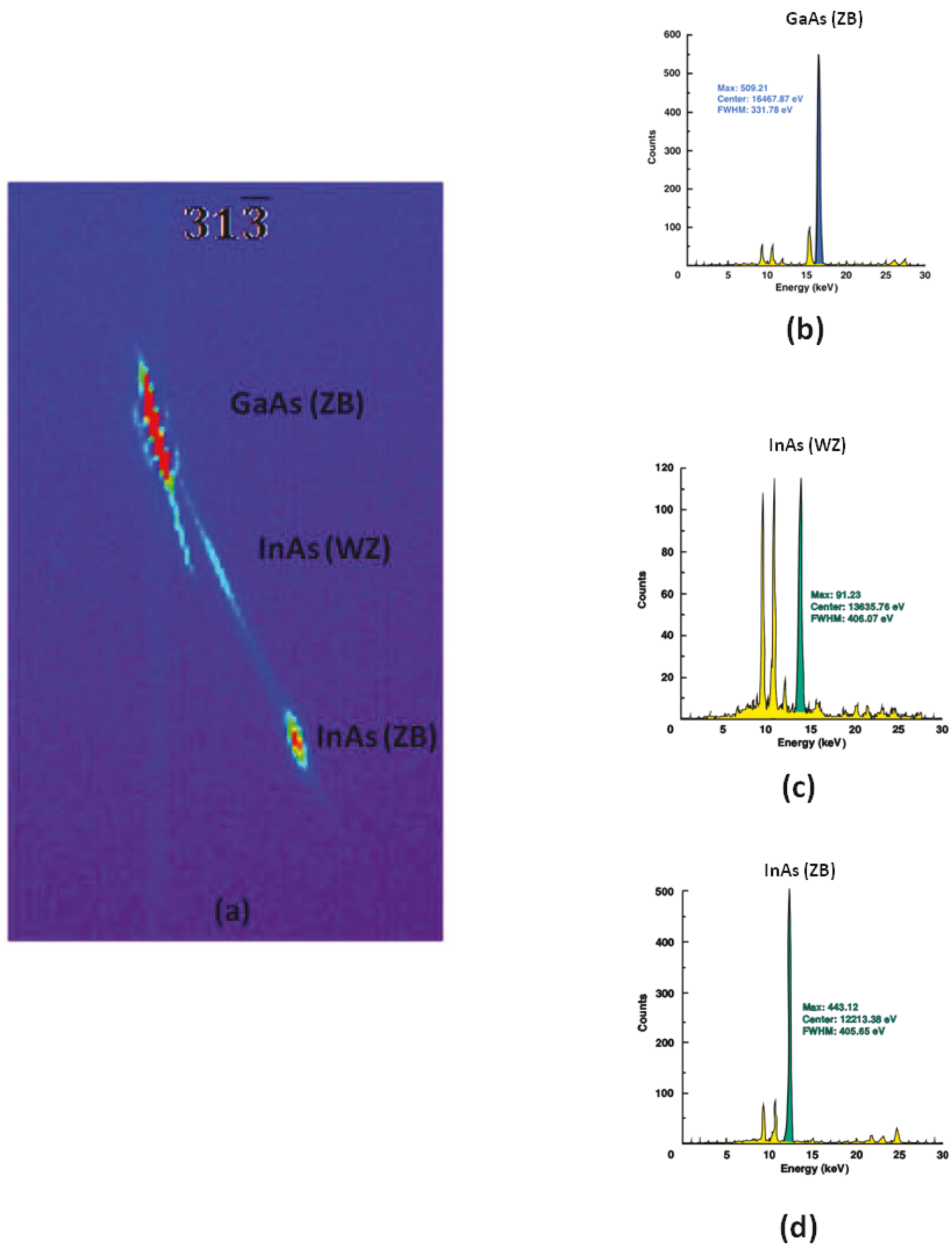

Figure 6.8 $31\bar{3}$ Laue spot of InAs NWs grown on GaAs[111] substrate (a). The spot shows three maxima in angular space and three different spot energies (b, c, d).

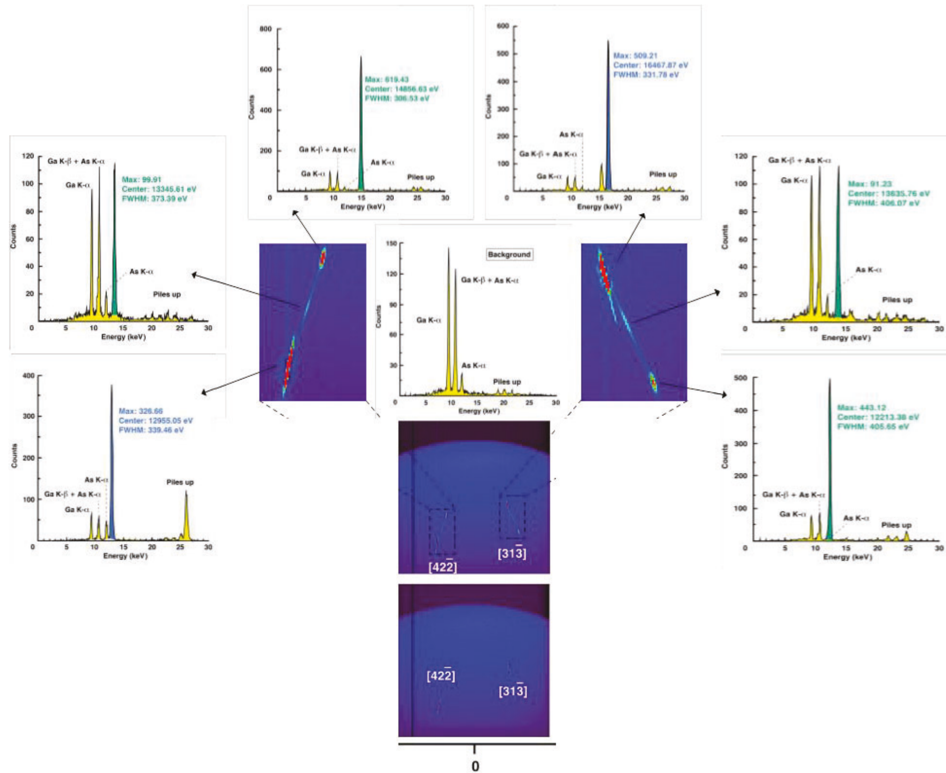

Figure 6.9 the total Integrated intensity image of GaAs[111] substrate (below) and Integrated intensity image of InAs NWs grown on GaAs[111] substrate (up) and evaluated energy and Miller indices for all reflected spots.

Considering cubic symmetry and knowing the energy, Bragg angle and Miller indices of each reflection in figure 6.9, all reflected spots can be indexed using the below relations in 4.19, 4.24 in the chapter 4

$$H^2 + K^2 + L^2 = a^2/d^2, \text{ using } d = hc/(2E \sin\theta) \quad (6.1)$$

Where "a" is the lattice parameter of the cubic lattice, h is Planck constant and c is the speed of the light. Signs of H, K and L are determined considering the angular relations between (H,K,L) and (111) on one hand and between the different (H,K,L) of one reflection {HKL} on the other hand using the below following relation

$$\cos\varphi = \frac{H_1H_2+K_1K_2+L_1L_2}{\sqrt{H_1^2+K_1^2+L_1^2}.\sqrt{H_2^2+K_2^2+L_2^2}} \tag{6.2}$$

This results in the indexation shown in figure 6.9.

The total integrated intensity image of InAs NWs grown on GaAs [111] substrate and evaluated all energy and Miller indices for all reflected spots as shown in figure 6.9. Since NWs grow either along [111] of cubic or along [0001] of the hexagonal lattice the respective d-values were probed by using the below relations 4.19, 4.21 in the chapter 4 and the d value of results Considering cubic symmetry for GaAs (ZB) and InAs (ZB) will present in the table 6.2, 6.3, 6.4.

$$d_{hkl}^{c} = \frac{a}{\sqrt{H^2+K^2+L^2}}\ ,\ d_{hkl}^{h} = \frac{a}{\sqrt{\frac{4}{3}(h^2+hk+k^2)+(\frac{a}{c})^2\ l^2}} \tag{6.3}$$

In order to caululted lattice parameter of InAs (WZ), The hexagonal Miller-indices of $(hkil)^h$ can be calculated form the cubic Miller-indices of $(HKL)^c$ by the following transformation matrix relation 4.22 in the chapter 4.

$$\begin{pmatrix} h \\ k \\ l \end{pmatrix}_h = \begin{pmatrix} 1/2 & 0 & -1/2 \\ -1/2 & 1/2 & 0 \\ 1 & 1 & 1 \end{pmatrix} \begin{pmatrix} H \\ K \\ L \end{pmatrix}_c \tag{6.4}$$

Resulting in h = (H-L)/2; k = (K-H)/2; i = (L-K)/2; l = H+K+L.

Depending on equation (6.4) it transforms $(31\,\overline{3})^c$ to $(3\,\overline{1}\,\overline{2}\,1)^h$, Due to similarity of ZB- and W- InAs structure indexing has been done in both ZB (hkl) and/or W (hkil) notation. We calculated the $d_{hkl}^{c} = d_{hkl}^{h}$value in relation 4.2 in the chapter 4.

In this case the [111] axis of cubic unit cell becomes the c-axis of hexagoal lattice for InAs and using a_{cub} = 6.0584 Å the a and c lattice parameters of hexagoal lattice become a_{hex}= 4.243 Å; c_{hex} = 7.025 Å following in a a/c ratio of $(a_{hex}/c_{hex})^2$=0.1656 [136]. Considering the hexagonal coordinate system, the d(khil)-values follow the relation shown in relations 4.19, 4.21 in the chapter 4.

Tables 6.2 show the evaluating experimental data for spot $42\bar{2}$

$42\bar{2}$ Laue spot	E(KeV)	FWHM (eV)	θ_B°	d (1/Å)	HKL	a (Å) Cal.	a (A°) The.	ε
GaAs (Sub.)_ZB	12.955	339.46	24.926±0.981	1.2361	$42\bar{2}$	5.6522±0.01	5.6532	7.142%
InAs (NWs)_WZ	13.205	373.39	224.159±2.121	1.1350	$31\bar{2}4$	4.5491±0.31	4.243	7.211%
InAs (NWs)_ ZB	14.856	306.53	19.728±0.971	1.2361	$42\bar{2}$	6.0559±0.01	6.0584	7.142%

Tables 6.3 show the evaluating experimental data for spot $31\bar{3}$

$31\bar{3}$ Laue spot	E(KeV)	FWHM (eV)	θ_B°	d (1/Å)	HKL	a (Å) Cal.	a (A°) The.	ε
GaAs (Sub.)_ZB	16.467	331.78	16.877±0.981	1.2966	$31\bar{3}$	5.6521±0.01	5.6532	7.241%
InAs (NWs)_WZ	13.653	406.07	21.031±2.111	1.263	$31\bar{2}1$	3.925±0..31	4.243	7.464%
InAs (NWs)_ ZB	12.213	405.85	21.4088±0.991	1.3905	$31\bar{3}$	6.0614±0.01	6.0584	7.241%

Table 6.4 experimental value of Lattice mismatch is compatible with the theoretical value.

HKL	Lattice mismatch_cal.	Lattice mismatch_the.
$31\bar{3}$	(7.1±0.1) %	(7.1±0.1)%
$42\bar{2}$	(7.2±0.2) %	

The experimental results are in good agreement with that of theoretical value in range of 1%. The lattice mismatch of the sample $\Delta a/a = (a_{rods} - a_{sub}) / a_{sub}$ is 7.241% due to the different lattice parameters of NW and substrate. But the lattice mismatch of the sample using monochromatic x-rays is 7.161% [136, 137, 138]. The agreements of the lattice mismatch between the accuracy which can be achieved by the white beam Laue method compared with the accuracy achievable by monochromatic x-rays is in range of 0.2%.

6.5. Conclusion

In this study, the response of pnCCD for hard X-ray exposure is tested at EDR beamline of BESSY II synchrotron for nanomaterials by analysis of InAs NWs planted on GaAs (111) substrate. The experimental and theoretical values of lattice parameters for GaAs substrate and InAs NRs are in good agreement are in range of 0.1%. The agreements of the lattice mismatch between the accuracy which can be achieved by the white beam Laue method compared with the accuracy achievable by monochromatic x-rays is in range of 0.2%.Using high and wide range of energy gives advantages of having more Laue patterns resolved in a large reciprocal space volume. The experiment clearly demonstrated the potential of pnCCD detectors for applications in semiconductor nanomaterials science using total hard X-ray Spectrum.

Chapter 7

7. EDDI Experiment

Application of polychromatic hard X-ray for energy-dispersive Laue diffraction to analyse GaAs/In_xGa_{1-x}As/GaAs core-shell nanowires using pnCCD detector

Summary

A frame-store pn-junction CCD is applied as a detection tool during energy-dispersive Laue diffraction, for the first time, on semiconductor nanowires (NWs) using white synchrotron radiation in the energy range of 20 to 120 keV. We investigate GaAs/In_xGa_{1-x} As/GaAs core-shell NWs grown by molecular beam epitaxy (MBE) onto a Si (111) substrate. Here the incident x-ray beam illuminates the sample nearly parallel to the [111] direction providing various Laue spots of few highly indexed {hkl} families which fulfill the Bragg condition with different lattice planes within the NWs for the wide range of x-ray energies. Operating the pnCCD in the energy selective mode, both the Bragg angles and the Bragg energies of all Laue spots can be measured simultaneously allowing for the determination of the lattice parameters for core and shell material separately. After the evaluation of 23 Laue spots and correction the small misalignment of the reflected beam by angle alpha =1.261 degree with respect to the 111 growth axis the In content of the In_xGa_{1-x} As shell pseudomorphically grown onto the GaAs core has been determined to $x = 26.5 \pm 1.5$ percent.

7.1. Introduction

$A^{III}B^{V}$ nanowires (NWs) grown onto Si (111) substrates are promising materials for future integration of optoelectronic applications in the Si technology [141 ,142]. Grown by molecular beam epitaxy (MBE) or metal-organic vapor phase

epitaxy, NWs can be grown as perfect crystalline material [143, 144,145]. In particular the core-shell composition of semiconductor NWs allows for various applications in the field of optoelectronics and energy harvesting [146]. Here, after the growth of a NW core, a material with a different lattice parameter is grown onto its side facets. For a nominal In content of 25% within the (In,Ga)As shell, the strain accommodation within the core-shell NW system is in the elastic regime [147]. Therefore, both materials grow pseudomorphic along the growth direction, faced by major deformation along the radial direction. In addition, due to growth along the zinc-blende (ZB) [111] direction, major structural defects such as the inclusion of stacking faults, and the appearance of different structural phase, such as the wurtzite (ZW) or 4H polytypes along the growth axis may deteriorate the performance of the respective devices requiring careful structural analysis of the NWs. Typically, the crystal phase structure and strain in NWs are investigated by high-resolution transmission electron microscopy (HRTEM) [148, 149, 150] and monochromatic x-ray diffraction (XRD) techniques [151]. Recently we have demonstrated that the complete structure of core-shell NWs can be determined using x-ray nano-diffraction measuring Bragg diffraction along and perpendicular to the NW growth axis [152]. Nevertheless, these measurements are time consuming and require additional modeling in terms of the finite element method. On the other hand, HRTEM analysis can only be applied locally as the prepared lamella needs to be less than a hundred nanometers thick. Moreover, the milling process is usually done using a focused ion beam which may induce detrimental changes to the crystal lattice. Therefore an alternative and less complicated method that can be used for strain characterization in NWs is demanded. In this paper, we demonstrate that the use of highly brilliant synchrotron radiation in combination with the energy dispersive pnCCD detector opens a new route of fast and precise structural analysis of core-shell NWs in their as-grown geometry. In this paper, we study the structure and strain of the $In_xGa_{1-x}As$ shell in $GaAs/In_xGa_{1-x}As/GaAs$ core-shell NWs using the pnCCD detector and a white beam. The experiment has been performed at the EDDI beam line of the BESSY II. The determination of the In

content within the (In,Ga)As shell of GaAs/In_xGa_{1-x}As/GaAs core-shell NWs using a combination of monochromatic high-resolution XRD and nano x-ray fluorescence has been reported by our group, Siegen university [152]. In this work we used the same NW system, radially composed of GaAs/In_xGa_{1-x} As/GaAs, at hard x-ray beam lines of BESSY II to study and determine the hexagonal deformation of the In_xGa_{1-x}As lattice along the growth direction of the NWs. We demonstrate that a Laue diffraction experiment allows for a fast access to the structural parameters of core-shell NWs which is promising for future use in NW device technology.

a. . pnCCD detector

Using white synchrotron radiation, the pnCCD provides a three-dimensional intensity distribution spanned by two pixel coordinates and an energy direction covering a 3D data volume in reciprocal space. The used pnCCD detector is a pn-junction charge coupled devices. The detection area is composed of 384 x 384 pixels in which each pixel is 75 x 75 μm^2 in size serving as individual energy selective point detectors with an energy resolution ΔE/E of about 1%. Currently, the frame store pnc-CD module at the University of Siegen is based on the eROSITA generation and has a sensitive area of 28.8 x 28.8 mm^2. Sensitive n-doped Si thickness is 450 µm subdivided into two parts namely an image area of 384×384 pixels with 75×75 μm^2 pixel size and frame store area of 384×384 pixels with 75×51 μm^2 pixel size with a typical readout frequency of about 100 Hz. The pnCCD provides a quantum efficiency higher than 95% in the range from 3 to 10 keV, above 30% at 20 keV, 7% at 40 keV, 3.5% at 60 keV and below 2% above at 100 keV [153, 154]. X-ray charge signals generated in the image area were accumulated for an externally selected integration time and are quickly transferred to the frame store area within 230 µs (600 ns per row). After amplification on the chip at low noise level, parallel readout of the column of the transferred image is achieved within 11.5 ms (30 per row) by three CAMEX chips with 128 channels each [155, 156, 157]. After the x-ray enters the detector

volume, they interact with the Si substrate and create a cloud of photoelectrons drifting to towards the front pixilated of the detector and are stored under the pixel registers. Buckets of stored electrons are shifted in parallel to the readout anode with a three-phase transfer clock. Further amplification and shaping (8MCDS) of the signal is done and the pixel amplitudes are digitized and sent to the data acquisition system for offline analysis.

7.3. Energy-dispersive Laue diffraction

A favored application of pnCCD is the energy dispersive Laue diffraction. It has been applied for structure analyses of single crystals [153]. and polycrystals [158] within an energy range of 20 keV to 120 keV, so that as many Laue spots as possible can be detected within a single x-ray shot at an incident angle α=90° with respect to the substrate surface. Taking into consideration, the distance between the sample and the detector allows the access of high indexed d-values.

7.3.1. Sample

Structural information about the investigated NWs are listed in Table 7.1 and the NW cross-section is animated in figure 7.1a. The number density of NWs was extracted by scanning electron microscopy (SEM). An example is illustrated in figure 7.1b and a zoom in on an individual NW is displayed in figure 7.1c. The core-shell configuration such as the nominal dimensions and nominal In content of the $In_xGa_{1-x}As$ shell were deduced from MBE growth parameters. The fractional In concentration, x, thickness, t, and the out-of-plane as well as in-plane elastic strain values of the In_xGa_{1-x} As shell were determined from high-resolution XRD measured along the [111] and [$2\bar{2}0$] direction as described by [152]. The selected NW sample under investigation is composed of a 150 nm thick GaAs core, covered by 40 nm $In_xGa_{1-x}As$ shell with 25% In and protected by 30 GaAs outer shell as animated in figure 7.1a. The aim of this experiment is

to deduce the composition of the $In_xGa_{1-x}As$ shell by white beam Laue diffraction using single shot exposure.

Table 7.1 structural information of the NWs ($GaAs/In_xGa_{1-x}As/GaAs$) under investigation. The $In_xGa_{1-x}As$ lattice is compressively strained along [111] faced by tensile strain along $[2\bar{2}0]$. Strain along [111] and $[2\bar{2}0]$ is denoted by $\varepsilon_{zz}^{(In,Ga)As}$ and $\varepsilon_{xx}^{(In,Ga)As}$, respectively.

NW density (μm^{-2})	**1**
Core-shell configuration	$GaAs/In_xGa_{1-x}As/GaAs$
Nominal dimensions (nm)	140/40/30
Nominal [In] (%)	25
XRD [In] (%)	27 ± 1.5
XRD [t] (nm)	36 ± 3
$\varepsilon_{zz}^{(In,Ga)As}$ **(%)**	−1.11
$\varepsilon_{xx}^{(In,Ga)As}$ **(%)**	**1.59**

However, in the mentioned XRD experiment, the complete strain state of the shell could be determined only by subsequently measuring the NW in two different diffraction geometries which consequently is a time consuming process.

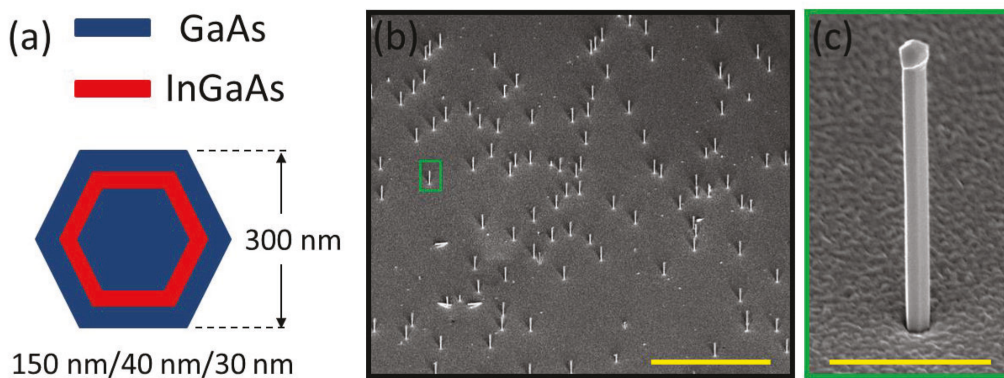

Figure 7.1 Panel (a) an animation showing the cross-section of a $GaAs/In_xGa_{1-x}As/GaAs$ core-shell NW. (b) SEM micrograph of an area on the substrate full of NWs. (c) a zoom in on an individual NW marked by a green box in (b). The scale bars in (b) and (c) are 30 µm and 2 µm, respectively.

7.3.2 Setup of experiment

We present a complementary approach to the high resolution XRD experiment [152] in order to determine the In content and strain in the $In_xGa_{1-x}As$ shell of a $GaAs/In_xGa_{1-x}As/GaAs$ core-shell NW using white synchrotron radiation and an energy-dispersive pnCCD detector. The experiment has been carried out at the EDDI beam line of BESSY II storage ring using nearly continuous hard x-rays creating detectable diffraction signals from the NWs. The 50 x 50 μm^2 white beam was directed slightly oblique to the [111] growth axis generating several Bragg peaks forming in a rather circular arrangement around the transmitting beam. The energy spectrum used ranged from 5 keV to 120 keV making it possible to measure up to $(h^2 + k^2 + l^2) < 107$. The pnCCD raw data consisted of 300 dark frames recorded in the absence of x-rays and 100 k signal frames taken from the sample exposed to white synchrotron radiation at a particular position on the sample and at fixed detector position (X_{Pixel} = 217, Y_{pixel} =150). The sample to detector distance was D = 55.8 mm providing an opening angle less than 24 degree as shown in figure 7.2.

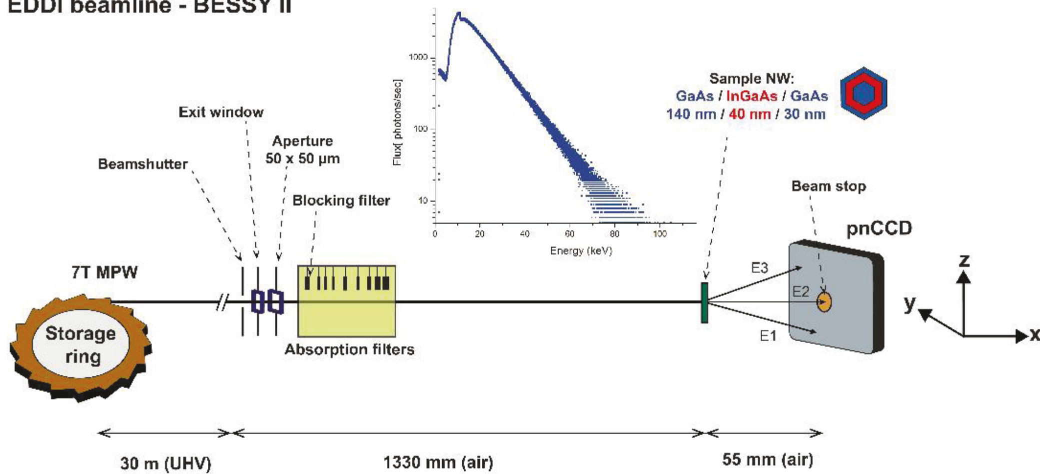

Figure 7.2 Experimental setup for energy-dispersive Laue diffraction on the $GaAs/In_xGa_{1-x}As/GaAs$ core-shell-shell NWs using white synchrotron radiation in the ultra-hard energy range at the EDDI beamline of BESSY II.

7.4. Data analysis and results

figure 7.3 shows the Laue pattern of the sample containing about 25 Laue spots. Each of the spots is analyzed in terms of peak position (Bragg angle θ) and peak energy (E). The result of the offline analysis produces a 3D array [y_p, z_p, E] with coordinates of position and energy for each single photon impact. After the integration of all single frames, the reflected signal of the sample along a particular direction defined by Bragg's law consists of diffracted energies E_1,..., E_n with average count rates 1,...,n superimposed by the background count rate. In this case, the detectable energies E_1... E_n which belong to reflections of various orders are integer multiples of the energy assigned to the first-order Bragg peak with coprime Miller indices (hkl). Considering cubic symmetry and knowing the energy, Bragg angle and Miller indices of each reflection, all reflected spots can be indexed using the below relations in 4.19, 4.24 in the chapter 4

$$H^2 + K^2 + L^2 = a^2/d^2 \text{ , using } d= hc/(2E \sin \theta) \qquad (7.1)$$

Where "a" is the lattice parameter of the cubic lattice, h is Planck constant and c is the speed of the light. Signs of H, K and L are determined considering the angular relations between (H,K,L) and (111) on one hand and between the different (H,K,L) of one reflection family {HKL} on the other hand using the following relation

$$\cos \varphi = \frac{H_1 H_2 + K_1 K_2 + L_1 L_2}{\sqrt{H_1^2+K_1^2+L_1^2} . \sqrt{H_2^2+K_2^2+L_2^2}} \qquad (7.2)$$

This results in the indexation shown in figure 7.3. Since NWs grow either along [111] of cubic or along [0001] of the hexagonal lattice the respective d-values follow by using the below relations 4.19, 4.21 in the chapter 4.

$$d_{hkl}^{c} = \frac{a}{\sqrt{H^2+K^2+L^2}} \; ; \; d_{hkl}^{h} = \frac{a}{\sqrt{\frac{4}{3}(h^2+hk+k^2)+(\frac{a}{c})^2 \, l^2}} \qquad (7.3)$$

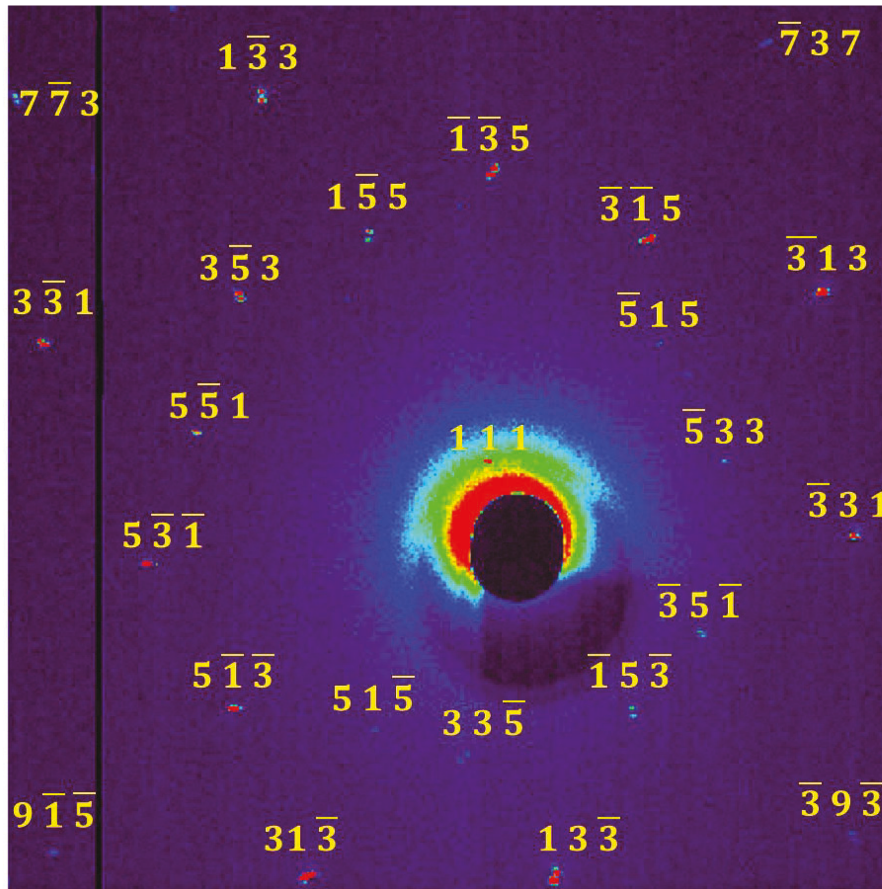

Figure 7.3 Laue diffraction pattern of a GaAs/$In_xGa_{1-x}As$/GaAs core-shell-shell NWs array accessed with an incident angle close to [111] growth axis. The bright spot in the middle is created by blocking the incident beam with a beam-stop. Since the pnCCD provides the diffraction energy and Bragg angles, each spot was indexed by (HKL). The 111 reflection spot is visible close to incident beam also but with low intensity due to the high background.

Figure 7.3 displays the $\{1\bar{3}3\}$, $\{\bar{1}\bar{3}5\}$, $\{5\bar{5}1\}$, $\{3\bar{5}3\}$and $\{7\bar{7}3\}$ reflection families of Bragg reflections in a deformed hexagonal arrangement. Due to small angle the small misalignment of the reflected beam with respect to [111], they are not symmetrically arranged with respect to the center of the detector frame. Closer look into each of the reflections displays a double peak structure visible by two spots of different Bragg angles as shown in figure 7.4a and different spot energy as shown in Fig. 7.4b-d. The evaluated spot spectra show a single peak from the region marked by the red box (figure 7.4b) and two peaks of different

energies at the region marked by the pink box (figure 7.4c). The sum of both energy spectra is displayed in figure 7.4d. The features can be explained by the particular structure of the core-shell NWs. As demonstrated by Lewis [147] core and shells grow with pseudomorph lattice parameter along the growth direction resulting in an axial compression of InGaAs shell and small axial expansion of GaAs core and outer shell. The accumulated stress is released along the direction perpendicular to the growth axis. This results in a hexagonal deformation of both components. Subsequently, for example, the angle between the $(\overline{13}5)$ (cubic notation) lattice plane to the (111) growth axis of the hexagonally deformed InGaAs lattice is by about 0.1 degree smaller compared to the angle between the $(\overline{13}5)$ lattice plane with respect to the growth axis in cubic crystal system. Since the hexagonal deformation of the GaAs core is very small, it is neglected in the upcoming data analysis, i.e. the GaAs lattice is kept in the cubic symmetry.

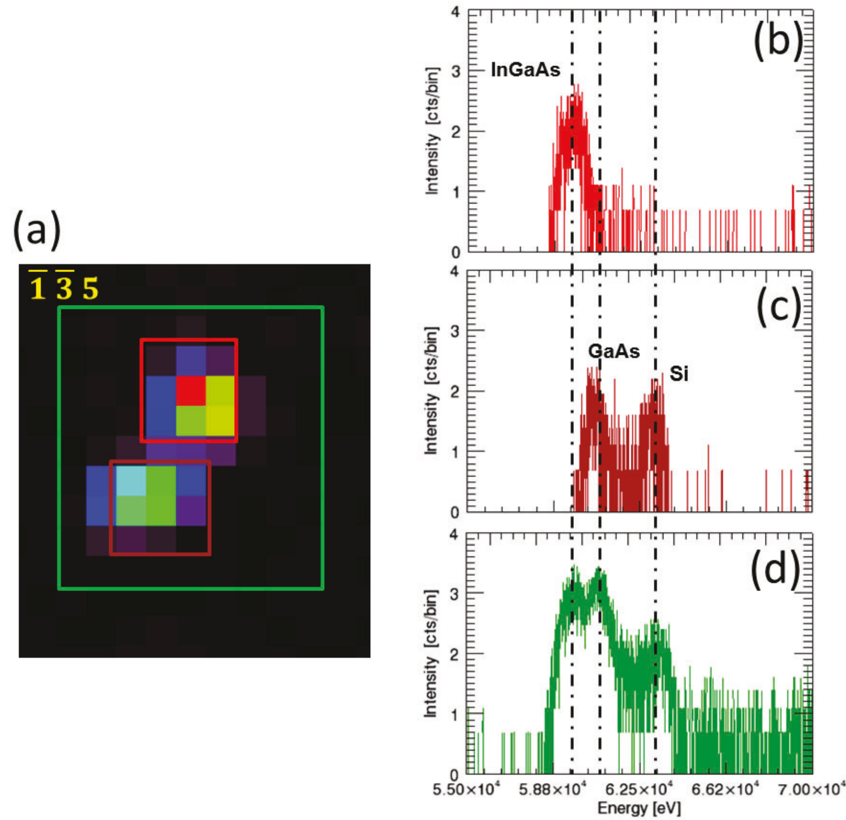

Figure 7.4 $\overline{13}5$ Laue spot of core-shell-shell NWs. The spot shows two maxima in angular space and two different spot energies.

Table 7.2 shows the experimental and theoretical values of the lattice plane $(\overline{13}5)$ estimated in cubic coordinates.

E(keV)	θ°	d[A°]Exp.	d[A°]th.	Identification
59.18	6.20	0.970	0.972	InGaAs shell
61.01	6.11	0.955	0.956	GaAs
63.51	6.11	0.917	0.918	Si

Due to the energy sensitivity of the detector, one can deduce the d-value of each reflection from the spot energy and Bragg angle (see equation 1). These values are listed in 3rd column of Table 7.2 of the $(\overline{13}5)$ reflection. The first row shows the measured d-value of the InGaAs shell whereas the 2nd and 3rd rows list those GaAs and Si, respectively. Data of all reflections of the $\{1\bar{3}3\}$ family are listed in

Table 7.3, the d-values shown in the 4rd and 5rd columns are the respective d-values calculated for cubic GaAs and Si using equation (3).

Table 7.3 shows List of theta angles and energies of all peaks of reflection family $\{1\bar{3}3\}$.

HKL ; hkil	E (keV)	Theta[deg]	d(exp.) [A˚]	d(th.) [A˚]
$31\bar{3}$; $3\bar{1}\bar{2}1$	38.99	6.95	1.314	1.320
	40.02	6.86	1.297	1.297
	41.66	6.86	1.245	1.246
$3\bar{3}1$; $1\bar{3}21$	31.68	8.55	1.316	1.320
	32.50	8.46	1.297	1.297
	33.87	8.48	1.244	1.246
$1\bar{3}3$; $\bar{1}\bar{2}31$	31.37	8.63	1.317	1.320
	32.26	8.52	1.297	1.297
	33.70	8.52	1.244	1.246
$\bar{3}13$; $\bar{3}211$	39.05	6.94	1.314	1.320
	40.09	6.85	1.297	1.297
	41.75	6.85	1.245	1.246
$\bar{3}31$; $\bar{2}3\bar{1}1$	43.48	6.21	1.318	1.320
	44.98	6.10	1.297	1.297
	46.93	6.10	1.243	1.246
$13\bar{3}$; $21\bar{3}1$	44.05	6.14	1.316	1.320
	45.51	6.03	1.297	1.297
	47.45	6.03	1.244	1.246

In order to describe the uniaxial deformation of the $In_xGa_{1-x}As$ lattice we transform the cubic lattice of the shell into a hexagonal one and use hexagonal indices. The hexagonal Miller-indices of $(hkil)^h$ can be calculated form the cubic Miller-indices of $(HKL)^c$ by the following transformation matrix relation 4.22 in the chapter 4.:

$$\begin{pmatrix} h \\ k \\ l \end{pmatrix}_h = \begin{pmatrix} 1/2 & 0 & -1/2 \\ -1/2 & 1/2 & 0 \\ 1 & 1 & 1 \end{pmatrix} \begin{pmatrix} H \\ K \\ L \end{pmatrix}_c \tag{7.4}$$

Resulting in h = (H-L)/2; k = (K-H)/2; i = (L-K)/2; l = H+K+L.

Depending on equation (4) it transforms $(31\bar{3})^c$ to $(3\bar{1}\bar{2}1)^h$, for example, and subsequently for all other reflections of the family. In this case the [111] axis of cubic unit cell becomes the c-axis of hexagoal lattice for GaAs and using a_{cub} = 5.653 Å the a and c lattice parameters of an undeformed cubic lattice become a_{hex}= 3.997 Å; c_{hex} = 9.7913 Å following in a a/c ratio of $(a_{hex}/c_{hex})^2$=0.1666. Considering the hexagonal coordinate system, the d(khil)-values follow the relation shown in equation (7.3).

Due to pseudomorph growth, the d(111)-values of GaAs and d(0002) $In_xGa_{1-x}As$ for cubic and hexagonal setting are the same. This results in a compressive deformation of $In_xGa_{1-x}As$ lattice along the growth axis but lattice expansion perpendicular. Considering c_{hex}=9.7913 Å from GaAs, the lattice parameter a_{hex} and the (a/c) ratio of $In_xGa_{1-x}As$ can be determined for all reflections of one family. In case of a perfect hexagonal setting, the (a/c) ratio is 3.997/9.7913 = 0.4082. Using c_{hex} ($In_xGa_{1-x}As$) = √3 a(GaAs) and calculating the in-plane lattice parameter a_{hex} from equ. (7.3), we obtain the experimental a/c ratio. For the measured $(1\bar{3}3)$ reflection, it yields to 4.0509/9.7913= 0.4137, which corresponds to a 1.35 % deformation with respect to cubic case and the respective In content is x = 0.21 for this particular reflection. The In content is deduced considering *Vegard's* rule $a_{exp.} = d_{exp.}\sqrt{H^2+K^2+L^2} = 0.970\sqrt{1+9+25} = 6.0583 - 0.405(1-x)$ (A°)resulting in x = 21.06%. In similar way, the d-values and In content in the $In_xGa_{1-x}As$ shell of all peaks of reflection family $\{1\bar{3}3\}$ were calculated and shown exemplarily in Table 7.4. As it can be seen, the In content differs for each reflection. This is a result of the small misalignment of

the reflected beam direction with respect to the [111] growth axis that changes the Bragg peak energy.

Table 7.4 shows the List of the lattice parameter a_{hex} and avarage of In content of the $In_xGa_{1-x}As$ for all peaks of reflection family $\{1\overline{3}3\}$ and the deduced x values before correction for misalignment.

HKL ; hkil	d(exp.) [Å]	a_{hex}[Å]	$\frac{a_{hex}}{c_{hex}}$	$(\frac{a_{hex}}{c_{hex}})^2$	$\left(\frac{a_{hex} - a_{hex(GaAs)}}{a_{hex(GaAs)}}\right)$%	XRD [In] (%)
$31\overline{3}$; $3\overline{1}\overline{2}1$	1.314	4.0509	0.4137	0.1712	1.35	18.7
$3\overline{3}1$; $1\overline{3}21$	1.316	4.0572	0.4143	0.1717	1.51	21.1
$1\overline{3}3$; $\overline{1}\overline{2}31$	1.317	4.060	0.4146	0.1719	1.59	21.9
$\overline{3}13$; $\overline{3}211$	1.314	4.0509	0.4137	0.1712	1.35	18.6
$\overline{3}31$; $\overline{2}3\overline{1}1$	1.318	4.0635	0.4150	0.1722	1.66	23.1
$13\overline{3}$; $21\overline{3}1$	1.316	4.0572	0.4144	0.1717	1.51	20.6

In the same way, the Bragg peak energy, lattice parameter a_{hex} and mean of In content of the $In_xGa_{1-x}As$ were calculated for all peaks of reflection families $\{1\overline{3}3\}$, $\{5\overline{1}\overline{3}\}$, $\{5\overline{5}1\}$,$\{3\overline{5}3\}$, and $\{7\overline{7}3\}$. The data are shown in **Table S1** of the supplement. The energy of all peaks of the mentioned reflection families again are modified by the non-perpendicular incidence of the beam with respect to 111 growth axis. For correction, one needs the correct azimuthal angles and the correct signs of Miller indices of the reflection families. These have been calculated using the stereographic projection along 111 as shown in figure 7.5.

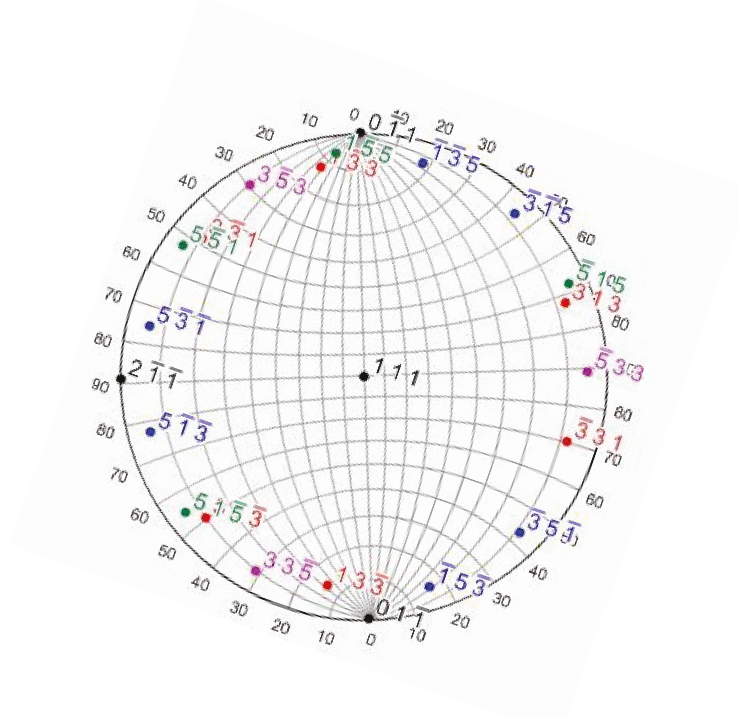

Figure 7.5 The stereographic projection of 111 GaAs for all peaks of reflection families $\{1\overline{3}3\}$, $\{5\overline{1}\overline{3}\}$, $\{5\overline{5}1\}$, $\{3\overline{5}3\}$, and $\{7\overline{7}3\}$ with correct signs along the azimuthal direction.

The angles between (HKL) and the 111 direction were used to correct energies of the Bragg diffractions. The correction was made considering the following procedure. The pnCCD detector has active area of 28.8 x 28.8 mm^2 (384×384 pixels with 75×75 μm^2 pixel size). The corrected Bragg angle (θc) and energy E_c of a peak depends on the misalignment angle α as shown in equations (7.5). α can be negative or positive for different reflections of the same family depending on the local incidence angle. Using the geometry shown on figure 7.6 we obtain

$$E_c = \frac{h.c}{2\,d\sin(\theta_c)} = \frac{E_i\sin(\theta_B)}{\sin(\theta_c)} \quad , \tag{7.5}$$

where

$$\theta_c = \frac{1}{2}\tan^{-1}\frac{R}{\sqrt{R^2+L_1^2}} = \frac{1}{2}\tan^{-1}\frac{R}{\sqrt{R^2+L^2(1-sin^2(\alpha))}}$$

using

$$L_3 = L.\sin(\alpha) \quad ; \; L_1 = \sqrt{L^2 - L_3^2} = \sqrt{L^2(1 - sin^2(\alpha))} \quad ; \alpha = \tan^{-1}(\frac{L_3}{L_1})$$

Here L = 55.80 mm is the distance between the sample and the detector and L_3 is the distance between the fixed detector position (X0 = 217, Y0 =150) and the position (X=207, Y=186) of the 111 reflection where the beam is perpendicular to the surface of the pnCCD detector. After derivation, the relation between the pixel size (ΔR= 0.075 µm) and energy E_i, the energy correction of a measured Laue spot, is given by:

$$\Delta E_c = E_i \frac{\tan\theta_B}{(\tan\theta_B - R/2L_1)^2} \frac{\Delta R}{2L_1} \tag{7.6}$$

Using eq. 7.5, Ec$\{1\bar{3}3\}$ = 35.413 keV for all reflections of the $\{1\bar{3}3\}$ reflection familiy, for example.

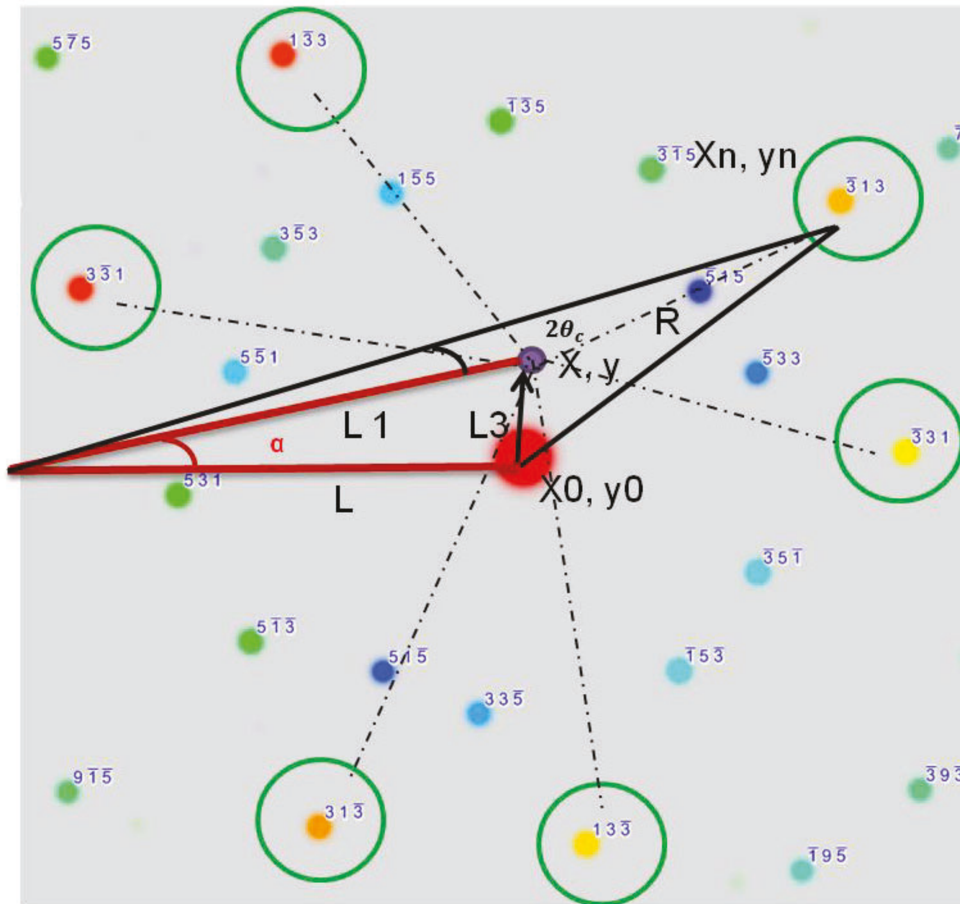

Figure 7.6 Laue pattern of InGaAs in a single exposure of the sample at distance of L = 55.8 mm. The 50 x 50µm^2 white beam is incident parallel to the [111]

growth axis. The NWs generate several Bragg peaks at particular position of the sample and at fixed detector position (X_0 = 217, Y_0 =150). (X_n,Y_n) are positions of Laue spots collected with one pnCCD image covering an area of 384 x 384 pixels. (X=207, Y=186) is the position of 111 reflection where the beam is perpendicular to the surface of pnCCD detector.

Table 7.5 shows the List of the lattice parameter a-hex and average of In content of the $In_xGa_{1-x}As$ for all peaks of reflection families $\{1\bar{3}3\}$, $\{5\overline{13}$, $\{5\bar{5}1\}$,$\{3\bar{5}3\}$ and $\{7\bar{7}3\}$ after the correction.

HKL ; hkil	E(keV)	θ[deg]	θc[deg]	Ec(keV)	d [A°]	a_{hex}[A°]	$\frac{a_{hex}}{c_{hex}}$	$(\frac{a_{hex}}{c_{hex}})^2$	$\left(\frac{a_{hex}-a_{hex(GaAs)}}{a_{hex(GaAs)}}\right)$%	XRD [In] (%)
$31\bar{3}$; $3\bar{1}\bar{2}1$	38.99	6.95	7.61	35.411	1.32177	4.0753	0.41623	0.1732	1.96113	26.2±1.3
$3\bar{3}1$;$1\bar{3}21$	31.68	8.55	7.62	35.411	1.3216	4.0748	0.41617	0.1732	1.94757	26.5±13
$1\bar{3}3$; $\bar{1}\bar{2}31$	31.37	8.63	7.62	35.413	1.32135	4.0740	0.41609	0.1731	1.92815	26.9±1.4
$\bar{3}13$; $\bar{3}211$	39.05	6.94	7.61	35.412	1.32191	4.0758	0.41627	0.1732	1.97177	26.0±1.3
$\bar{3}31$; $\bar{2}3\bar{1}1$	43.48	6.21	7.61	35.411	1.32177	4.0753	0.41623	0.1732	1.96113	26.8±1.5
$13\bar{3}$; $21\bar{3}1$	44.05	6.14	7.61	35.419	1.32182	4.0755	0.41624	0.1732	1.96481	26.1±1.4
$\bar{1}\bar{3}5$; $\bar{3}\bar{1}41$	59.18	6.02	5.61	65.249	0.97344	4.0729	0.41598	0.1730	1.9002	25.9±1.2
$\bar{3}\bar{1}5$; $\bar{4}131$	65.44	5.62	5.6	65.242	0.97338	4.0726	0.41595	0.1730	1.89293	26.3±1.3
$5\bar{1}\bar{3}$; $4\bar{3}\bar{1}1$	65.91	5.59	5.6	65.241	0.97356	4.0734	0.41603	0.1730	1.91282	25.3±1.1
$5\bar{3}\bar{1}$; $3\bar{4}11$	60.48	6.08	5,61	65.254	0.9732	4.0719	0.41587	0.1729	1.8742	26.4±15
$1\bar{5}5$; $\bar{2}\bar{3}51$	77.07	5.74	4.63	95.051	0,80658	4.0735	0.41604	0.1730	1.91455	26.4±1.5
$5\bar{5}1$; $2\bar{5}31$	77.23	5.72	4.64	95.072	0.80657	4.0735	0.41603	0.1730	1.91396	26.1±1.3
$3\bar{5}3$; $0\bar{4}41$	65.35	6.22	5.06	80.15	0.8785	4.0740	0.41609	0.1731	1.92736	26.9±1.6
$7\bar{7}3$; $2\bar{7}53$	57.04	11.32	9.64	66.101	0.55707	4.0769	0.41638	0.1733	1.99948	26.2±1.4

It turns out that the lattice parameter a_{hex} and In content of the In_xGa_{1-x} As deduced from all measured reflections become rather similar after the correction considering a misalignment angle α = 1.261 degree. Based on this data, the mean

x value is determined to be x = 26.5 ± 1.5 percent which well confirms the nominal value (Table 7.1).

7.5. Conclusion

For the first time, pnCCD detector is applied for energy-dispersive Laue diffraction of semiconductor nano-materials, namely NWs, using white synchrotron radiation in the energy range of 20 to 120 keV. We investigate GaAs/$In_xGa_{1-x}As$/GaAs core-shell NWs grown onto Si (111) substrate. The experiment provides Laue spots of various {HKL} families such as $\{1\bar{3}3\}$, $\{5\overline{13}\}$, $\{5\bar{5}1\}$,$\{3\bar{5}3\}$, and $\{7\bar{7}3\}$ simultaneously without any sample rotation by single shot exposure. The mean In content of the $In_xGa_{1-x}As$ shell was calculated from all peaks of these reflection families. A small the small misalignment of the reflected beam direction with respect to the [111] growth axis originated small changes in the Bragg peak energies. After correction by α = 1.261 degree the mean x value is determined to be x = 26.5 ± 1.5 percent. The experiment demonstrates the capability for a fast determination of the strain state in pseudomorph grown semiconductor core- shell systems.

7.6. Supplement

Table S1 List of theta angles and energies of all peaks of reflection families $\{1\bar{3}3\}$, $\{5\bar{1}\bar{3}\}$, $\{5\bar{5}1\}$,$\{3\bar{5}3\}$ and $\{7\bar{7}3\}$. Where d(th.) is estimate for a cubic lattice.

HKL ; hkil	E (keV)	Theta[deg]	d(exp.) [A˚]	d(th.) [A˚]
$31\bar{3}$; $3\bar{1}\bar{2}1$	38.99	6.95	1.314	1.320
	40.02	6.86	1.297	1.297
	41.66	6.86	1.245	1.246
$3\bar{3}1$;$1\bar{3}21$	31.68	8.55	1.316	1.320
	32.50	8.46	1.297	1.297
	33.87	8.48	1.244	1.246
$1\bar{3}3$; $\bar{1}\bar{2}31$	31.37	8.63	1.317	1.320
	32.26	8.52	1.297	1.297
	33.70	8.52	1.244	1.246
$\bar{3}13$; $\bar{3}211$	39.05	6.94	1.314	1.320
	40.09	6.85	1.297	1.297
	41.75	6.85	1.245	1.246
$\bar{3}31$; $\bar{2}3\bar{1}1$	43.48	6.21	1.318	1.320
	44.98	6.10	1.297	1.297
	46.93	6.10	1.243	1.246
$13\bar{3}$; $21\bar{3}1$	44.05	6.14	1.316	1.320
	45.51	6.03	1.297	1.297
	47.45	6.03	1.244	1.246
$\bar{1}\bar{3}5$; $\bar{3}\bar{1}41$	59.18	6.20	0.970	0.972
	61.01	6.11	0.955	0.956

	63.51	6.11	0.917	0.918
$\bar{3}\,\bar{1}\,5\,;\,\bar{4}131$	65.44	5.62	0.968	0.972
	67.36	5.53	0.955	0.956
	70.16	5.53	0.917	0.918
$5\,\bar{1}\,\bar{3}\,;\,4\bar{3}\,\bar{1}1$	65.91	5.59	0.966	0.972
	67.74	5.50	0.955	0.956
	70.61	5.50	0.916	0.918
$5\,\bar{3}\,\bar{1}\,;\,3\bar{4}11$	60.48	6.08	0.968	0.972
	62.29	5.98	0.955	0.956
	64.88	5.98	0.918	0.918
$1\,\bar{5}\,5\,;\,\bar{2}\,\bar{3}51$	77.07	5,74	0.805	0.806
	79.56	5.65	0.791	0.791
	82.87	5.65	0.760	0.761
$5\,\bar{5}\,1\,;\,2\,\bar{5}31$	77.23	5.72	0.806	0.806
	79.72	5.64	0.791	0.791
	83.15	5.64	0.759	0.760
$3\,\bar{5}\,3\,;\,0\,\bar{4}41$	65.35	6.22	0.876	0.877
	67.47	6.12	0.862	0.862
	70.31	6.12	0.827	0.828
$7\,\bar{7}\,3\,;\,2\bar{7}53$	57.04	11.32	0.554	0.556
	58.32	11.22	0.546	0.546
	60.75	11.22	0.524	0.525

Table S2 List of the lattice parameter a_{hex} and avarage of In content of the $In_{21}Ga_{79}As$ for all peaks of reflection families $\{1\bar{3}3\}$, $\{5\bar{1}\bar{3}\}$, $\{5\bar{5}1\}$,$\{3\bar{5}3\}$ and $\{7\bar{7}3\}$.

HKL ; hkil	E(keV)	Theta [deg]	d(exp.) [Å]	a_{hex}[Å]	$\frac{a_{hex}}{c_{hex}}$	$(\frac{a_{hex}}{c_{hex}})^2$	$\left(\frac{a_{hex} - a_{hex(GaAs)}}{a_{hex(GaAs)}}\right)\%$	XRD [In] (%)
$31\bar{3};3\bar{1}\bar{2}1$	38.99	6.95	1.314	4.0509	0.4137	0.1712	1.35	18.7
$3\bar{3}1;1\bar{3}21$	31.68	8.55	1.316	4.0572	0.4143	0.1717	1.51	21.1
$1\bar{3}3;\bar{1}\bar{2}31$	31.37	8.63	1.317	4.060	0.4146	0.1719	1.59	21.9
$\bar{3}13;\bar{3}211$	39.05	6.94	1.314	4.0509	0.4137	0.1712	1.35	18.6
$\bar{3}31;\bar{2}3\bar{1}1$	43.48	6.21	1.318	4.0635	0.4150	0.1722	1.66	23.1
$13\bar{3};21\bar{3}1$	44.05	6.14	1.316	4.0572	0.4144	0.1717	1.51	20.6
$\bar{1}\bar{3}5;\bar{3}\bar{1}41$	59.18	6.02	0.970	4.0584	0.4145	0.1718	1.54	21.6
$\bar{3}\bar{1}5;\bar{4}131$	65.44	5.62	0.968	4.0499	0.4136	0.1711	1.32	17.8
$5\bar{1}\bar{3};4\bar{3}\bar{1}1$	65.91	5.59	0.966	4.0415	0.4128	0.1704	1.11	15.3
$5\bar{3}\bar{1};3\bar{4}11$	60.48	6.08	0.968	4.0499	0.4136	0.1711	1.32	18.4
$1\bar{5}5;\bar{2}\bar{3}51$	77.07	5.74	0.805	4.0655	0.4152	0.1724	1.71	22.9
$5\bar{5}1;2\bar{5}31$	77.23	5.72	0.806	4.0705	0.4157	0.1729	1.84	24.8
$3\bar{5}3;0\bar{4}41$	65.35	6.22	0.876	4.0623	0.4149	0.1721	1.65	22.3
$7\bar{7}3;2\bar{7}53$	57.04	11.32	0.554	4.0538	0.4140	0.1714	1.42	18.8

Chapter 8

8. Conclusion & Outlook

Throughout this work, a detailed investigation of NWs was demonstrated for the first time by using pnCCD detector and energy dispersive Laue diffraction method with ultra-hard X-rays in the energy range between 8 keV and 120 keV. Here a white x-ray beam exposes different suture NWs providing various Laue spots which fulfill the Bragg condition for different x-ray energies. The fast and precise characterization of NWs by this method requires a simultaneous position and energy resolved detection of X-rays. For that purpose a GaAs NWs, InAs NWs and GaAs/$In_xGa_{1-x}As$/GaAs core shell NWs structure was investigated using different highly brilliant white synchrotron radiation and analyzed in transmission geometry by means of a one shot exposure without move or scans the sample.

The first experiment curried out using micro beam to study structures GaAs NWs Grown onto GaAs[111]B. The experimental results of the lattice parameter is in good agreement with that of theoretical value. and the lattice mismatch between the GaAs NWs and substrate was 0.34% probably because different the NWs crystallize in the wurtzite phase with respect to the zinc-blende GaAs substrate The lattice mismatch of the sample using monochromatic x-rays is 0.23%. The agreements of the lattice mismatch between the accuracy which can be achieved by the white using PnCCD detector compared with the accuracy achievable by monochromatic x-rays is in range of 0.11%.

The following measurement of pnCCD for hard X-ray exposure is tested at EDR beamline of BESSY II synchrotron for analysis of the InAs NWs planted on GaAs (111) substrate. The experimental and theoretical values of lattice parameters for GaAs substrate and InAs NRs are in good agreement are in range of 0.1%. The achieved accuracy is comparable to the result of a previous Laue

diffraction experiment by monochromatic x-rays is in range of 0.2%. Using high and wide range of energy gives advantages of having more Laue patterns resolved in a large reciprocal space volume. This experiment clearly demonstrated the potential of pnCCD detectors for applications in semiconductor nanomaterials science using total X-ray Spectrum.

Finaly, pnCCD detector is applied for energy-dispersive Laue diffraction of semiconductor nano-materials, namely NWs, using white synchrotron radiation in the energy range of 20 to 120 keV. We investigate GaAs/$In_xGa_{1-x}As$/GaAs core-shell NWs grown onto Si (111) substrate. The experiment provides Laue spots of various {HKL} families such as $\{1\bar{3}3\}$, $\{5\overline{13}\}$, $\{5\bar{5}1\}$,$\{3\bar{5}3\}$, and $\{7\bar{7}3\}$ simultaneously without any sample rotation by single shot exposure. The mean In content of the $In_xGa_{1-x}As$ shell was calculated from all peaks of these reflection families. A small the small misalignment of the reflected beam direction with respect to the [111] growth axis originated small changes in the Bragg peak energies. After correction by $\alpha = 1.261$ degree the mean x value is determined to be $x = 26.5 \pm 1.5$ percent. This experiment demonstrates the capability for a fast determination of the strain state in pseudomorph grown semiconductor core- shell systems. Also recently, this measurement has been performed to check the indium distribution within the GaAs/$In_xGa_{1-x}As$/GaAs core-shell NWs. In that respect, the potential of pnCCD for X-ray structure NWs analysis based on energy-dispersive Laue diffraction with white synchrotron radiation could be demonstrated over the complete experimentally accessible energy range provided by a storage ring.

Outlook

Subsequent work will concentrate on the application of Laue diffraction to study the structure of individual nanowire with different diameters and the influence of size effects using nano white beam and pnCCD detector as we see in Figure 8.1 using monochromatic beam [113] where the peak positions of the ZB and WZ phase observed in the asymmetric reflection geometry for individual nanowire GaAs. But the left panel in figure 8.1 shows an ensemble averaged reciprocal space map of the GaAs NWs allowed for both ZB and WZ structures. Due to larger lattice parameters of WZ and ZB GaAs the Bragg peak of the NWS is located at smaller vertical momentum transfer and ZB and WZ segments diffract at different values of Qz, reflected by overlap of two peaks. The previous results are agreement with the EDDI results using InAs NWs. Therefore if study of the structure of individual nanowire (InAs) using nano white beam will be implemented, the peak positions of the ZB and WZ phase could be separate because there is one lattice parameters of the ZB and WZ of individual NW (InAs).

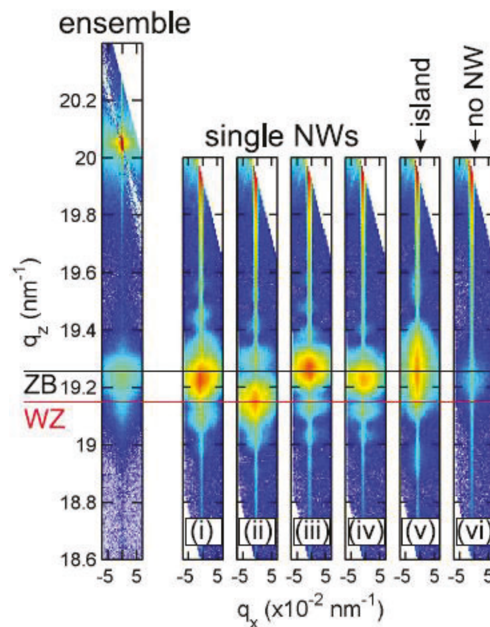

Figure 8.1 Reciprocal space maps around the GaAs $(111)^c$ reflection. Left: Ensemble measurement, showing the Si and GaAs $(111)^c$ reflections. Right: measurements on single NWs with a focussed x-ray beam. NW lattice parameters

fluctuate around the average values. If no NW is illuminated (vi), only a small signal is observed, caused by the long tails of the focussed x-ray beam still illuminating wires. Colorscale: log (intensity). Average and single measurements are on different scale due to focussing.

9. Bibliography

[1] M.T.Björk, et al., Few-electron quantum dots in nanowires. Nano Letters, 4(9): p. 1621-1625, 2004.

[2] P. Yang, R. Yan, and M. Fardy, Semiconductor nanowire: What's next, Nano Letters 10, 1529, 2010.

[3] F. Qian, S. Gradecak, Y. Li, C.-Y. Wen, and C. Lieber, "Core/multishell nanowire heterostructures as multicolor, high-efficiency light-emitting diodes," Nano Lett., vol. 5, no. 11, pp. 2287–2291, 2005.

[4] M. H. Huang, S. Mao, H. Feick, H. Yan, Y. Wu, H. Kind, E. Weber, R. Russo, and P. Yang, "Room temperature ultraviolet nanowire nanolasers," Science, vol. 292, no. 5523, pp. 1897–1899, 2001.

[5] X. F. Duan, Y. Huang, R. Agarwal, and C. M. Lieber, "Single-nanowire electrically driven lasers," Nature, vol. 421, no. 6920, pp. 241–245, 2003.

[6] J. Wang, M. S. Gudiksen, X. Duan, Y. Cui, and C. M. Lieber, "Highly polarized photoluminescence and photodetection from single indium phosphide nanowires," Science, vol. 293, no. 5534, pp. 1455–7, 2001.

[7] Y. Gu, E.-S. Kwak, J. L. Lensch, J. E. Allen, T.W. Odom, and L. J. Lauhon, "Nearfield scanning photocurrent microscopy of a nanowire photodetector," Appl. Phys. Lett., vol. 87, no. 4, p. 043111, 2005.

[8] H. Pettersson, J. Tr¨ag˚ardh, A. I. Persson, L. Landin, D. Hessman, and L. Samuelson, "Infrared photodetectors in heterostructure nanowires," Nano Lett., vol. 6, no. 2, pp. 229–232, 2006.

[9] Y. Cui, Z. Zhong, D. Wang, W. U. Wang and C. M. Lieber, "High Performance Silicon Nanowire Field Effect Transistors," Nano Letters, Vol. 3, No. 2, pp. 149-152, 2003.

[10] H. T. Ng, J. Han, T. Yamada, P. Nguyen, Y. P. Chen, and M. Meyyappan, "Single crystal nanowire vertical surround-gate field-effect transistor," Nano Lett., vol. 4, no. 7, pp. 1247–1252, 2004.

[11] T. Bryllert, L.-E.Wernersson, T. Lowgren, and L. Samuelson, "Vertical wrap-gated nanowire transistors," Nanotechnology, vol. 17, no. 11, p. S227, 2006.

[12] E. Lind, A. I. Persson, L. Samuelson, and L.-E.Wernersson, "Improved subthreshold slope in an InAs nanowire heterostructure field-effect transistor," Nano Lett.,vol. 6, no. 9, pp. 1842–1846, 2006.

[13] M. T. Bjork, O. Hayden, H. Schmid, H. Riel, and W. Riess, "Vertical surroundgated silicon nanowire impact ionization field-effect transistors," Appl. Phys. Lett., vol. 90, no. 14, p. 142110, 2007.

[14] C. Thelander, P. Agarwal, S. Brongersma, J. Eymery, L. F. Feiner, A. Forchel, M. Scheffler, W. Riess, B.J.Ohlsson, U. Gösele, and L. Samuelson " Nanowire-based one-dimensional electronics ", Materials Today vol. 9 (10) p. 28, 2006.

[15] M. Law, L. E. Greene, J. C. Johnson, R. Saykally, and P. Yang, "Nanowire dyesensitized solar cells," Nature Mater., vol. 4, no. 6, pp. 455–459, 2005.

[16] E. C. Garnett and P. Yang, "Silicon nanowire radial p–n junction solar cells," J. Am. Chem. Soc., vol. 130, no. 29, pp. 9224–9225, 2008.

[17] Y. Dong, B. Tian, T. J. Kempa, and C. M. Lieber, “Coaxial group III–nitride nanowire photovoltaics,” Nano Lett., vol. 9, no. 5, pp. 2183–2187, 2009.

[18] J. A. Czaban, D. A. Thompson, and R. R. LaPierre, “GaAs core-shell nanowires for photovoltaic applications,” Nano Lett., vol. 9, no. 1, pp. 148–154, 2009.

[19]O. L. Krivanek, M. F. Chisholm, V. Nicolosi, T. J. Pennycook, G. J. Corbin, N. Dellby, M. F. Murfitt, C. S. Own, Z. S. Szilagyi, M. P. Oxley, S. T. Pantelides, O. L. Krivanek, G. J. Corbin, N. Dellby, B. F. Elston, R. J. Keyse, M. F. Murfitt, J. Nature 464, 571-574, 2010.

[20] D.T. Nguyen, S.D. Findlay, J. Etheridge, Ultramicroscopy, vol. 146, pp. 6-16,. 2014.

[21] K. Ikejiri, J. Noborisaka, S. Hara, J. Motohisa, T. Fukui. Journal of Crystal Growth 298, 616-619, 2007.

[22] X. Dai, A. Messanvi, H. Zhang, C. Durand, J. Eymery, C. Bougerol, F. H. Julien & M. Tchernycheva, Nano Lett. **15**, 6958 -6964, 2015.

[23] M. Heiss, Y. Fontana, A. Gustafsson, G. Wüst, C. Magen, D. D. O’Regan, J. W. Luo, B. Ketterer, S. Conesa-Boj, A. V. Kuhlmann, J. Houel, E. Russo-Averchi, J. R. Morante, M. Cantoni, N. Marzari, J. Arbiol, A. Zunger, R. J. Warburton, and A. F. Morral, Nature Mater. 12, 439, 2013.

[24] R.B. Lewis, P. Corfdir, J. Herranz, H. Küpers, U. Jahn, O. Brandt and L. Geelhaar, “Self-assembly of InAs nanostructures on the sidewalls of GaAs nanowires directed by a Bi surfactant,” Nano Letters 17, 4255−4260,2017.

[25] K. Tomioka, J. Motohisa, S. Hara and T. Fukui, "Control of InAs nanowire growth directions on Si," Nano Lett., vol. 8, p. 3475–3480, 2008.

[26] Paetzelt, H., Gottschalch,V., Bauer, J., Benndorf, G. &Wagner, G., (2008). Journal of Crystal Growth Vol. 310, Issue 23, p. 5123-5128, 2008.

[27] K. A. Dick , J. Bolinsson , B. M. Borg and J. Johansson , Nano Lett., 12 , 3200 —3206,2012.

[28] A. Davtyan, S. Lehmann, D. Kriegner, R. R. Zamani, K. Dick, D. Bahrami, A. Al-Hassan, S. J. Leake, U. Pietsch, V. Holy: Characterisation of individual stacking faults in a wurtzite GaAs nanowire by Nanobeam x-ray diffraction, J. Appl. Cryst. 50, 673–680, 2017.

[29] A. Al Hassan, A.Davtyan, H. Küpers, R. B. Lewis, D. Bahrami, F. Bertram, G. Bussone, C. Richter, L. Geelhaar & U. Pietsch J. Appl. Cryst. 51, 1387-1395, 2018. ; A. Al Hassan, A., R. B Lewis., H. Ku¨ pers, W.-H. Lin, D. Bahrami, T. Krause, D. Salomon, A. Tahraoui, M. Hanke, L. Geelhaar& U. Pietsch Phys. Rev. Mater. **2**, 014604, 2018.

[30] Strüder, L. et al. (2001). Astron. Astrophys. 365, L18-L26; L. Strüder, U. Briel, K. Dennerl, et al., “The European Photon Imaging Camera on XMM-Newton: The pn-CCD camera”, Astronomy & Astrophysics, vol. 365, 1, pp. L18-L26, 2001.

[31] P. Predehl, A. Deresch, H. Böhringer, et al., “eROSITA: an extended X-ray survey telescope”, in Space Telescopes and Instrumentation II: Ultraviolet to Gamma Ray, G. Hasinger and M. J. L. Turner, eds., Proc. SPIE 6266, 2006.

[32] N. Meidinger, N. Andritschke, R. Hartmann, S. Herrmann, p. Holl, G. Lutz, & L. Strüder Nucl. Instrum. Methods Phys. Res. Sect. A, 565, 251-257, 2006.
[33] N. Meidinger, R. Andritschke, O. Halker, et al., Proceedings of the SPIE, 6686, 66860H-1, doi: 10.1117/12.787793, 2007.

[34] N. Meidinger, R. Andritschke, J. Elbs, et al., Proceedings of the SPIE, 7011, 70110J, doi: 10.1117/12.787793, 2008.

[35] G. Schächner, R. Andritschke., O. Hälker,S. Herrmann., N. Kimmel, N. Meidinger& L. Strüder, Nucl. Instrum. Methods Phys. Res. Sect. A, 624, 330-333, 2010.

[36] S. H. Nowak, A. Bjeoumikhov, J. von Borany, J. Buchriegler, F. Munnik, M. Petric, A. D. Renno, M. Radtke, U. Reinholz, O. Scharf, L. Strüder, R. Wedell, and R. Ziegenrücker, X-Ray Spectrom. 44, 135 https://doi.org/10.1002/xrs.2590, 2015.

[37]W. Leitenberger, R. Hartmann, U. Pietsch, R. Andritschke,I. Starke, L. Strüer , Application of a pnCCD in X-ray diffraction: a three dimensional X-ray detector, J. Synchrotron Rad. 15, 449-457, 2008.

[38] S. Send, M. von Kozierowski, T. Panzner, S. Gorfman, K. Nurdan, A. H. Walenta, U. Pietsch, W. Leitenberger, R. Hartmann, L. Strüder(2009). J. Appl. Cryst Vol. 42, Pages: 1139-1146, Part: 6, 2009.

[39] S. Send, A. Abboud, R. Hartmann, M. Huth, W. Leitenberger, N. Pashniak, J. Schmidt, L. Strüder, U. Pietsch, J. Appl. Cryst. **45**, 517-522, 2012.

[40]S. Send, A. Abboud, R. Hartmann, M. Huth, W. Leitenberger, N Pashniak, J. Schmidt, L. Strüder, U. Pietsch, Nucl. Instrum. Methods Phys. Res. Sect. Vol. 711, Pages 132–142; DOI: 10.1016/j.nima.2013.01.044, 2013.

[41] S. Send, A. Abboud, N. Wiesner, M. Shokr, M. Klaus, C. Genzel, T. Conka-Nurdan, D. Schlosser, M. Huth, R. Hartmann, L. Strüder, U. Pietsch. Application 49, 222-233, Part 1; DOI: 10.1107/S1600576715023997, 2016.

[42] Abboud, A., Kirchlechner, C., Send, S., Micha, J.-S., Ulrich, O., Pashniak, N., Strüder, L., Keckes, J. & Pietsch, U. (2014). *Rev. Sci. Instrum.* 85, 113901.

[43] Abboud, A, Kirchlechner, C., Keckes, J., Nurdan,T., C., Send, S., Mich, J.S., Ulrich, O., Hartmann, R.,Strüder, L., and Pietsch, U. Appl. Cryst. 50, 901–908, 2017.

[44] K. Nurdan, T. Conka Nurdan, M. AL-Taani, H. Yousef, A. H. Walenta, K. Walenta, A. Abboud, A. Nasr, O. Riibsamen, W. Schenk, U. Pietsch, S. Send, R. Hartmann, W. Leitenberger, L. Stroder, (Simultaneous acquisition of K-edge subtraction images using a pnCCD), 2008.

[45] R. Andritschke, G. Hartner, R. Hartmann, N. Meidinger, L. Striider (Data Analysis for Characterizing pn-CCDs), Nuclear Science Symposium Conference Record, NSS 08. IEEE, 2166-2172, 2008.

[46] L. Struder, J. Englhauser, R. Hartmann, P. Holl, N. Meidinger, H. Soltau, U. Briel, K. Dennerl, M. Freyberg, F. Haberl, G. Hartner, E. Pfeffermann, T. Stadlbauer, E. Kendziorra (pn-CCDs on XMM-Newton-42 months in orbit) Nuclear Instruments and Methods in Physics Research, A 512, 2003.

[47] S. Herrmann, W. Buttler, R. Hartmann, P. Holl, N. Meidinger, L. Strueder, (Mixed signal pn-CCD readout ASIC for the future X-Ray astronomy mission eROSITA), Nuclear Science Symposium Conference Record, NSS '07. IEEE, vol.3, no., pp.2398-2403, Oct. 26 2007-Nov. 3 2007.doi: 10.1109/NSSMIC.2007.4436626, 2007.

[48] R. C. Alid, S. Bloom, and W. Struck, “Scattering by ionization and phonon emission in semiconductors,” Physical Review B, vol. 22, no. 12, pp. 5565–5582, 1980.

[49] S. Send, A. Abboud, R. Hartmann, M. Huth, W. Leitenberger, N. Pashniak, J.Schmidt, L. Strüder, and U. Pietsch, Characterization of a pnCCD for applications with synchrotron radiation, Nuclear Instruments and Methods in Physics Research A 711, 132-142, 2013.

[50] I. Ordavo, S. Ihle, V. Arkadiev, O. Scharf, H. Soltau, A. Bjeoumikhov, S. Bjeoumikhova, G. Buzanich, R. Gubzhokov, A. G¨unther, R. Hartmann, P. Holl, N. Kimmel, M. K¨uhbacher, M. Lang, N. Langhoff, A. Liebel, M. Radtke, U. Reinholz, H. Riesemeier, G. Schaller, F. Schopper, L. Strüder, C. Thamm, and R. Wedell, A new pnCCD-based color X-ray camera for fast spatial and energy-resolved measurements, Nuclear Instruments and Methods in Physics Research A 654, 250-257, 2011.

[51] S. Send, Utilization of a frame store pnCCD for energy-dispersive Laue diffraction with white synchrotron radiation. Doktorarbeit, Universität Siegen, 2012.

[52] D. E. Grider, A Wright, and P. K. Ausburn, “Electron beam melting in microfocus x-ray tubes”, J. Phys. D: Appl. Phys. 19: 2281-2292, 1986.

[53] N. Meidinger, L. Strüder, P. Holl, H. Soltau, and C. von Zanthier, Analysis of trapping effects on charge transfer in proton irradiated pn-CCDs, Nuclear Instruments and Methods in Physics Research A 377, 298-311, 1996.

[54] M. Shokr L. Strüder, and U. Pietsch, PnCCD Response to Hard X-Ray Radiation,thesis 2015.

[55] O. Hayden, R. Agarwal, and W. Lu, “Semiconductor nanowire devices,” *Nano Today*, vol. 3, pp. 12–22, Oct. 2008.

[56] P. E. Landreman and M. L. Brongersma, “Deep-subwavelength semiconductor nanowire surface plasmon polariton couplers,” *Nano Letters*, vol. 14, no. 2, pp. 429–434, 2014.

[57] A. I. Hochbaum, R. Chen, R. D. Delgado, W. Liang, E. C. Garnett, M. Najarian, A. Majumdar, and P. Yang, “Enhanced thermoelectric performance of rough silicon nanowires,” *Nature*, vol. 451, pp. 163–167, Jan. 2008.

[58] K. L. Kavanagh, “Misfit dislocations in nanowire heterostructures,” *Semiconductor Science and Technology*, vol. 25, p. 024006, Feb. 2010.

[59] Björk, M.T., et al., Few-electron quantum dots in nanowires. Nano Letters, 4(9): p. 1621-1625, 2004.

[60] P. Yang, R. Yan, and M. Fardy, Semiconductor nanowire: What’s next?, Nano Letters 10, 1529, 2010.

[61] F. Qian, S. Gradecak, Y. Li, C.-Y. Wen, and C. Lieber, “Core/multishell nanowire heterostructures as multicolor, high-efficiency light-emitting diodes,” Nano Lett., vol. 5, no. 11, pp. 2287–2291, 2005.

[62] E. D. Minot, F. Kelkensberg, M. van Kouwen, J. A. van Dam, L. P. Kouwenhoven, V. Zwiller, M. T. Borgstr¨om, O. Wunnicke, M. A. Verheijen, and E. P. A. M. Bakkers, “Single quantum dot nanowire LEDs,” Nano Lett., vol. 7, no. 2, pp. 367–371, 2007.

[63] K. Tomioka, J. Motohisa, S. Hara, K. Hiruma, and T. Fukui, GaAs/AlGaAs core multishell nanowire-based light-emitting diodes on Si, Nano Letters 10, 1639, 2010.

[64] M. T. Bj¨ork, B. J. Ohlsson, C. Thelander, A. I. Persson, K. Deppert, L. R. Wallenberg, and L. Samuelson, "Nanowire resonant tunneling diodes," Appl. Phys. Lett., vol. 81, no. 23, pp. 4458–4460, 2002.

[65] M. H. Huang, S. Mao, H. Feick, H. Yan, Y. Wu, H. Kind, E. Weber, R. Russo, and P. Yang, "Room temperature ultraviolet nanowire nanolasers," Science, vol. 292, no. 5523, pp. 1897–1899, 2001.

[66] X. F. Duan, Y. Huang, R. Agarwal, and C. M. Lieber, "Single-nanowire electrically driven lasers," Nature, vol. 421, no. 6920, pp. 241–245, 2003.

[67] R. Agarwal, C. J. Barrelet, and C. M. Lieber, "Lasing in single cadmium sulfide nanowire optical cavities," Nano Lett., vol. 5, no. 5, pp. 917–920, 2005.

[68] A. H. Chin, S. Vaddiraju, A. V. Maslov, C. Z. Ning, M. K. Sunkara, and M. Meyyappan, "Near-infrared semiconductor subwavelength-wire lasers," Appl. Phys. Lett., vol. 88, no. 16, p. 163115, 2006.

[69] F. Qian, Y. Li, S. Gradecak, H.-G. Park, Y. Dong, Y. Ding, Z. L. Wang, and C. M. Lieber, "Multi-quantum-well nanowire heterostructures for wavelength-controlled lasers," Nature Mater., vol. 7, no. 9, pp. 701–706, 2008.

[70] B. Hua, J. Motohisa, Y. Kobayashi, S. Hara, and T. Fukui, "Single GaAs/GaAsP coaxial core-shell nanowire lasers," Nano Lett., vol. 9, no. 1, pp. 112–116, 2009.

[71] R. Yan, D. Gargas, and P. Yang, Nanowire photonics, Nature Photonics 3 , 569, 2009.

[72] J. Wang, M. S. Gudiksen, X. Duan, Y. Cui, and C. M. Lieber, “Highly polarized photoluminescence and photodetection from single indium phosphide nanowires,” Science, vol. 293, no. 5534, pp. 1455–7, 2001.

[73] Y. Gu, E.-S. Kwak, J. L. Lensch, J. E. Allen, T.W. Odom, and L. J. Lauhon, “Nearfield scanning photocurrent microscopy of a nanowire photodetector,” Appl. Phys. Lett., vol. 87, no. 4, p. 043111, 2005.

[74] H. Pettersson, J. Tr¨ag˙ardh, A. I. Persson, L. Landin, D. Hessman, and L. Samuelson, “Infrared photodetectors in heterostructure nanowires,” Nano Lett., vol. 6, no. 2, pp. 229–232, 2006.

[75] Y. Cui, Z. Zhong, D. Wang, W. U. Wang, and C. M. Lieber, High performance Silicon nanowire field effect transistors, Nano Letters 3 ,149, 2003.

[76] H. T. Ng, J. Han, T. Yamada, P. Nguyen, Y. P. Chen, and M. Meyyappan, “Single crystal nanowire vertical surround-gate field-effect transistor,” Nano Lett., vol. 4, no. 7, pp. 1247–1252, 2004.

[77] T. Bryllert, L.-E.Wernersson, T. Lowgren, and L. Samuelson, “Vertical wrap-gated nanowire transistors,” Nanotechnology, vol. 17, no. 11, p. S227, 2006.

[78] E. Lind, A. I. Persson, L. Samuelson, and L.-E.Wernersson, “Improved subthreshold slope in an InAs nanowire heterostructure field-effect transistor,” Nano Lett.,vol. 6, no. 9, pp. 1842–1846, 2006.

[79] M. T. Bjork, O. Hayden, H. Schmid, H. Riel, and W. Riess, “Vertical surroundgated silicon nanowire impact ionization field-effect transistors,” Appl. Phys. Lett., vol. 90, no. 14, p. 142110, 2007.

[80] C. Thelander, P. Agarwal, S. Brongersma, J. Eymery, L.F. Feiner,A.Forchel,M. Scheffler, W. Riess, B.J. Ohlsson, U. Gösele, and L. Samuelson, Nanowirebased one-dimensional electronics, Materials Today 9, 28, 2006.

[81] C. Thelander, T. Martensson, M. T. Bj¨ork, B. J. Ohlsson, M. W. Larsson, L. R. Wallenberg, and L. Samuelson, “Single-electron transistors in heterostructure nanowires,” Appl. Phys. Lett., vol. 83, no. 10, pp. 2052–2054, 2003.

[82] M. T. Bj¨ork, C. Thelander, A. E. Hansen, L. E. Jensen, M. W. Larsson, L. R.Wallenberg, and L. Samuelson, “Few-electron quantum dots in nanowires,” Nano Lett., vol. 4, no. 9, pp. 1621–1625, 2004.

[83] C. Thelander, H. A. Nilsson, L. E. Jensen, and L. Samuelson, “Nanowire singleelectron memory,” Nano Lett., vol. 5, no. 4, pp. 635–638, 2005.

[84] H. A. Nilsson, C. Thelander, L. E. Fr¨oberg, J. B. Wagner, and L. Samuelson, “Nanowire-based multiple quantum dot memory,” Appl. Phys. Lett., vol. 89, no. 16, p. 163101, 2006.

[85] H. A. Nilsson, T. Duty, S. Abay, C.Wilson, J. B.Wagner, C. Thelander, P. Delsing, and L. Samuelson, “A radio frequency single-electron transistor based on an InAs/InP heterostructure nanowire,” Nano Lett., vol. 8, no. 3, pp. 872–875, 2008.

[86] E. C. Heeres, E. P. A. M. Bakkers, A. L. Roest, M. Kaiser, T. H. Oosterkamp, and N. de Jonge, “Electron emission from individual indium arsenide semiconductor nanowires,” Nano Lett., vol. 7, no. 2, pp. 536–540, 2007.

[87] M. Law, L. E. Greene, J. C. Johnson, R. Saykally, and P. Yang, “Nanowire dyesensitized solar cells,” Nature Mater., vol. 4, no. 6, pp. 455–459, 2005.

[88] E. C. Garnett and P. Yang, “Silicon nanowire radial p–n junction solar cells,” J. Am. Chem. Soc., vol. 130, no. 29, pp. 9224–9225, 2008.

[89] Y. Dong, B. Tian, T. J. Kempa, and C. M. Lieber, “Coaxial group III–nitride nanowire photovoltaics,” Nano Lett., vol. 9, no. 5, pp. 2183–2187, 2009.

[90] J. A. Czaban, D. A. Thompson, and R. R. LaPierre, “GaAs core-shell nanowires for photovoltaic applications,” Nano Lett., vol. 9, no. 1, pp. 148–154, 2009.

[91] C. J. Barrelet, A. B. Greytak, and C. M. Lieber, “Nanowire photonic circuit elements,” Nano Lett., vol. 4, no. 10, pp. 1981–1985, 2004.

[92] M. T. Borgstr¨om, V. Zwiller, E. Muller, and A. Imamoglu, “Optically bright quantum dots in single nanowires,” Nano Lett., vol. 5, no. 7, pp. 1439–1443, 2005.

[93] C. J. Barrelet, J. Bao, M. Lonˇcar, H.-G. Park, F. Capasso, and C. M. Lieber, “Hybrid single-nanowire photonic crystal and microresonator structures,” Nano Lett., vol. 6, no. 1, pp. 11–15, 2006.

[94] H.-G. Park, C. J. Barrelet, Y. Wu, B. Tian, F. Qian, and C. M. Lieber, “A wavelength-selective photonic-crystal waveguide coupled to a nanowire light source,” Nature Photon., vol. 2, no. 10, pp. 622–626, 2008.

[95] S. G. Ihn, J. I. Song, T. W. Kim, D. S. Leem, T. Lee, S. G. Lee, E. K. Koh, and K.Song, Nano Lett., 7, 39, 2007.

[96] X.-Y. Bao, C. Soci, D. Susac, D. P. R. Aplin, W. Wei, C.-Y. Chen, K. L. Kavanagh, and Deli Wang, 2008.

[97] R. G. Hobbs, N. Petkov, and J. D. Holmes, “Semiconductor nanowire fabrication by bottom-up and top-down paradigms,” Chemistry of Materials, vol. 24, no. 11, pp. 1975–1991, 2012.

[98] M.-C. Sun, G. Kim, J. H. Lee, H. Kim, S. W. Kim, H. W. Kim, J.-H. Lee, H. Shin, and B.-G. Park, “Patterning of Si nanowire array with electron beam lithography for sub-22 nm Si nanoelectronics technology,” Microelectronic Engineering, vol. 110, pp. 141 – 146, 2013.

[99] Y., Xia, et al., One-Dimensional Nanostructures: Synthesis, Characterization, and Applications. Advanced Materials, 15(5): p. 353-389, 2003.

[100] R. Wagner, and W. Ellis, Vapor-liquid-solid mechanism of single crystal growth. Applied Physics Letters, 4(5): p. 89-90, 1964.

[101] A. I. Persson, et al., Solid-phase diffusion mechanism for GaAs nanowire growth. Nature Materials, 3(10): p. 677-681, 2004.

[102] J. Thangala, et al., Large-Scale, Hot-Filament-Assisted Synthesis of Tungsten Oxide and Related Transition Metal Oxide Nanowires. small, 3(5): p. 890-896, 2007.

[103] R. Wagner, and W. Ellis, Vapor-liquid-solid mechanism of single crystal growth. Applied Physics Letters, 4(5): p. 89-90, 1964.

[104] J. Bao, et al., Optical properties of rotationally twinned InP nanowire heterostructures. Nano Letters, 8(3): p. 836-841, 2008.

[105] Anton Davydok, M. Sc. thesis, X-ray Diffraction Analysis of InAs Nanowires, 2013.

[106] D. Spirkosk. Structural and optical properties of high quality zincblende/ wurtzite gaas nanowire heterostructures. Phys. Rev. B, page 80(24) 245325, 2009.

[107] Andreas Biermanns, M. Sc. Thesis, X-ray diffraction from single GaAs nanowires, 2012.

[108]O. Madelung, Semiconductors: Data handbook, Springer, Berlin, Heidelberg, ISBN: 3540404880, 2004.

[109] Genziana Bussone. Grazing-incidence x-ray diffraction of single gaas nanowires at locations defined by focused ion beams. J Appl Crystallogr., page 46(Pt 4): 887–892, Aug 1, 2011.

[110] Ashcroft and Mermin, Solid State Physics, Stratford Books, 1976.

[111] B. E. Warren X-ray diffraction (Addison-Wesley, Reading MA/Dover, Mineola NY), (1969/1990).

[112] S. O. Mariager, Structure and dynamics of crystalline nano-systems, Ph.D. thesis, Niels Bohr Institute, University of Copenhagen, 2010.

[113] Andreas Biermanns, M. Sc. Thesis, X-ray diffraction from single GaAs nanowires, 2012.

[114] M. Köhl, Analysis of nanostructures based on diffraction of X-ray radiation. Dissertation, Karlsruhe Institute of Technology, 2014.

[115] P. E. Schroth, Growth of self-catalyzed GaAs nanowires using molecular-beam-epitaxy and structural characterization by in-situ X-ray diffraction. Dissertation. Universität Siegen, 2016.

[116] Bragg, W.L. "The Reflexion of X-rays by Crystals". Proc R. Soc. Lond A 88 (605): 42838. Bibcode :1913RSPSA..88..428B. doi: 10.1098 / rspa.1913.0040, 1913.

[117] M. shoker, book pnccd response to hard x ray 2015.

[118] H. P. Myers, Introductory Solid State Physics. Taylor & Francis. ISBN 0-7484-0660-3, 2002.

[119] Kittel, C. Introduction to Solid State Physics, New York: John Wiley & Sons.ISBN 0-471-49024-5,1976.

[120] C. Kittel, Einf¨uhrung in die Festk¨orperphysik, 14. Auflage, Oldenbourg, M¨unchen, ISBN: 3486577239, 2006.

[121] Z. H. Kalman, On the derivation of integrated reflected energy formulae, Acta Crystallographica A 35, 634-641, 1979.

[122] S. Send, Utilization of a frame store pnCCD for energy-dispersive Laue diffraction with white synchrotron radiation, 2013.

[123] R. Kahn, R. Fourme, A. Gadet, J. Janin, C. Dumas, and D. Andr´e, Macromolecular crystallography with synchrotron radiation: photographic data collection and polarization correction, Journal of Applied Crystallography 15, 330-337,1982.

[124] R. Klein, R. Thornagel, and G. Ulm, Der Speicherring BESSY II als prim¨ares Strahlernormal, PTB-Mitteilungen 115, 172-179, 2005

[125] H. M. Einspahr and M. S. Weiss, Quality indicators in macromolecular crystallography: definitions and applications, International Tables for Crystallography, Volume F, Crystallography of Biological Macromolecules, 64-74, edited by E. Arnold, D. M. Himmel, and M. G. Rossmann, 2nd edition, Wiley, New York, ISBN: 0470660783, 2012.

[126] M. T. Björk, et al., Few-electron quantum dots in nanowires. Nano Letters, 4(9): p. 1621-1625, 2004.

[127] O. Hayden, et al., Visualization of Carrier Depletion in Semiconducting Nanowires. small, 3(12): p. 2048-2052, 2007.

[128] J.A., D.A. Czaban, Thompson, and R.R. LaPierre, GaAs core− shell nanowires for photovoltaic applications. Nano Letters, 9(1): p. 148-154, 2008.

[129] X. Duan, et al., Indium phosphide nanowires as building blocks for nanoscale electronic and optoelectronic devices. Phys. Rev. A, 56, p. R1083-R1086, 1997.

[130] (a) A. Abboud et al., Applications of an energy-dispersive pnCCD for X-ray reflectivity: investigation of interdiffusion in Fe-Pt multilayers, Phys. Status

Solidi A 208, 2601, 2011. ; (b)S. Send et al., Energy-dispersive Laue diffraction by means of a frame-store pnCCD, J. Appl. Cryst.42, 1139, 2009.

[131] (a) R. Andritschke, G. Hartner, R. Hartmann, N. Meidinger, L. Striider (Data Analysis for Characterizing pn-CCDs), Nuclear Science Symposium Conference Record, NSS 08. IEEE, 2166-2172, 2008.; (b) L. Struder, J. Englhauser, R. Hartmann, P. Holl, N. Meidinger, H. Soltau, U. Briel, K. Dennerl, M. Freyberg, F. Haberl, G. Hartner, E. Pfeffermann, T. Stadlbauer, E. Kendziorra (pn-CCDs on XMM-Newton-42 months in orbit) Nuclear Instruments and Methods in Physics Research, A 512, 2003.

[132] A. Abboud, Send, Pashniak, Leitenberger, Ihle, Huth,Hartmann, Strüder and Pietsch. Sub-pixel resolution of a pnCCD for X-ray white beam applications, ,JINST, 8 P05005 doi: 10, 1088/178-0221/8/05/P05005, 2013.

[133] H. Paetzelt, V. Gottschalch, J. Bauer, G. Benndorf, and G. Wagner: J. Cryst. Growth, 2008, vol. 310, pp. 5093–97, 2008.

[134] (a) A. Davydok, A. Biermanns, U. Pietsch, .., X-Ray Diffraction from Periodically Patterned GaAs Nanorods Grown onto GaAs [111]B Metallurgical and Materials Transactions A 41, 1191, 2010.

[135] J. Wiesmann, J. Graf, C. Hoffmann,A. Hembd, C. Michaelsen, N. Yang, H. Cordes, 26 112–116. doi: 10.1002/ppsc.200800052,2009.

[136] J. Brauer, U. Pietsch, A. Davydok, A. Biermanns, J. Grenzer, V. Gottschalch, G. Wagner, “X-ray investigation of the interface structure of free standing InAs nanowires grown on GaAs [111]B”, Appl. Phys. A, 96, 851, 2009.

[137] Anton Davydok, M. Sc. thesis, X-ray Diffraction Analysis of InAs Nanowires, 2013.

[138] A. Davydok, T. Rieger, A. Biermanns,a M. Saqib,a T.. Grap, M. Ion Lepsa, and U. Pietscha (Alloy formation during molecular beam epitaxy growth of Si-doped InAs nanowires on GaAs[111]B) J Appl Crystallogr. 46(Pt 4): 893–897, 2013.

[139] Berliner Elektronenspeicherring-Gesellschaft für Synchrotronstrahlung m.b.H., BESSY II, Berlin, Germany,www.bessy.de ,2002.

[140] B. L. Henke, E. M. Gullikson, J. C. Davis, *(*X-ray interactions: photoabsorption, scattering, transmission, and reflection at E=50-30000 eV, Z=1-92)*,* Atomic Data and Nuclear Data Tables Vol. 54, 181-342 (July 1993), (http://henke.lbl.gov/optical_constants/).

[141] O. L. Krivanek, M. F. Chisholm, V. Nicolosi, T. J. Pennycook, G. J. Corbin, N. Dellby, M. F. Murfitt, C. S. Own, Z. S. Szilagyi, M. P. Oxley, S. T. Pantelides, S.J. Pennycook, Nature, 464, 571-574, 2010.

[142] D. T. Nguyen, S. D. Findlay, J. Etheridge, Ultramicroscopy,146, 6-16, 2014.

[143]K. Ikejiri, J. Noborisaka, S. Hara, J. Motohisa, T. Fukui. Journal of Crystal Growth 298, 616-619, 2007.

[144] E. Dimakis, U. Jahn, M. Ramsteiner,A. Tahraoui, J. Grandal, X. Kong, O. Marquardt, A. Trampert, H. Riechert, and L. Geelhaar, Nano Lett. 14, 2604−2609, 2015.

[145] X. Dai, A. Messanvi, H. Zhang, C. Durand, J. Eymery, C. Bougerol, F. H. Julien & M. Tchernycheva, Nano Lett. 15, 6958 -6964, 2015.

[146] M. Heiss, Y. Fontana, A. Gustafsson, G. Wüst, C. Magen, D. D. O'Regan, J. W. Luo, B. Ketterer, S. Conesa-Boj, A. V. Kuhlmann, J. Houel, E. Russo-Averchi, J. R. Morante, M. Cantoni, N. Marzari, J. Arbiol, A. Zunger, R. J. Warburton, and A. F. Morral, Nature Mater. 12, 439, 2013.

[147] R.B. Lewis, P. Corfdir, J. Herranz, H. Küpers, U. Jahn, O. Brandt and L. Geelhaar, "Self-assembly of InAs nanostructures on the sidewalls of GaAs nanowires directed by a Bi surfactant," Nano Letters 17, 4255−4260,2017.

[148] K. Tomioka, J. Motohisa, S. Hara and T. Fukui, "Control of InAs nanowire growth directions on Si," Nano Lett., vol. 8, p. 3475–3480, 2008.

[149] H. Paetzelt, V. Gottschalch, J. Bauer, G. Benndorf&G. Wagner, Journal Of Crystal Growth 310, 5093-5097-2008

[150] k. A. Dick, K., A., Bolinsson, J., Borg, B., M., & Johansson, J., Nano Letters 12, 3200-3206, 2012.

[151] A. Davtyan, S. Lehmann, D. Kriegner, R. R. Zamani, K. Dick, D. Bahrami, A. Al-Hassan, S. J. Leake, U. Pietsch, V. Holy: Characterisation of individual stacking faults in a wurtzite GaAs nanowire by Nanobeam x-ray diffraction, J. Appl. Cryst. 50, 673–680, 2017.

[152] A. Al Hassan, A.Davtyan, H. Küpers, R. B. Lewis, D. Bahrami, F. Bertram, G. Bussone, C. Richter, L. Geelhaar & U. Pietsch J. Appl. Cryst. 51, 1387-1395, 2018. ; A. Al Hassan, A., R. B Lewis., H. Ku¨ pers, W.-H. Lin, D. Bahrami, T. Krause, D. Salomon, A. Tahraoui, M. Hanke, L. Geelhaar& U. Pietsch Phys. Rev. Mater. 2, 014604, 2018.

[153] S. Send, A. Abboud, N. Wiesner, M. Shokr, M. Klaus, C. Genzel, T. Conka-Nurdan, D. Schlosser, M. Huth, R. Hartmann, L. Strüder, U. Pietsch. Application, 49, 222-233, Part 1; DOI: 10.1107/S1600576715023997, 2016.

[154] A.Tosson, M. Shokr, A. Abboud, Y. Bebawy, **A. Algashi**, R. Hartmann, M. Klaus, C. Genzel , L. Strüderb, &U. Pietsch, JINST 14 P01008, 2019.

[155]S. Send,A. Abboud, R. Hartmann, M. Huth, W. Leitenberger, N. Pashniak, J . Schmidt, L. Strüder, U. Pietsch, Vol. 711, Pages 132–142; DOI: 10.1016/j.nima. 01.044, 2013.

[156] Abboud, A., Send, S., Hartmann, R., Strüder, L., Savan, A., Ludwig, A., Zotov, N. & Pietsch, U. Phys. Status Solidi A, 208, 2601-2607, 2011.

[157]A. Abboud, S. Send, N. Pashniak, W. Leitenberger, S. Ihle, M. Huth, R. Har tmann, L. Strüder, U. Pietsch, J. Instrum. 8, P05005, 2013.

[158] M. Shokr, D. Schlosser, A. Abboud, **A. Algashi**, A. Tosson, T. Conka, L. Strüder, U. Pietsch, .Journal of Instrumentation 12 (12), P12032, 2017.

[159] Philipp E. Schroth, M. Sc. Thesis, Growth of self-catalyzed GaAs nanowires using molecular beam epitaxy and structural characterization by in-situ X-ray diffraction, 2016.

10. Acknowledgements

Foremost, I would like to express my sincere thanks and gratitude to Prof. Ullrich Pietsch, for his continued supervision, advice, constant encouragement and support throughout my studying. His motivations and constructive criticism have always led me to do more and think deeply about my experiences. I appreciate all his contributions of ideas, time and patience.

Besides my advisor, I am very thankful to Prof. Dr. Lothar Strüder for the assessment of this thesis and his support.

In my daily work with the members of the pnCCD detector group and nanoscience and semiconductor group, I have been blessed with the friendly groups who have been working side by side with me. I am grateful to all of them and particularly to my colleagues (Dr. Andreas Biermanns, Dr. Anton Davydok, Dr. Ali Al-hassan, Dr. Sebastian Send, Dr. Ali Abboud, Dr. Mohammad Shokr, Amir Tosson) for support and all the helpful discussions.

I am grateful for the support I got from the beamlines staff of EDR represented in particular by Dr. Wolfram Leitenberger and EDDI represented by Prof. Dr. Christoph Genzel and Dr.Manuela Klaus at the BESSY II - Helmholtz-Zentrum Berlin.
Words fail me to express my appreciation to my father, mother and brothers who have always been by my side whenever I need them, and their love, encouragement and constant support all the time for working until I finish my studies successfully.

In particular, I would like to extend my special thanks to my wife, Mais Alali, for her dedication, love and continued trust in me, for lifting the burden off my shoulders. I owe her for pushing me forward toward accomplishing this work.

My research would not have been possible without the financial support from the Atomic Energy Commission of Syria. Many thanks go in particular to Prof. Dr.

Ibrahim Othman and Prof. Dr. Mohamed Said Masri for their support and encouragement.

Erkärung

Hiermit erkläre ich, dass ich die vorliegende Arbeit selbstständig und nur unter Verwendung der angegebenen Literatur und Hilfsmittel angefertigt habe.

……………………………..
………………………………

(Ort) (Datum) (Unterschrift)